Multifunctional Surfaces:

Hierarchical nanoarchitectures as a toolbox for complex reactions

Inauguraldissertation

zur

Erlangung der Würde eines Doktors der Philosophie

vorgelegt der

Philosophisch-Naturwissenschaftlichen Fakultät

der Universität Basel

von

Alexandra Wiesler

aus Bad Bellingen, Deutschland

Basel, 2018

Genehmigt von der Philosophisch-Naturwissenschaftlichen Fakultät

auf Antrag von

Prof. Dr. Catherine E. Housecroft und Prof. Dr. Christof Sparr

Basel, den 11.12.2018

Prof. Dr. Martin Spiess

Dekan

Parts of this Work have been published

C. E. Housecroft, C. G. Palivan, K. Gademann, W. Meier, M. Calame, V. Mikhalevich, X. Zhang, E. Piel, M. Szponarski, A. Wiesler, A. Lanzilotto, E. C. Constable, A. Fanget, R. Stoop "'Active surfaces' as Possible Functional Systems in Detection and Chemical (Bio) Reactivity", *Chimia,* 2016, **6**, 402.

A. Wiesler, M. Garni, A. Lanzilotto, T. Einfalt, A. I. Dinu, E. C. Constable, W. P. Meier, C. G. Palivan, C. E. Housecroft, "Hierarchical assembly of compartmentalized surfaces – from empty vesicles to sticky balls", under revision.

And you ask "What if I fall?"

Oh but my darling, What if you fly?

— Erin Hanson

Table of Contents

Table of Contents

Abstract

For many decades scientists have been fascinated by the beauty and the complexity of nature and had the aim to create man-made synthetic materials with all kinds of imaginable specific functionalities. In the field of biomimetics, smart surfaces play an important role. Towards their realization, functional polymer nanostructures were immobilized on a conductive metal oxide surface through utilization of two different self-assembly phenomena: metal-ligand interactions and the formation of polymersomes from block copolymers. Glass supported titania surfaces were optimized in terms of surface roughness, by spin-coating multiple layers of titania, and further modified by stepwise assembly of an $[Fe(tpy)_2]^{2+}$-based complex as a linker unit to connect the polymersomes to the semiconductor surface. Nanoreactors based on aldehyde-terminated poly(2-methyloxazoline)-*block*-poly(dimethylsiloxane)-*block*-poly(2-methyloxazoline) (PMOXA-PDMS-PMOXA) amphiphilic block copolymer were prepared and functionalized through Schiff base condensation with an amino-functionalized tpy acting as an additional metal-binding domain. These functionalized compartments were successfully immobilized on the tpy-functionalized titania surface through assembly of the $[Fe(tpy)_2]^{2+}$ motif.

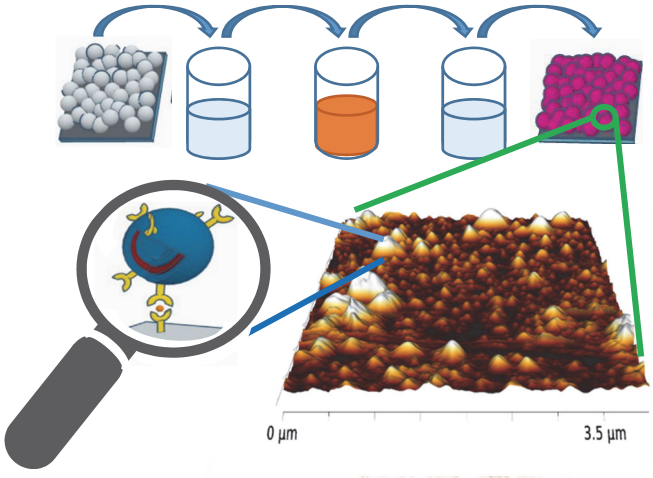

Chapter 1 gives a short overview over the strategy to create “smart surfaces” based on the immobilization of nanocompartments on a solid surface and introduces substrate types, appropriate linker systems and the formation of suitable nanocompartments with the corresponding immobilization techniques.

Chapter 2 describes the characterization of glass-supported titania surfaces and their smoothing by application of multiple layers of spin-coated titania.

Chapter 3 discusses surface modification by adsorption of metal-binding domains and the optimization process for stepwise assembly of an $[Fe(tpy)_2]^{2+}$-core as binding motif for polymersomes.

Chapter 4 describes polymersome formation and their subsequent functionalization with amino-functionalized tpy units acting as a metal-binding domains.

Chapter 5 shows the surface immobilization of the functionalized polymersomes.

Chapter 6 gives an overview of the methods and materials used in this thesis.

Chapter 7 concludes the thesis and gives a short outlook for the future.

Abbreviations

%	per cent
$[Fe(tpy)_2]^{2+}$	bis(2,2':6',2''-terpyridine)iron(II)complex
$(CD_3)_2SO$	deuterated dimethyl sulfoxide
$[PF_6]^-$	hexafluorophosphate
°C	degree celsius
^{1}H-NMR	proton nuclear magnetic resonance
AFM	atomic force microscopy
FT-IR	Fourier transform infrared spectroscopy
ANOVA	two-way analysis of variance
a.u.	arbitrary unit
C	constant
$CDCl_3$	deuterated chloroform
CHO	aldehyde
CLSM	confocal laser scanning microscopy
cm	centimetre
CO_2H	carboxylic acid
CPM	counts per molecule
D	deuterium
Decyl	*n*-decylphosphonic acid
DLS	dynamic light scattering
DMP	Dess-Martin periodinane
DMSO	dimethyl sulfoxide
DPSS	diode-pumped solid-state laser
DSSC	dye sensitized solar cell
H_4EDTA	ethylenediaminetetraacetic acid
EE	encapsulation efficiency
eq.	equivalent
Et	ethyl
Et_2O	diethyl ether
EtOH	ethanol
FCS	fluorescence correlation spectroscopy
$FeCl_2$	iron(II) chloride

FTO	fluorine doped tin oxide
g	gram
h	hour
HBr	hydrogen bromide
H_2SO_4	sulfuric acid
HCl	hydrochloric acid
HEPES	2-(4-(2-hydroxyethyl)piperazidin-1-yl)ethane-sulfonic acid
Hz	hertz
IR	infrared
J	coupling constant
K	Kelvin
K_2CO_3	potassium carbonate
kDa	kiloDalton
KNO_3	potassium nitrate
KOH	potassium hydroxide
M	mol L^{-1} or parent ion
mmol	millimole
Mn	number average molecular weight
Me	methyl
MeCN	acetonitrile
MeO	methoxy also abbreviated as OMe
MeOH	methanol
mg	milligram
min	minute
MLCT	metal to ligand charge transfer
mm	millimeter
mM	milli molar
mmol	millimole
mol	mole
mV	millivolt
Mw	weight average molecular weight
MWCO	molecular weight cut-off

N	number of particles
n	harmonic number
NaCl	sodium chloride
NaOH	sodium hydroxide
NH_2	amine
NH_3	ammonia
nm	nanometre
NMR	nuclear magnetic resonance, with the signals being identified as singlet (s), doublet (d), triplet (t), quartet (q), multiplet (m)
OH	hydroxyl group
P	power
PBS	phosphate buffered saline
PCE	photon to power conversion efficiency
PDMS	poly(dimethylsiloxane), α,ω-bis(3-hydroxypropyl)poly(dimethylsiloxane)
PDI	polydispersity index
PF_6	hexafluoridophosphate
pH	potential of hydrogen
Ph	phenyl
Phen	Phenylphosphonic acid
PMOXA	poly(2-methyloxazoline)
$PO(OH)_2$	phosphonic acid group
ppm	parts per million
Pt	platinum
QCM	quartz crystal microbalances
R	structural parameter
Rg	radius of gyration
R_H	hydrodynamic radius
R_{RMS}	Root mean squared roughness
rpm	revolutions per minute
RT	room temperature
s	Singlet

SALSAC	surface-as-ligand, surface-as-complex
sat.	saturated
SDS	sodium dodecyl sulfate
Si	silicon
SLS	static light scattering
SRB	Sulforhodamine B
StDev	standard deviation
T	transmission
T	fraction of fluorophores in triplet state
t	triplet
^{t}Bu	*tert*-butyl, used to abbreviate *tert*-butylphosphonic acid
TEM	transmission electron microscopy
TES	*N*-tris(hydroxymethyl)methyl-2-aminoethanesulfonic acid
THF	tetrahydrofuran
$TiCl_4$	titanium tetrachloride
TiO_2	titanium dioxide
TMS	tetramethylsilane
TMSBr	bromotrimethylsilane
tpy	2,2':6',2''-terpyridine
UV-O_3	ultraviolet-ozone
UV-vis	ultraviolet-visible spectrophotometry
UVO	ultraviolet ozone
V	Potential, volt
δ	chemical shift [ppm]
ε	molar absorption coefficient
ε_{max}	maximum molar absorption coefficient
η	overall conversion efficiency from solar to electrical energy for a photovoltaic device
λ	wavelength
λ_{max}	maximum absorption
µm	micrometre
τ_D	diffusion time

τ_{trip}	triplet time
Ω	electrical resistance; ohm

Structures of ligands used in this thesis

Terpyridines

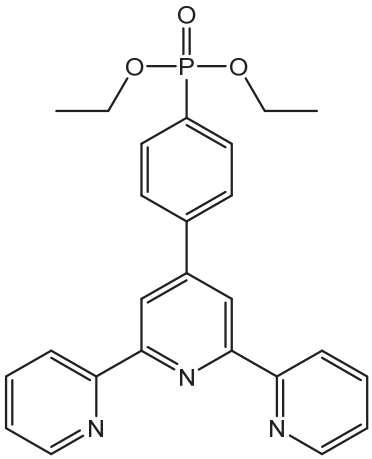

4-(2,2':6',2''-terpyridin-4'-yl)-phenylphosphonate
1

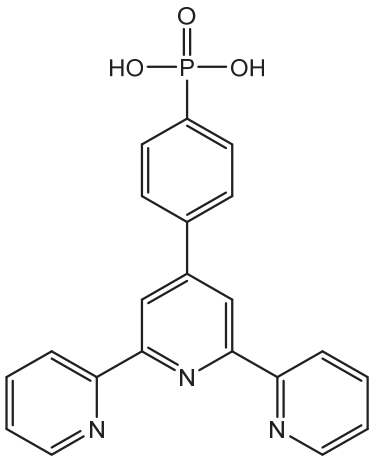

(4-([2,2':6',2''-terpyridin]-4'-yl)-phenyl)phosphonic acid
2

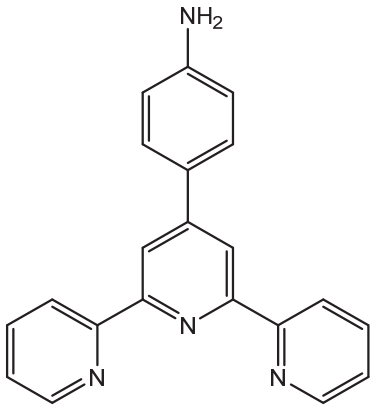

4-(2,2':6',2''-terpyridin-4'-yl)-aniline
3

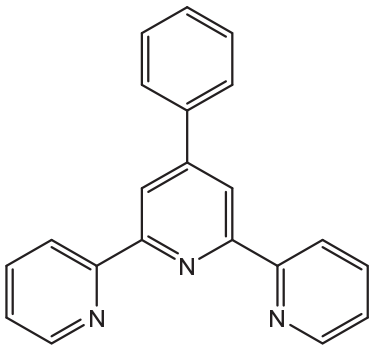

4'-phenyl-2,2':6',2''-terpyridine
4

Coadsorbants

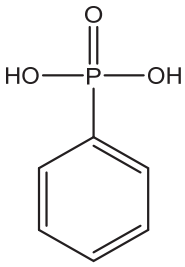

Phenylphosphonic acid

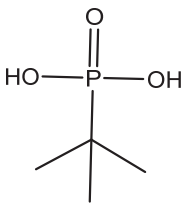

tert-Butylphosphonic acid

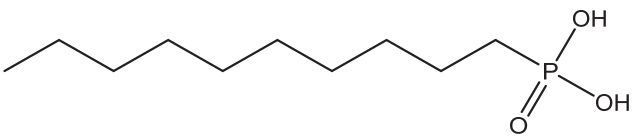

Decylphosphonic acid

Polymer

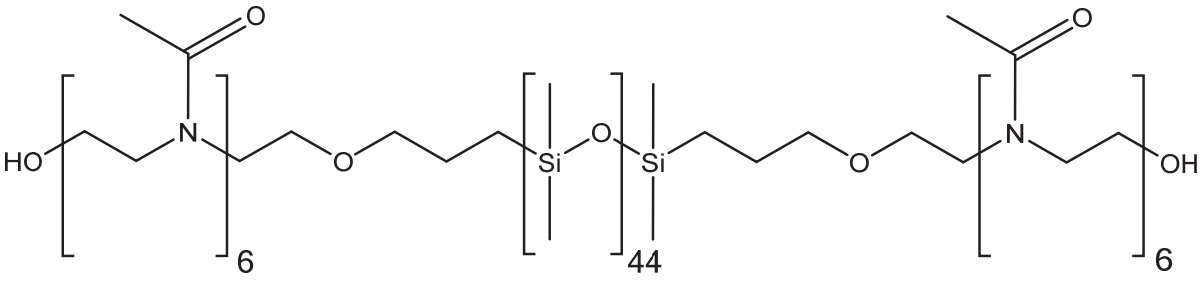

HO - poly(2-methyloxazoline - poly(dimethylsiloxane - poly(2-methyloxazoline) - OH

HO - $PMOXA_6$ - $PDMS_{44}$ - $PMOXA_6$ - OH

$A_6B_{44}A_6$

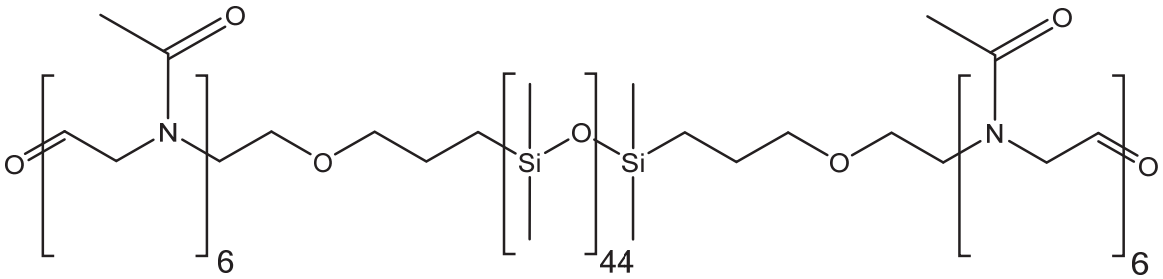

OHC - poly(2-methyloxazoline - poly(dimethylsiloxane - poly(2-methyloxazoline) - CHO

OHC - $PMOXA_6$ - $PDMS_{44}$ - $PMOXA_6$ - CHO

$A_6B_{44}A_6$-CHO

Chapter 1

Introduction

Abstract

The first chapter of this thesis serves to familiarize the reader with the fundamental principles and the scientific interest of creating “smart surfaces” based on the immobilization of nanocompartments on solid supports. Based on the biocompatibility of the nanocompartments, this system can be seen as a toolbox to study biological processes taking place inside the cavities of these nanocompartments or to create surface-attached polymer nanoreactors which can produce and release molecules/compounds locally on demand. The reader is introduced to the current state of the art of novel bioinspired materials. Further substrate types for surfaces serving for the immobilization of the nanocompartments are discussed, which are the fundamental structures used in the later chapters of this work, and appropriate linker systems are presented. The formation of nanocompartments and nanoreactors based on block copolymers is explained and other immobilization strategies introduced. Finally, the approach of creating surfaces with immobilized nanocompartments is presented.

Bioinspired materials

Nature is strange. It is harsh and unforgiving. Nature is also beautiful and ingenious. It has produced organisms that are not only perfectly adapted to their environment, but also provided with very special skills. Sea cucumbers, for example, seem inconspicuous, but have the fascinating ability to reversibly alter their body tissue to become stiff when threatened. Lotus leafs and butterfly wings have an amazing self-cleaning effect. Chitons, marine molluscs, have super strong, self-sharpening teeth, that are able to break down rocks. All of them have one thing in common: They have not only baffled but moreover inspired scientists to create smarter, functional materials. [1-5] The principles of imitating natural processes forms the field of biomimetics. It studies nature to understand its principles and underlying mechanisms, to obtain ideas and to apply its concepts for the benefit of science, engineering and medicine. [5, 6] Working at the interface between chemistry and biology serves two purposes: Biology can help to study and understand complex processes taking place in living organisms. In turn, chemistry can lead to new devices, where it mimics concepts from nature by producing synthetic analogues. [7] Examples include smart surfaces coated with anti-fouling, protective, hydrophobic or adhesive layers, that can be used in food packaging or for medical implants. [8-12] One step further towards smart surfaces for biological applications is to equip surfaces in general with biological components such as enzymes and membrane proteins. These materials serve on the one hand to get a deeper inside into biologically relevant processes taking place in nature, or on the other hand, can be used to design novel bioinspired materials. The creation of these hybrid materials, where biomolecules are combined with synthetic components such as polymer membranes gained a lot of attention in recent years due to the higher mechanical stability of polymer membranes compared with cell membranes based on lipids. Further, numerous amphiphilic block copolymers with different chemical compositions, block ratios and functionality are available to create planar membranes or via a self-assembly process, micelles, worms and polymersomes in which their properties can be easily tuned. Polymersomes especially find a lot attention due to their usage as nanoreactors when enzymes are encapsulated. The membrane can be equipped with biopores to allow substrates and products to pass the membrane serving as artificial organelles if they preserve their functionality *in vitro* and *in vivo*. Further, by using specific functionalized polymers, polymersomes can be used as carriers which release their encapsulated cargos due to their

rupture or by inducing a change of the membrane structure based on the response to different stimuli such as pH [13], temperature [14] or light. [15] The immobilization of these polymersomes on a planar solid surface can serve as a toolbox to produce enzymatic reaction products in the case of the nanoreactors, or to release specific cargos in the case of stimuli-responsive polymersomes at a defined place and on demand. This is needed in order to study biological processes or for the design of sensors.

The Surface

The most commonly used substrate for surface immobilization of polymer nanostructures is glass. [16-19] However, its poor mechanical properties, such as its inelasticity, its low fracture toughness and its brittleness, make it unsuitable for load-bearing applications, which is a disadvantage for material sciences. Titania, on the other hand, comes in various forms. It can form opaque or transparent films and is used as the white pigment in paint, sunscreen or toothpaste. [20] Titania appears in three crystal forms of TiO_2, anatase, rutile and brookite. The photocatalytical activity of the material is strongly dependent on the phase. Rutile is the thermodynamically favoured form. However, anatase has a larger bandgap and a higher conduction band energy, making it an ideal semiconductor for use in dye sensitized solar cells. [20, 21] It can also be applied as a thin film on various substrates, such as glass or even flexible plastic films. [23] Titania has a high chemical, electrochemical and thermal stability and is non-toxic, market-abundant, inexpensive and readily available. [23-26] It is considered a low-cost and clean photocatalyst, that has been used for a broad range of environmental applications, including water treatment [27] and air purification. [28-30] Furthermore it is a common additive in medical implants, such as dental prostheses (Figure 1.1). Titania shows a strong oxidizing power under UV-light illumination when in aqueous or oxygen-rich environment, that can oxidize (decompose) most organic and inorganic compounds. [30] Nanosized titania particles were even shown to have bactericidal effect under irradiation of UV light. [32] This makes Titania an attractive component in the destruction of microorganisms. In nanoparticle formation titania has a wide range of applications (Figure 1.1). [33] Among other uses, it is commonly used as a semiconductor in dye sensitized solar cells, the nanoparticulate form increasing the surface area roughly 1000 times compared to a monolayer, therefore allowing a much higher number of molecules to be adsorbed. [20, 34,35]

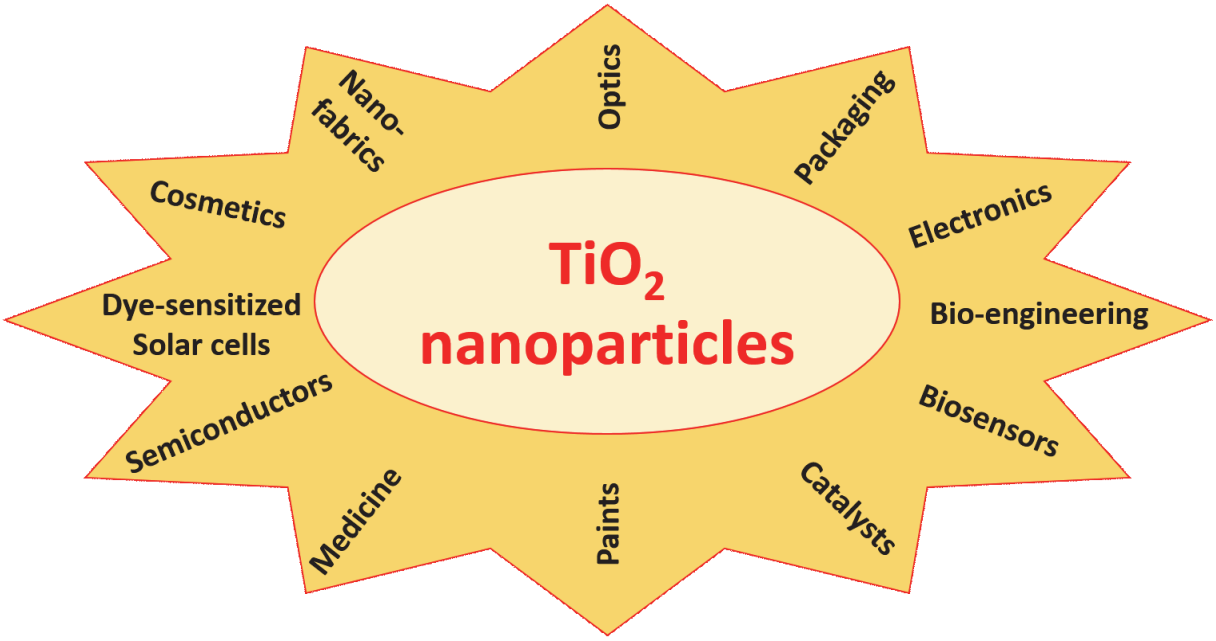

Figure 1.1. *Schematic overview of titania nanoparticle applications.*

It serves our purpose as a surface, since it can be functionalized by certain molecules with anchoring groups, meaning they can adsorb onto the titania surface. [33] The titania surface area is tunable by using nanoparticles (high roughness, large surface area) or by spin coating layers [36] of titania over a rough underlying layer for a step by step smoothing of the surface (Figure 1.2). Depending on the application, a smoother or rougher surface is required. The number of molecules adsorbed on the surface is proportional to the surface area and can therefore be tuned as well. [37]

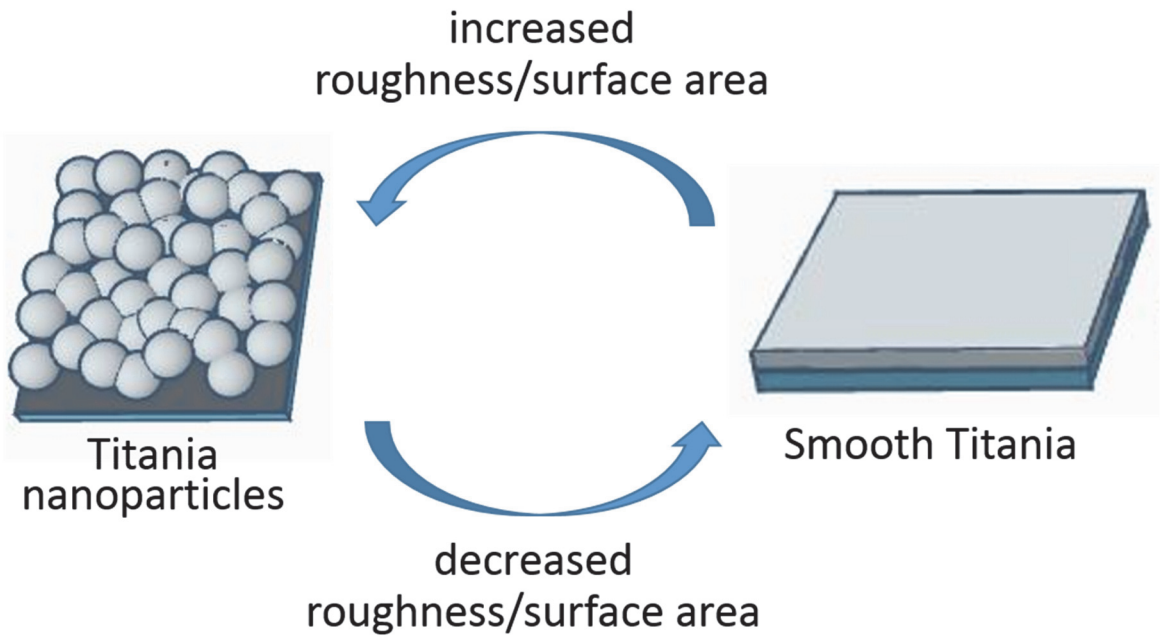

Figure 1.2. *Schematic representation of the trade off between surface smoothness and surface area.*

The Linker

In order to bind nanostructures such as nanoparticles or nanovesicles to a surface, an appropriate linker system is required. It commonly consists of receptor-ligand pairs, with one of the two being bound to the surface and the other on the nanostructure which should be linked to the surface, such as biotin-avidin or mannose-cancanavalin A. [16-18, 38] Other linking methods include sulfur-gold chemisorption [39], hydrophobic interactions, or click chemistry. Surface-binding reactions need to be fast, easy to purify, simple, versatile and give high yields, such as thiol-ene binding. [40-44] Another possible binding motif, that has not yet been used to immobilize macromolecular structures on surfaces, is the metal-ligand motif of metal coordination complexes. *N*-Heterocycles exist in various forms and present effective and stable complexation agents for many transition metals, such as copper(I), nickel(II), ruthenium(II). This can be used to generate a broad variety of supramolecular and highly sophisticated structures, such as helicates, racks, and grids. [45] It has even led to the development of not only metal-containing, but also metal-based coordination polymers, for several applications ranging from filtration to catalysis. [46] We focus on 2,2':6',2''-terpyridine, simplified to terpyridine and abbreviated with tpy, ligands and their self-assembly with iron(II) to the $[Fe(tpy)_2]^{2+}$-complex as a binding motif. Terpyridine was first synthesized in 1931. Because of the spatial disposition of its three nitrogen atoms, it can act as a tridentate ligand (Scheme 1.1). [46, 47] The 2,2':6',2''-tpy isomer forms a bis(chelate) unlike other isomers (eg. 4,2':6',4''-tpy) of tpy.

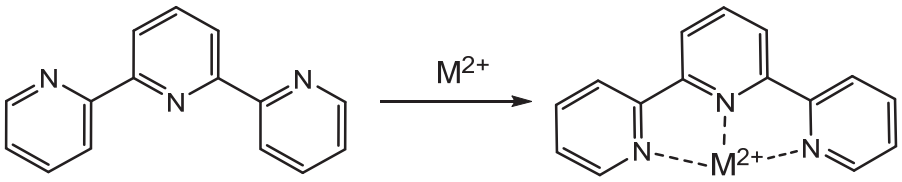

Scheme 1.1. Change in ligand configuration upon binding a metal ion.

The stability of such complexes is highly important for their applicability. The use of terpyridines as chelating ligands is very promising, because they are well-known to build highly stable complexes with interesting physical characteristics with transition-metal ions. [45] A coordination bond is formed between the metal or metal ion and the lone electron pair of an organic ligand, in which case the metal acts as a Lewis acid and the ligand as a Lewis base. [48] Complexation with iron(II) to use the $[Fe(tpy)_2]^{2+}$-complex as a linker, is attractive because of

the iron(II) complex`s relative stability compared with other transition metals, [49] while the complexation can be undone by addition of EDTA. [50]

The Polymer Nanocompartments

Amphiphillic block copolymers are inspired by amphiphilic phospholipids, which are the main building blocks of natural biological membranes. [51] Cell membranes based on lipids have typical membrane thicknesses of 3-5 nm whereas the membranes of polymersomes based on amphiphilic polymers have thicknesses in the range of 5 to 30 nm. [51] The large variety of the chemical compositions of the polymersomes leads to a broad range of thermodynamic and chemical properties compared to liposomes. Polymersomes have a higher mechanic stability and offer greater adaptability for further improvement of their properties. [52-54] Amphiphilic block copolymers can form various structures in aqueous solution via a self-assembly process such spherical, cylindrical, gyroidal and lamellar structures [55-57], depending on: *i*) the hydrophilic to total mass ratio (*f*-value), *ii*) the packing parameter *p,* and *iii*) the dispersity of the copolymer chains. [58, 59] The self-assembly process based on the chemical structures of the polymers is essential to the types of structures that are formed. Based on the formation method, other nanostructures can be formed such as micelles and/or worms. For the formation of polymersomes equipped with biomolecules such as enzymes or membrane proteins, the use of volatile solvents can affect their functionality. Formation methods to create polymersomes are *i*) direct dissolution of the dry polymer powder, *ii*) thin-film rehydration, *iii*) solvent exchange method and *iv*) double emulsion techniques. [60-62] For polymersome formation through film rehydration, the method used in this thesis, a block copolymer is dissolved in an appropriate organic solvent and subsequently the solvent is evaporated, depositing the polymer as a thin film on the flask walls. This film is slowly hydrated with a solvent suitable for one of the blocks, typically water based buffers. Stirring or ultrasonication supports the hydration process and therefore the formation of polymersomes. Although generally size and shape of polymersomes depend on the preparation method, polymersome size can be decreased through extrusion. In this process, a filter with a defined nanopore size is used to pass the polymersomes through. [63]

Due to the possibility to encapsulate specific molecules inside their cavities, polymersomes can be used as carriers to release specific cargos. [64] Applications of polymersomes include catalysis [65], sensing [66], complex multistep reactions like (enzyme) cascade reactions [67, 68],

localized drug production and delivery [69, 70], biomimetic arrangements. [71] An example of a sensor is described in Figure 1.3. [72]

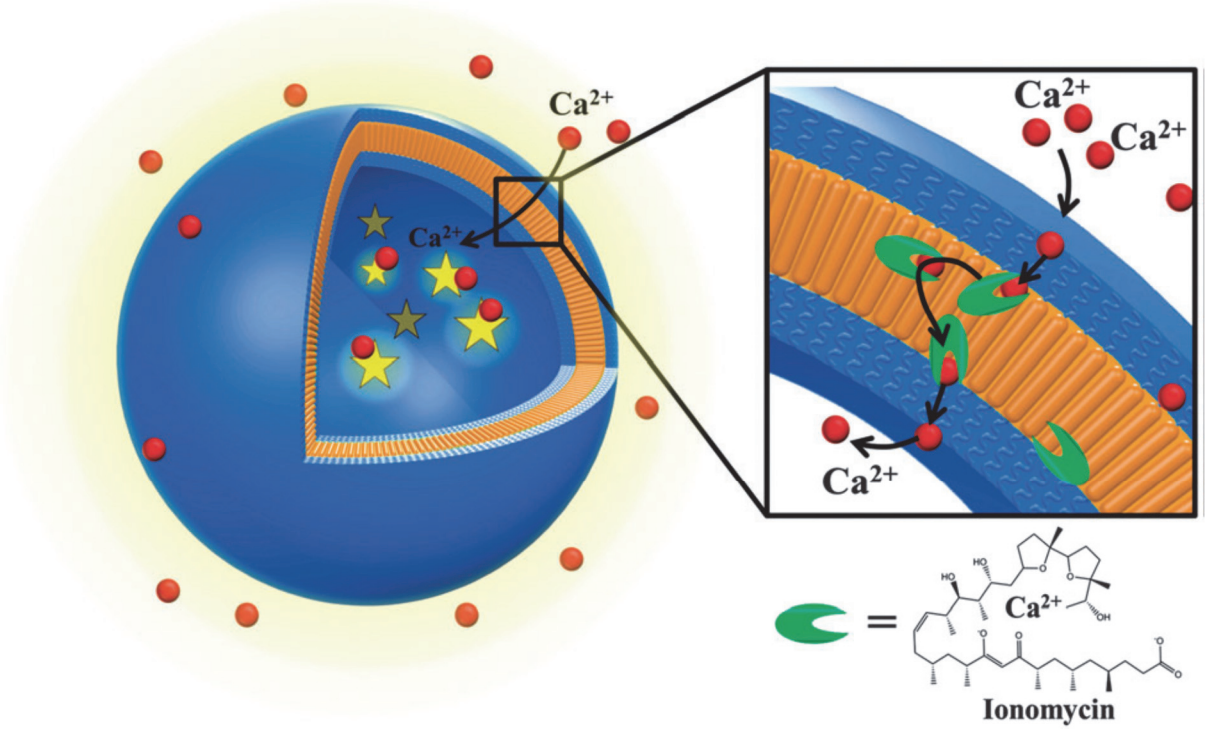

Figure 1.3 *Schematic representation of a biosensor based on polymersomes with inserted ionomycin to achieve membrane permeability for Ca^{2+}-sensitivity. Reproduced from Ref. 72 with permission from the PCCP Owner Societies.*

Further, they can be used as nanoreactors if they are equipped with membrane proteins in their membrane and enzymes inside their cavities so that the substrates and products can pass through the membrane. They can even act as artificial organelles [73] if they preserve their functionality *in vitro* and *in vivo.*

Polymersomes immobilized on surfaces

Solid supports based on materials such as glass or mica have been previously used to immobilize polymer nanostructures. Among others these included hollow-sphere polymersomes, which retained their functionality and responsiveness. When designed correctly, the set-up of immobilizing polymersomes can result in stimuli-responsive "active surfaces". Temperature responsiveness has been achieved by using surface-immobilized polymersomes based on poly (acrylic acid) (PAA) bearing pluronic L121, PEO-*b*-PPO-*b*-PEO, which could be detached from the surface with increasing temperature. [74] The design of such systems does not only serve as a possible life-science tool but also sheds light on the single

vesicle dynamics. Other examples of surface immobilized polymersomes include polymersomes based on PLA-*b*-PEO, PCL-*b*-PEO and PI-*b*-PEO polymers attached to aldehyde modified supports by chemical bonds (Figure 1.4). [75]

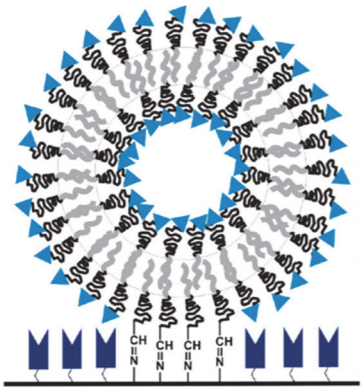

Figure 1.4. *Immobilization of nanocompartments made of aldehyde-modified block copolymers on an aminated glass surface. Adapted and modified with permission from Ref 75. Copyright (2010) American Chemical Society.*

In a similar approach, treated-porous polyacrylonitrile (PAN) membranes served as a surface for covalent attachment of PMOXA-*b*-PDMS-*b*-PMOXA vesicles containing carboxylate or amine groups by means of click chemistry [76]. Due to the straightforwardness, the system has been proposed as a valid candidate for membrane based filtration and biosensing technology. Among others, the biocompatibility of PMOXA-*b*-PDMS-*b*-PMOXA allowed integration of phosphoglycerate kinase (PK) proteins in the membrane of PMOXA-*b*-PDMS-*b*-PMOXA-based vesicles and subsequent immobilization on to streptavidin covered glass substrates. [77] As a milestone in the field, this principle of immobilization of biomolecule encapsulating polymersomes opened up a field that allowed research on protein behavior (i.e. folding), as the vesicles harboring the protein can protect it from extreme conditions by exploiting the remarkably stable nature of polymersomes.

In other examples, soft multifunctional (pH and light responsive) polymersomes were attached to solid surfaces by means of strong molecular interactions, such as the example of adamantine-β-cyclodextrin. [78] More recently, a proton sensitive fluorescent dye was encapsulated into methacrylate functionalized PMOXA-*b*-PDMS-*b*-PMOXA vesicles, followed by polymersome attachment to thiol functionalized surfaces [79] to obtain an active surface for pH reporting. Differences in pH of the external environment lead to a change in the fluorescence intensity of the polymersome coated surface, due to the protonation / deprotonation of the encapsulated sensitive dye.

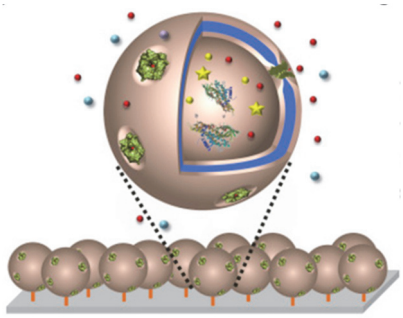

Figure 1.5. *Schematic representation of an "active surface" serving as a sugar alcohol biosensor based on the immobilization of nanoreactors, where the reconstitution of the membrane protein (GlpF) together with the encapsulation of the enzyme (RDH) allowed selective transport and detection of sugar alcohols. Adapted with permission from Ref 80. Copyright (2016) Elsevier.*

Polymersomes encapsulating an active biomolecule, referred to as nanoreactors, were also attached to solid supports in order to mimic particular biological processes. In a prominent example, ribitol dehydrogenase (RDH) enzymes were encapsulated into aldehyde functionalized PMOXA-*b*-PDMS-*b*-PMOXA vesicles and subsequently attached to an amino group-bearing surface substrate (Figure 1.5). [80] Since polymersome membranes are naturally impermeable to substrates of the RDH enzyme, selective diffusion of sugar alcohols from outside to inside of vesicles was achieved by insertion of the *E.coli* glycerol facilitator (GIpF) into the polymersome membrane. In a similar approach, the enzyme penicillin acylase was protected within the cavities of PMOXA-*b*-PDMS-*b*-PMOXA polymersomes and successfully catalysed the production of antibiotics, killing the surrounding bacteria. [81] Astonishingly, surface immobilized polymersome nanoreactors were stable over the course of several days. The stability of the hollow-sphere polymersomes allowed the enzyme to retain its activity producing a drug, which efficiently inhibited bacterial growth in its surroundings. A first proof of concept of its kind, this model could potentially be used to prevent bacteria related infections of medical devices in a controlled manner. Overall, the immobilized nanoreactors create biomimetic surfaces that find their applications as biosensors and antifouling surfaces.

Aim of the thesis

In this project, inspired by nature, we aimed to go a step farther and produce a flexible and versatile template based on immobilized polymersomes on a solid surface, that can be assembled as easily as putting together a LEGO® structure. The aim was for the surface to function as a basis for a variety of applications, such as complex reactions, sensors or biological

models. The surfaces were equipped with different functionalities and characteristics: A solid-supported, electronically conductive surface with a tunable surface area was combined with a stable, but reversibly-formed metal complex to immobilize polymersomes, which can contain and release different compounds based on the type of polymer used. To achieve this, we exploit two self-assembly phenomena, self-assembly of block copolymers into polymersomes in an aqueous solution and metal-ligand interactions. Our general strategy is shown in Figure 1.6. A hydroxyl terminated/bifunctional amphiphilic triblock copolymer, poly(2-methyloxazoline)-*block*-poly(dimethylsiloxane)-*block*-poly(2-methyloxazoline) (HO-PMOXA$_6$-PDMS$_{44}$-PMOXA$_6$-OH, referred to as A$_6$B$_{44}$A$_6$). (Figure 1.6a) can be oxidized to give aldehyde end groups, OHC-PMOXA$_6$-PDMS$_{44}$-PMOXA$_6$-CHO (referred to as A$_6$B$_{44}$A$_6$-CHO), (Figure 1.6b) and then forms via a self-assembly process spherical hollow nanostructures/nanocompartments (Figure 1.6c). After functionalizing the outer surface of the polymersomes with 2,2':6',2''-terpyridine (tpy) units, through Schiff base condensation of the polymer`s aldehyde groups with the primary amine of 4-([2,2':6',2''-terpyridin]-4'-yl)aniline, (Figure 1.6d), we can use the formation of bis(2,2':6',2''-terpyridine)iron(II) complexes upon the addition of iron(II) (Figure 1.6, purple) as a driving force to interconnect nanocompartments (Figure 1.6e) or bind the latter to a titania surface functionalized with terpyridine anchoring domains (Figure 1.6f). This system is versatile, stable, can be assembled in ambient conditions and allows for a variety of functionalizations.

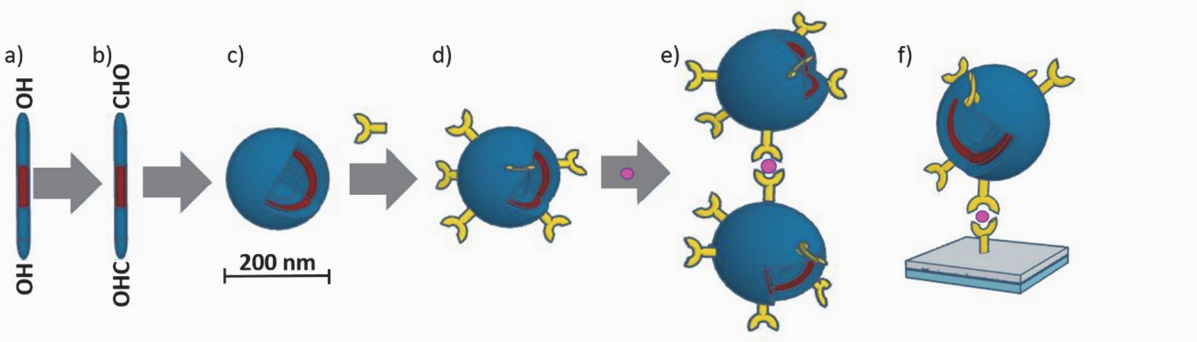

Figure 1.6. *Schematic illustration of the modification and self-assembly of amphiphilic block copolymers (in blue and red) into nanocompartments: A hydroxy terminated/ bifunctional amphiphilic triblock copolymer (a) can be oxidized to aldehyde end groups (b) and after self-assembly into nanocompartments (c). After functionalization with a metal binding ligand (yellow) (d), they can be reversibly bound together (e) or to a surface (f) by addition of metal ions (purple).*

References

[1] L. Hsu, C. Weder, S. J. Rowan, *J. Mater. Chem.*, 2011, **21**, 2812.

[2] H. J. Ensikat, P. Ditsche-Kuru, C. Neinhuis, W. Barthlott, *Beilstein J. Nanotechnol.,* 2011, **2***,* 152.

[3] T. Saison, C. Peroz, V. Chauveau, Serge Berthier, E. Sondergard, *Biomimetics, IOPSCIENCE*, 2008, **3**, 046004.

[4] C. Liu, Y. Han, C. Guo, *J. Wuhan Univ. Technol.-Mat. Sci. Edit.,* 2011, **26**, 478.

[5] J. Hwang, Y. Jeong, J. Min Park, K. H. Lee, J. W. Hong, J. Choi, *Int. J. Nanomedicine*, 2015, **10**, 5701.

[6] P.t Garg, P. Ghatmale, K. Tarwadi, S. Chavan**,** *Biomimetics,* 2017, ***2***, 7.

[7] R. Breslow, *J. Biol. Chem.*,2009, **284**, 1337.

[8] J. Bico, C. Marzolin, D. Quéré, *Europhys. Lett.,* 1999, **47**, 220.

[9] C. Sanchez, H. Arribart, M. Madeleine, G. Guille, *Nat. Mater.*, 2005, **4**, 277.

[10] J. Vincent, *Structural Biomaterials*, Princeton Univ. Press, New Jersey,USA, 1990.

[11] A. H. Simmons, C. A. Michal, L. W. Jelinski, *Science*, 1996, **271**, 84.

[12] B. Bensaude-Vincent, H. Arribart, Y. Bouligand, C. Sanchez, *New J. Chem.*, 2002, **1,** 1.

[13] Z. Y. Qiao, C. Jing, J. Ran, D. Fu-Sheng, L. De-Hai, J. Shou-Ping, L. Zi-Chen, *RSC Adv.*, 2013, **3**, 24345.

[14] C. Sanson, J.-F. Le Meins, C. Schatz, A. Soum, S. Lecommandoux, *Soft Matter*, 2010. **6**, 1722.

[15] X. Hu, Z. Yuqi, X. Zhigang, J. Xiabin, B. Adriano, G. Zhen, *Biomacromolecules*, 2017, **18**, 649.

[16] N. P. Kamat, S. J. Henry, D. Lee, D. A. Hammer, *Small,* 2013, **9**, 2272.

[17] T. Olsson*,* V. P. Zhdanov*,* F. Höök, *J. Appl. Phys.*, 2015, **118**, 064702.

[18] P. Kuhn, K. Eyer, T. Robinson, F. I. Schmidt, J. Mercerb, *Integr. Biol.,* 2012, **4**, 1550.

[19] M. J. Sarmento, M. Prieto, F. M. J. Fernandes, Biochim. Biophys. Acta, 2012, 1818, 2605.

[20] A. Hagfeldt, G. Boschloo, L. Sun, L. Kloo, H. Pettersson, *Chem. Rev.*, 2010, **110**, 6595.

[21] S. Valencia, J. M. Marin, G. Restrepo, *Open Mater. Sci. J.*, 2010, **4**, 9.

[22] H. C. Weerasinghe, F. Huang, Y.-B. Cheng, *Nano Energy*, 2013, **2**, 174.

[23] M. R. Hoffmann, S. T. Martin, W. Choi, D. W. Bahnemann, *Chem. Rev.,* 1995, **95**, 69.

[24] A. Fujishima, T. N. Rao, D. A. Tryk, *J. Photochem. Photobiol. C: Photochem. Rev.*, 2000, **1**, 1.

[25] S. Sharma, B. Siwach, S. K. Ghoshal, D. Mohan, *Renewable Sustainable Energy Rev.*, 2017, **70**, 529.

[26] M. A. M. Al-Alwani, A. B. Mohamad, N. A. Ludin, A. A. H. Kadhum, K. Sopian, *Renewable Sustainable Energy Rev.*, 2016, **65**, 183.

[27] Q. Li, S. Mahendra, D. Y. Lyon, L. Brunet, M. V. Liga, D. Li, P. J. J. Alvarez, *Water Res.*, 2008, **42**, 18, 4591.

[28] L. S. Acosta-Torres, L. M. López-Marín, E. R. Elvira Núñez-Anita, G. Hernández-Padrón, V. M. Castaño, *J. Nanomater.*, 2011, **2011**, 1.

[29] T. Nonami, H. Hase, and K. Funakoshi, *Catal. Today*, 2004, **96**, 113.

[30] L. Sikong, B. Kongreong, D. Kantachote, W. Sutthisripok, *Energy Research Journal*, 2010, **1**, 120.

[31] C. C. Trapalis, P. Keivanidis, G. Kordas, *Thin Solid Films*, 2003, **433**, 18.

[32] S. Kwak, S. H. Kim, S. S. Kim, *Environ. Sci. Technol.*, 2001, **35**, 2388.

[33] A. Mbonyiryivuze, S. Zongo, A. Diallo, S. Bertrand, E. Minani, L. Lal Yadav, B. Mwakikunga, S. M. Dhlamini, M. Maaza, *Phys. Mater. Chem.*, 2015, **3**, 12.

[34] B. Bozic-Weber, E. C. Constable, C. E. Housecroft, *Coord. Chem. Rev.*, 2013, **257**, 3089.

[35] K. Kalyanasundaram, A. Hagfeldt, G. Boschloo, L. Sun, L. Kloo, H. Pettersson, *Chem. Rev.*, 2010, **110**, 6595.

[36] *A. C.* Arango, L. R. Johnson, V. N. Bliznyuk, Z. Schlesinger, S. A. Carter, H. H. Hörhold, *Adv. Mater.*, 2000, **12**, 1689.

[37] J. Gong, J. Liang, K. Sumathy, *Renewable Sustainable Energy Rev.*, 2012, **16**, 5848.

[38] O. Roling, C. Wendel, U. Kauscher, P. Seelheim, H.-J. Galla, B. J. Ravoo, *Langmuir*, 2013, **29**, 10174.

[39] C. Gou, P. Boullanger, L. Jiang, T. Liu, *Colloids and Surfaces B: Biointerfaces*, 2008, **62**, 146.

[40] J. Zhang, L. Zhang, C. Lei, X. Huang, Y. Yang, C. Yu, *Langmuir*, 2018, **34**, 5011.

[41] Q. Yang, M. Wallstne, P. Ludahl, *Biochim. Biophys. Acta*, 1988, **938**, 243.

[42] I. Stanish, D. A. Lowy, Y. Lee, J. Fang, E. Wong, R. I. Ray, A. Singh, *J. Phys. Chem. B,* 2004, **108**, 127.

[43] C. D. Hein, X. M. Liu, D. Wang, *Pharm. Res.*, 2008, **25**, 2216.

[44] U. S. Schubert, C. Eschbaumer, *Angew. Chem. Int. Ed.*, 2002, **41**, 2892.

[45] U. S. Schubert, *in Tailored Polymers & Applications*, Eds.: Y. Yaggi, M. K. Mishtra, O. Nuyken, K.Ito, G. Wnek, VSP, Utrecht, 2000, 63.

[46] S. G. Morgan, F. H. Burstall, *J. Chem. Soc.*, 1931, 20.

[47] S. G. Morgan, F. H. Burstall, *J. Chem. Soc.,* 1937, 1649.

[48] C. E. Housecroft, A. G. Sharpe, in *Inorganic Chemistry, 3rd edn*, Pearson, Harlow United. Kingdom, 2008, p. 198.

[49] M. A. R. Meier, B. G. G. Lohmeijer, U. S. Schubert, *J. Mass Spectrom.,* 2003, **38**, 510.

[50] E. C. Constable, W. Meier, C. Nardin, S. Mundwiler, *Chem. Commun.*, 1999, 1483.

[51] F. Itel, M. Chami, A. Najer, S. Lörcher, D. Wu, I. A. Dinu, W. Meier, *Macromolecules*, 2014, **47**, 7588.

[52] B. M. Discher, Y.-Y. Won, D. S. Ege, J. C-M. Lee, F. S. Bates, D. E. Discher, D. A. Hammer, *Science*, 1999. **284**, 1143.

[53] O. Onaca, R. Enea, D. W. Hughes, W. Meier, *Macromol. Biosci.*, 2009, **9**, 129.

[54] J. S. Lee, J. Feijen, *J Controlled Release*, 2012, **161**, 473.

[55] D. E. Discher, F. Ahmed, *Annu. Rev. Biomed. Eng.*, 2006, **8**, 323.

[56] D. M. Vriezema, M. C. Aragonès, J. A. A. W. Elemans, J. J. L. M. Cornelissen, A. E. Rowan, R. J. M. Nolte, *Chem. Rev.*, 2005, **105**, 1445.

[57] P. van Rijn, M. Tutus, C. Kathrein, L. Zhu, M. Wessling, U. Schwaneberg, A. Böker, *Chem. Soc. Rev.*, 2013, **42**, 6578.

[58] Y. Mai, A. Eisenberg, *Chem. Soc. Rev.*, 2012, **41**, 5969.

[59] D. E. Discher, A. Eisenberg, *Science*, 2002, **297**, 967.

[60] P. V. Pawar, S. V. Gohil, J. P. Jain, N. Kumar, *Polym. Chem.*, 2013, **4**, 3160.

[61] K. Kita-Tokarczyk, J. Grumelard, T. Haefele, W. Meier, *Polymer*, 2005, **46**, 3540.

[62] C. Martino, T. Y. Lee, S. H. Kim, A. J. deMello, *Biomicrofluidics*, 2015. **9**, 024101.

[63] J. E. Bartenstein, J. Robertson, G. Battaglia, W. H.Briscoe, *Colloids. Surf., A*, 2016, **506**, 739.

[64] P. Tanner, P. Baumann, R. Enea, O. Onaca, C. Palivan, W. Meier, *Acc. Chem. Res.*, 2011, **44**, 1039.

[65] L. Marchetti, M. Levine, *ACS Catalysis,* 2011, **1**, 1090.

[66] J. H. Lee, H.-E. Jin, M. S. Desai, S. Ren, S. Kim, S.-W. Lee, *Nanoscale,* 2015, **7**, 18379.

[67] K. C. Nicolaou, T. Montagnon, S. A. Snyder, *Chem. Commun.,* 2003, **5**, 551.

[68] D. M. Vriezema, P. M. L. Garcia, S. N. Oltra, N. S. Hatzakis, S. M. Kuiper, R. J. M. Nolte, A. E. Rowan, J. C. M. van Hest, *Angew. Chem.,* 2007, **119**, 7522..

[69] K. Langowska, J. Kowal, C. G. Palivan, W. Meier, *J. Mater. Chem. B,* 2014, **2**(29), 4684.

[70] L. S. Lee, J. Feijen, *J. Control. Release*, 2011, **161**, 473.

[71] M. Spulber, P. Baumann, S. S. Saxer, U. Pieles, W. Meier, N. Bruns, *Biomacromolecules,* 2014, **15**, 1469.

[72] M. Lomora, F. Itel, I. A. Dinu, C. G. Palivan, *Phys. Chem. Chem. Phys.,* 2015, **17**, 15538.

[73] T. Einfalt, D. Witzigmann, C. Edlinger, S. Sieber, R. Goers, A. Najer, M. Spulber, O. Onaca-Fischer, J. Huwyler, C.G. Palivan, *Nature Commun.*, 2018, **9**, 1127.

[74] F. Li, T. Ketelaar, M. A. C. Stuart, E. J. R. Sudhölter, F. A. M. Leermakers, A. T. M. Marcelis, *Langmuir*, 2008, **24**, 76.

[75] S. Domes, V. Filiz, J. Nitsche, A. Frömsdorf, S. Förster, *Langmuir*, 2010, **26**, 6927.

[76] Rein, C., S. Nissen, M. Grzelakowski, M. Meldal, *J. Polym. Sci. A: Polymer Chem.*, 2016, **54**, 2032.

[77] T. Rosenkranz, A. Katranidis, D. Atta, I. Gregor, J. Enderlein, M. Grzelakowski, P. Rigler, W. Meier, J. Fitter, *ChemBioChem*, 2009, **10**, 702.

[78] B. Iyisan, A. Janke, P. Reichenbach, L. M. Eng, D. Appelhans, B. Voit, *ACS Appl. Mater. Interfaces*, 2016, **8**, 15788.

[79] I. Craciun, A. S. Denes, G. Gunkel-Grabole, A. Belluati, C. G. Palivan, *Helv. Chim. Acta*, 2018, **101**, e1700290.

[80] X. Zhang, M. Lomora, T. Einfalt, W. Meier, N. Klein, D. Schneider, C. G. Palivan, *Biomaterials*, 2016, **89**, 79.

[81] K. Langowska, J. Kowal, C. G. Palivan, W. Meier, *J. Mater. Chem. B*, 2014, **2**, 4684.

Chapter 2

The Surface -Optimization of TiO_2 surface roughness

Abstract

Following a straightforward approach, we focus here in this chapter on the surface made of titania on a glass surface used as a solid support which is one of the main building blocks towards the surface immobilization of polymer nanocompartments. The surface topology of commercial electrodes, "Test Cell Titania Electrodes" from Solaronix and FTO-covered glass is measured as a means to analyze the surface roughness. Further, the root mean square roughness R_{RMS} was calculated to quantify the roughness, which is also an indicator of the surface area. Starting with commercial FTO-covered glass, the surface roughness was decreased by spin-coating multiple titania layers onto the FTO. Monitoring the decrease in roughness via R_{RMS} calculations, the optimum smoothness was achieved with seven compact layers of spin coated TiO_2, reaching an average R_{RMS} of 2.0 ± 0.2 nm.

Motivation and Problem Definition

Smart, nanostructured surfaces hold remarkable potential for applications in material sciences, that range from diagnostic assays to drug delivery systems. [1, 2] Similar systems include surface bound planar polymer membranes, brushes and vesicles [3-6] However, existing systems rely on the tunability of the surface-bound component, rather than the solid support itself. [7-9] This system is aimed to be a toolbox for versatile applications. In this chapter we focus on the surface that is used as a solid support. As part of the desired versatility, the surface should not only be stable towards thermal and chemical influences. For possible biomedical applications, non-toxicity is a requirement. At the same time, all components, including the surface, should be tunable. In this work we focused on a fluorine-doped tin oxide (FTO) coated glass substrate coated with TiO_2 as a solid support due to its ability to fulfil the above mentioned requirements. Titania, an n-type semiconductor, is a solid material, electrically conductive, inexpensive, stable, non-toxic and biocompatible and is being applied in a large range of applications, like sunscreen (because of its ability to absorb UV radiation) and wall paint. [10-12] Besides the use of tiania as single crystal or thin film, it can further be used in the form of nanoparticles. The great advantage of nanoparticulate titania lies in the increased surface area, estimated to be around 1000 times the area of bulk material. [13, 14] The larger surface area allows for a larger molecular load to be bound to the surface. However, some characterization methods, such as for example, atomic force microscopy (AFM) require a smooth surface. To find the optimal compromise between the surface area and the surface roughness is a challenging task which will be addressed in this chapter. Therefore commercially available titania electrodes are compared to FTO-covered glass by imaging and determination of Root mean squared roughness (R_{RMS}) [15] using AFM. Through manual layer-by-layer deposition of titania, the surface is gradually smoothed until the desired level is reached.

Evaluation of commercially available surfaces

Before optimization of the surface roughness, the existing commercial available surfaces “Test Cell Titania Electrodes” and FTO-covered glass were investigated. The surface roughness of the solid-supported titania electrodes of both commercially available substrates had to be determined. The surface roughness was calculated by determining the R_{RMS} values of the individual surfaces using the measured AFM images. The roughness could be quantified by the

R_{RMS}. It is given by the standard deviation of the z-values for the sample area and was calculated for every image.

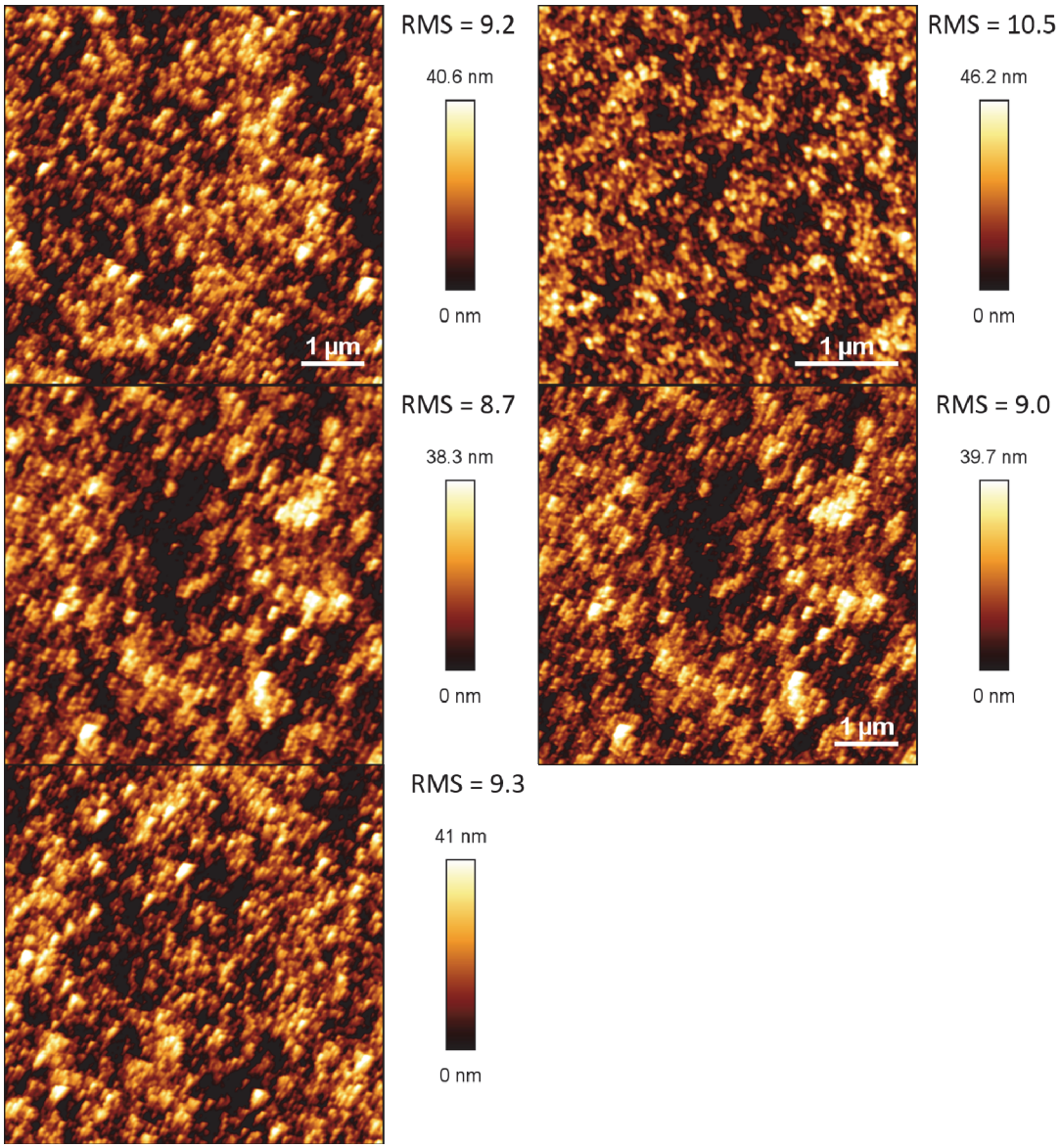

Figure 2.1. *AFM images of commercial Test Cell Titania Electrodes.* R_{RMS} *in nm.*

AFM images were taken of the commercial electrodes showing the nanoparticulate titania covering the surface (Figure 2.1). The nanoparticles have an average diameter of 50 nm as determined from cross sections of the images. R_{RMS} values lie between 8.7 and 10.5 nm, with an average R_{RMS} of 9.4 ± 0.7 nm. The FTO-covered glass seems to have a needle to rod like structure with sharp edges. In comparison to the titania nanoparticulate surface, the surface roughness of the FTO was much higher (Figure 2.2). This could be obtained by the corresponding R_{RMS} values ranging from 24.6 to 27.6 nm, with an average R_{RMS} of 26.0 ± 1.4 nm. Surprisingly, the FTO has a much rougher surface than the titania nanoparticles. For these

relatively rough solid surfaces, proving vesicle attachment by AFM would fail, because all characterization methods for surface bound polymersomes rely on a relatively smooth surface to identify the nano-assembly architectures. Therefore these surfaces need to be smoothed.

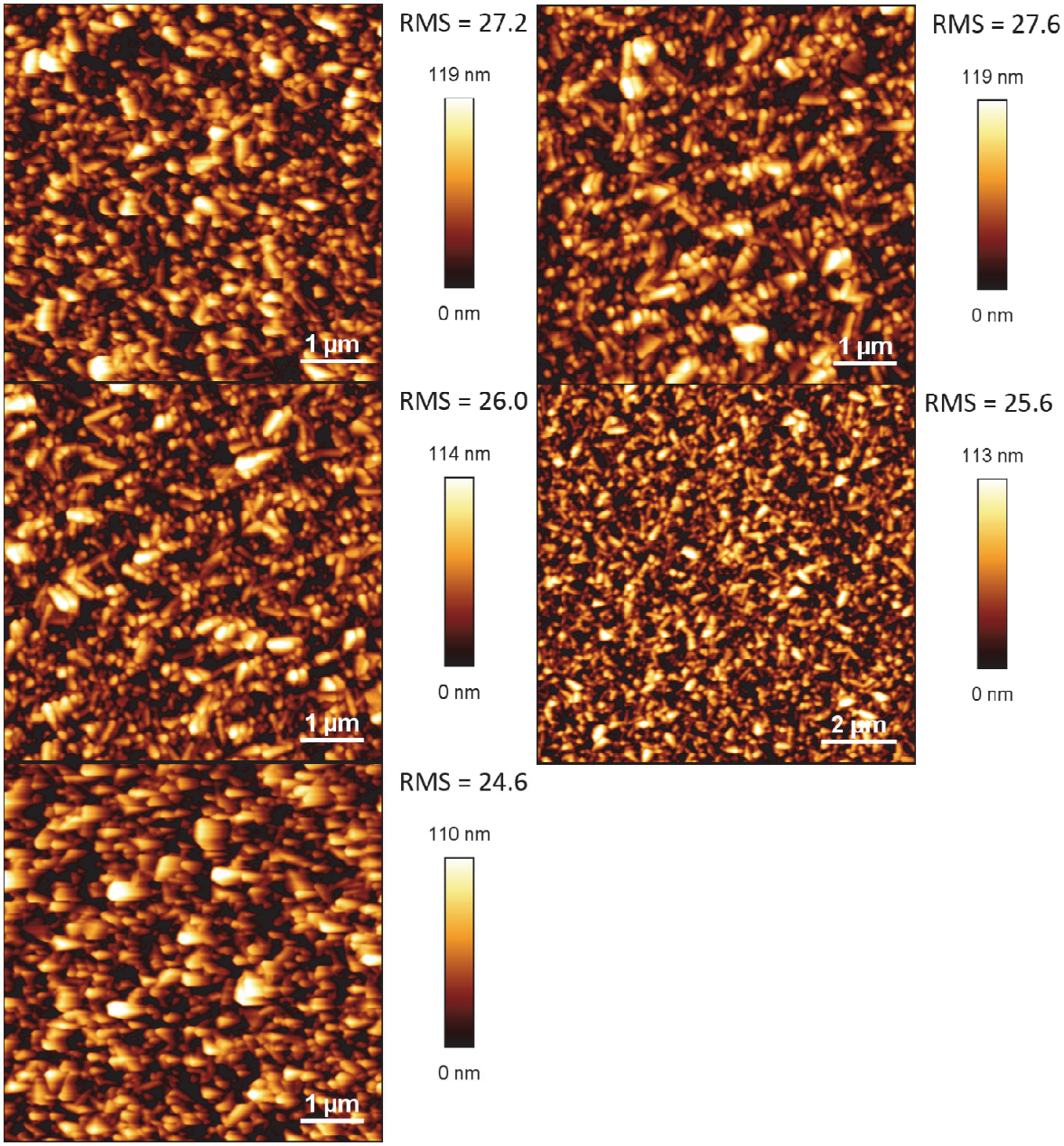

Figure 2.2. *AFM images of commercially available FTO covered glass*

Optimization of TiO_2 surface roughness

For further experiments we used FTO-covered glass surfaces. The optimization of surface smoothness could be achieved through deposition of multiple TiO_2 layers. It was necessary to optimize the surface smoothness for later analysis of the successful polymersome binding.

After having determined the surface roughness of FTO-covered glass, the surface was gradually smoothed by the application of titania layers (Figure 2.3).

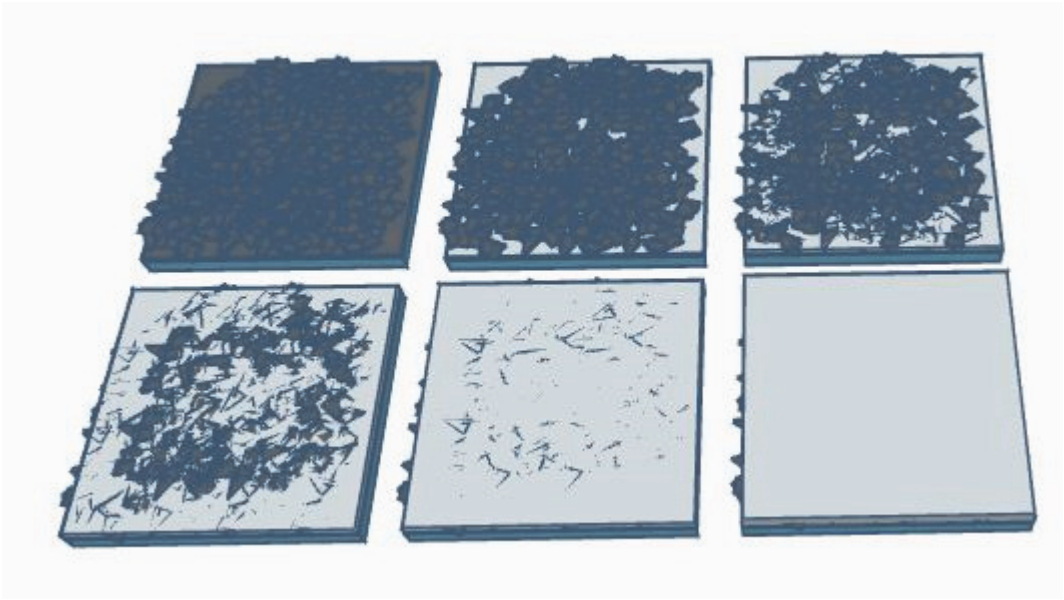

Figure 2.3. *Schematic representation of the gradual smoothing, achieved through layer-by-layer deposition of titania*

The starting substrate in the form of large sheets of FTO-covered glass was cut to 8 × 8 cm sized squares. The substrate was cleaned by sonication in a solution of sonoswiss cleaner (2%), followed by rinsing with tap water, milli-Q water and EtOH. The glass was then dried under an air flow and cleaned in a UV/ozone cleaner for 20 min. One layer of titania was applied to the surface by following a spin-coating procedure: the cleaned glass sheets were put in a spin coater, where vacuum was applied to hold the glass sheets in place. 1.5 mL of titania precursor solution consisting of 40 mL EtOH, 4.4 mL 38% aqueous HCl, 4.0 mL titanium ethoxide and 1.0 mL H_2O was applied to the center of the surface with a syringe and spread thinly by spinning at 3000 rpm for 60 s (1 s for acceleration/deceleration). The bottom side of the glass was thoroughly cleaned with EtOH, before the glass sheet was sintered on a heating plate at 78 °C for 45 min and at 540 °C for 30 min. The whole spin coating cycle, including the sintering was repeated for each additional TiO_2 layer until the desired smoothness, as investigated by AFM, was reached. The glass was then cut into pieces of 2 × 2 cm. [16]

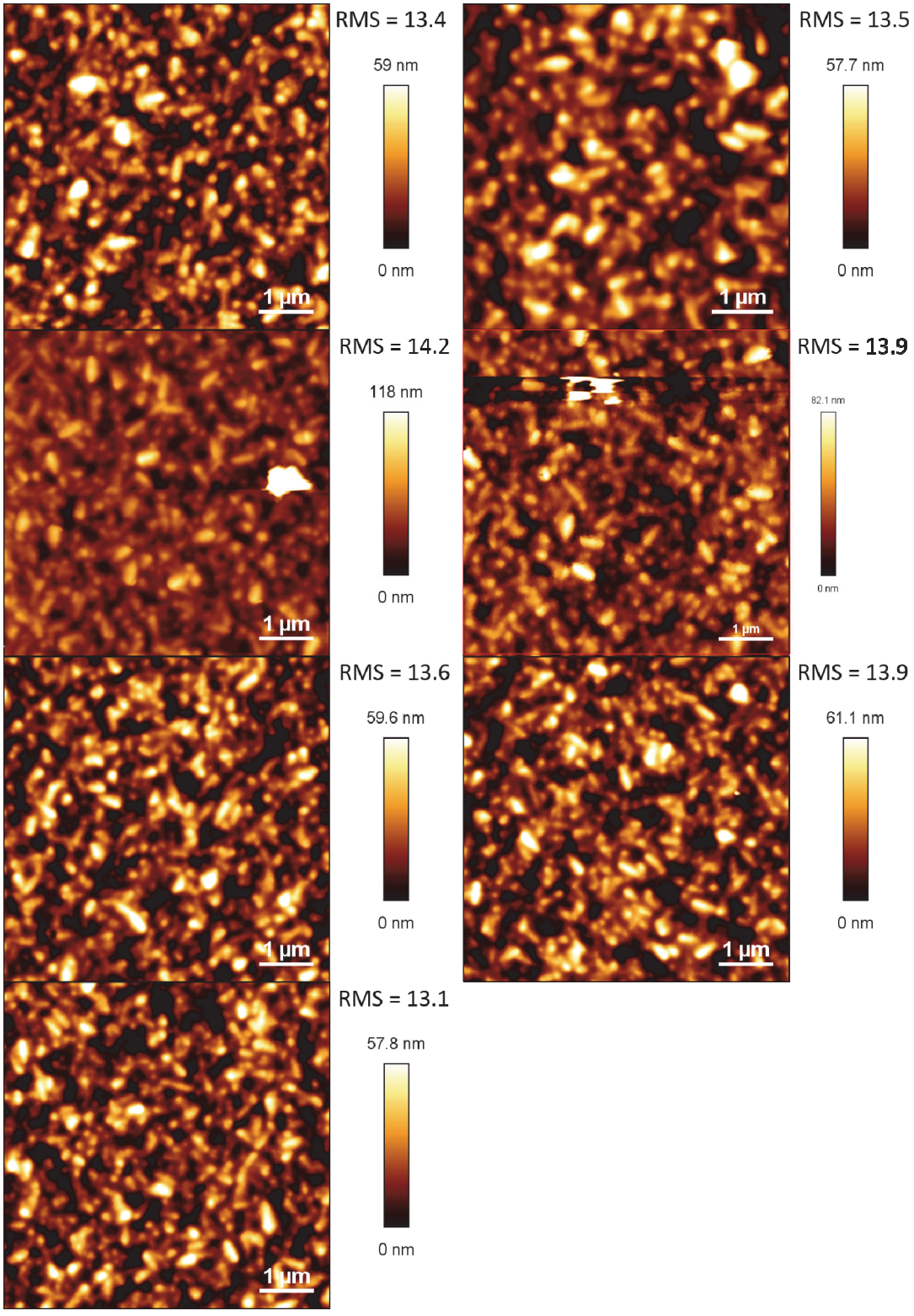

Figure 2.4. *AFM image of commercial FTO-covered glass after deposition of 2 titania layers*

Starting as described from commercial FTO-covered glass, the surfaces were gradually smoothed by spin-coating layers of titania, called compact layers. The roughness was determined by AFM imaging with 4 – 7 images being taken per sample. The R_{RMS} was

calculated for every image. Figure 2.4 shows AFM images taken after deposition of two compact layers. Compared to Figure 2.5 showing the starting material, FTO-covered glass, the edges appear less sharp. R_{RMS} values lie between 13.1 nm and 14.2 nm, with an average R_{RMS} of 13.6 ± 0.4 nm, which is already only half the roughness of the original FTO-covered glass.

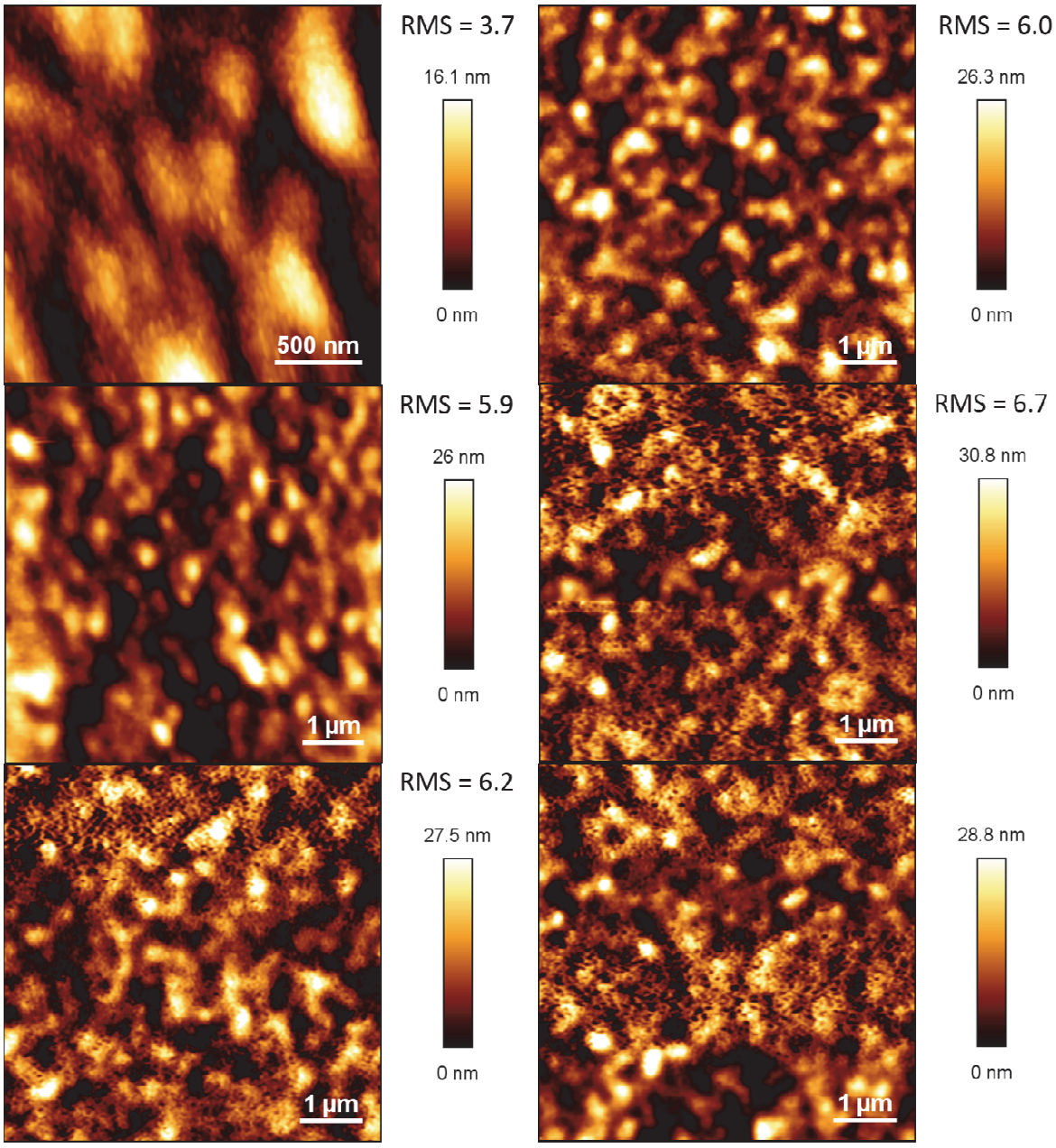

Figure 2.5. *AFM image of commercial FTO-covered glass after deposition of 4 titania layers*

After 4 compact layers, the surface could be smoothed even further resulting in R_{RMS} values between 3.7 and 6.7 nm, with an average R_{RMS} of 6.1±1.1 nm (Figure 2.5).

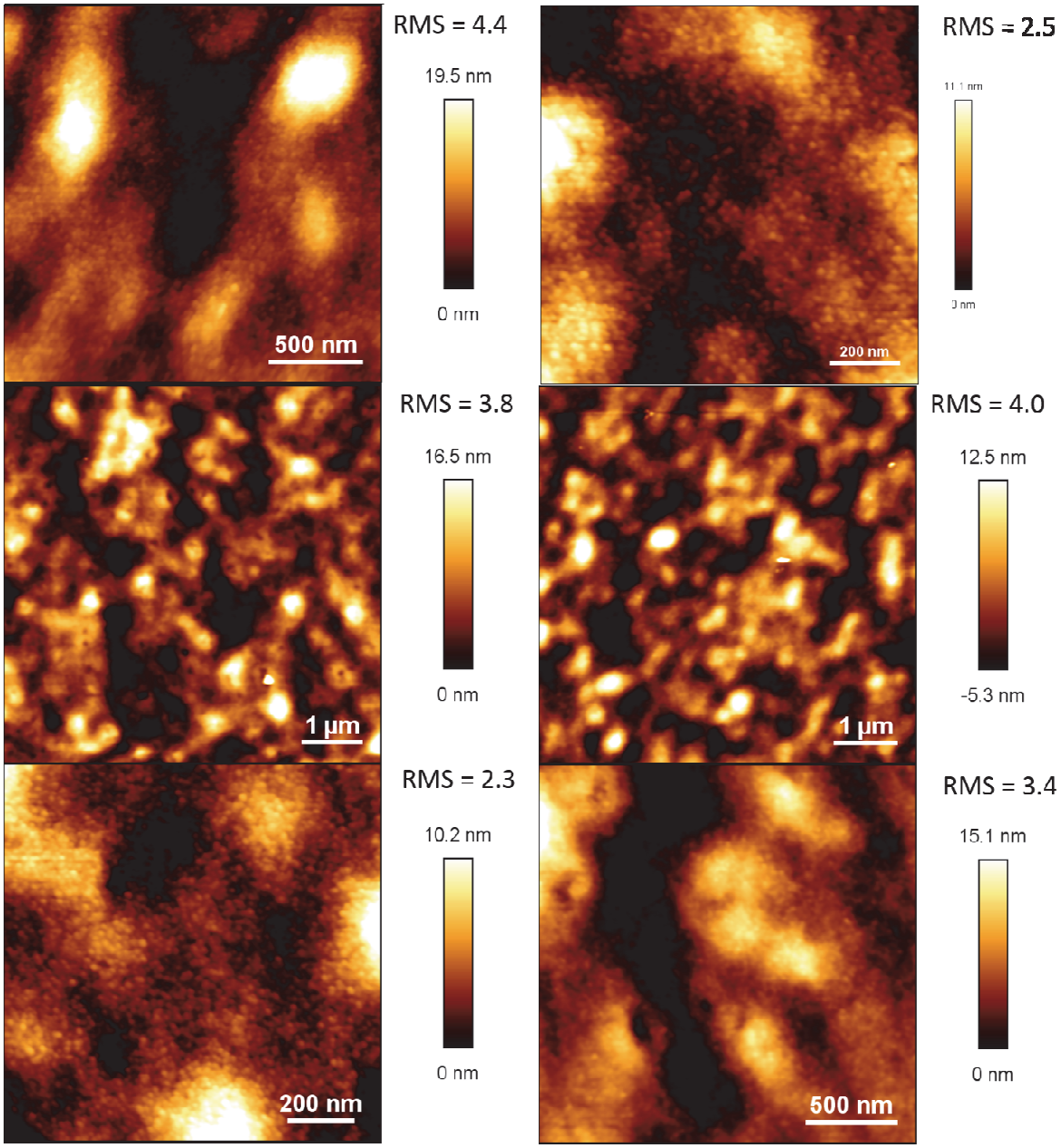

Figure 2.6. *AFM image of commercial FTO-covered glass after deposition of 5 titania layers*

Figure 2.6 shows AFM images taken after deposition of 5 compact layers. R_{RMS} values are decreased to 2.3 and 4.4 nm, with an average R_{RMS} of 3.9 ± 0.4 nm.

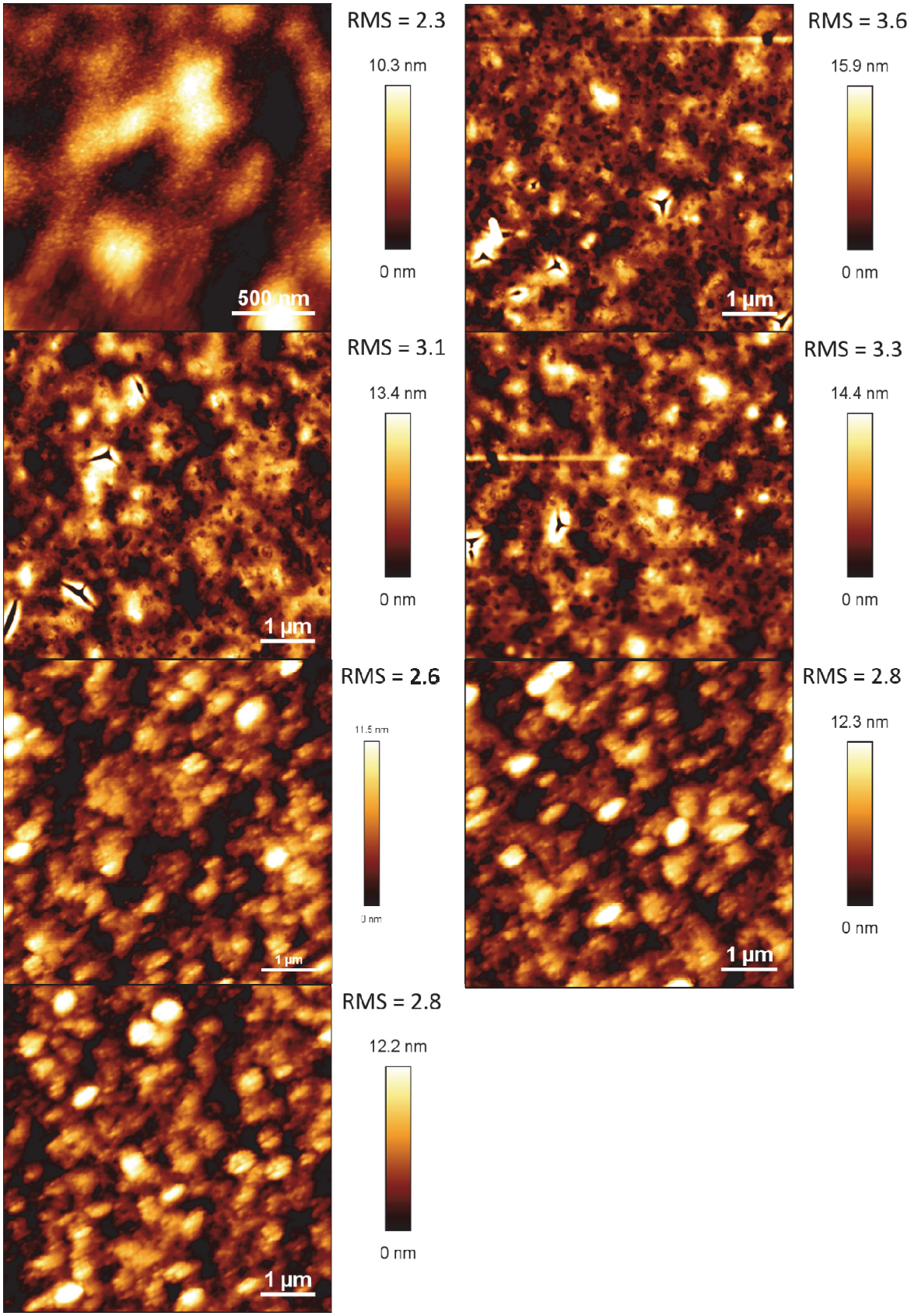

Figure 2.7. *AFM image of commercial FTO-covered glass after deposition of 6 titania layers*

Continuing the smoothing procedure, after the deposition of 6 compact layers (Figure 2.7) the R_{RMS} values are between 2.3 and 3.6 nm, with an average R_{RMS} of 2.9 ± 0.3 nm. Finally a good smoothing of the surfaces could be achieved after the deposition of 7 compact layers (Figure 2.8) with R_{RMS} values ranging from 1.8 to 2.2 nm, with an average R_{RMS} of 2.0±0.2 nm. For comparison, atomically flat mica surfaces reach a roughness of R_{RMS} = 0.2 nm. [17]

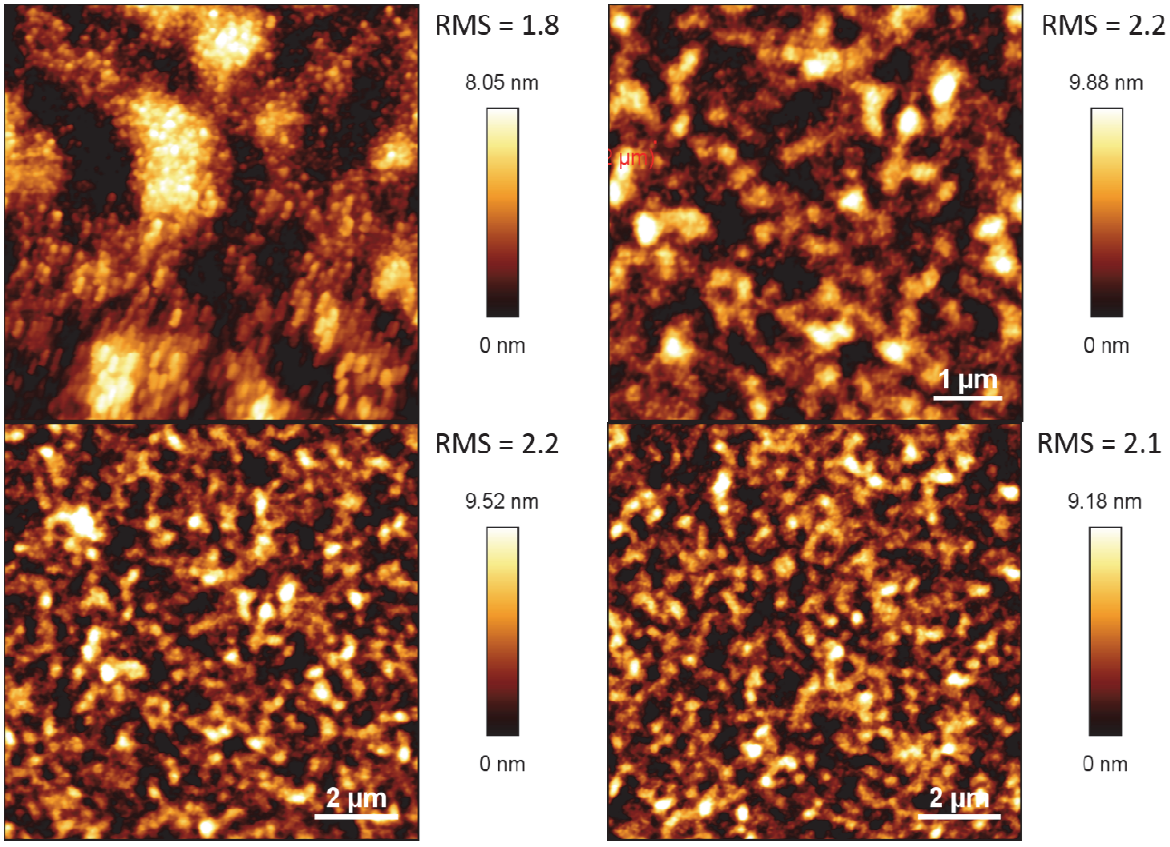

Figure 2.8. *AFM image of commercial FTO-covered glass after deposition of 7 titania layers*

To illustrate the smoothing process, starting from FTO-covered glass, the calculated R_{RMS} values for the various numbers of compact layers were plotted as a function of the number of compact layers (Figure 2.9). For comparison, the R_{RMS} value for the untreated commercial electrodes was also added (Figure 2.9*). The graph shows a smooth decrease in surface roughness up to 7 compact layers, where it seems to reach a plateau indicating that further treatment would not lead to significantly smoother surfaces. Compared to the starting substrate, FTO-covered glass, after the addition 7 compact layers the roughness was decreased to below 10%. Compared to the nanoparticulate titania of the "Test Cell Titania Electrodes" (Figure 2.9*), the roughness was decreased to approx. 20%. The successfully smoothed glass-supported titania surfaces could now be used for the next step.

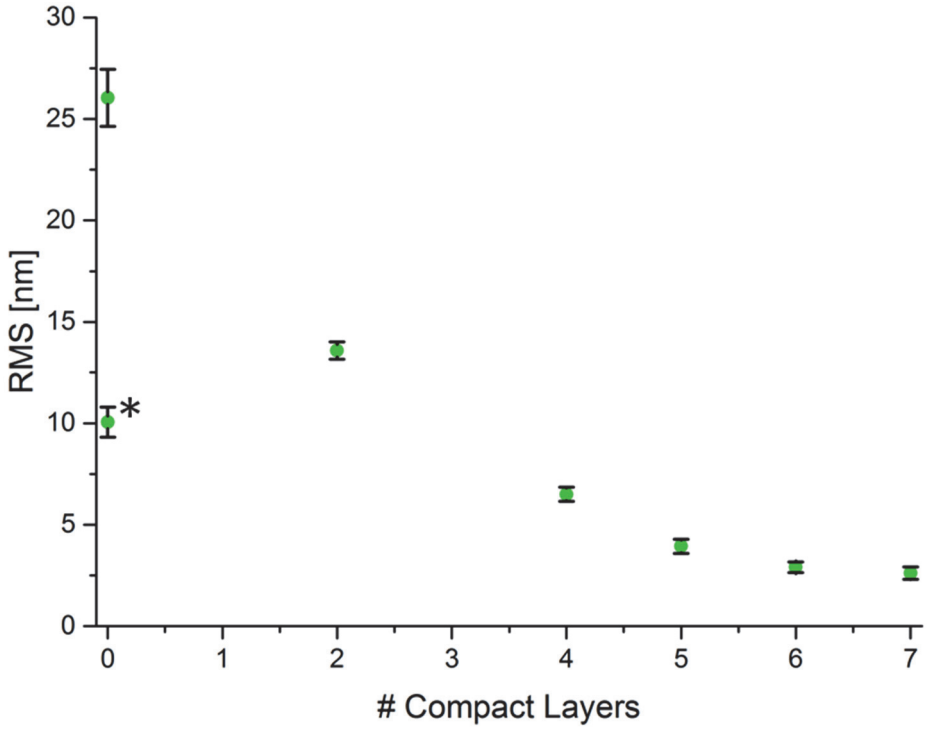

Figure 2.9. *Average root mean square (R_{RMS}) [16] roughness of different FTO-covered glass surfaces, which were modified by deposition of titania layers; R_{RMS} is derived from AFM measurements and presented as a function of the number of applied TiO_2 layers. The surface roughness decreases with increasing numbers of TiO_2 layers. For comparison the asterisk (*) indicates the R_{RMS} value for commercially available electrodes with mesoporous titania nanoparticles. For statistics only measurements of the same area (4x4 µm) were used.*

Conclusion

On the way to immobilizing polymersomes on a solid support using a metal complex linking the two together, this chapter focused on the surface that is used as the substrate. We focused on titania in the form of nanoparticles, which are commercially available as "Test Cell Titania Electrodes", or in the form of spin-coated layers on FTO-covered glass. Both, the "Test Cell Titania Electrodes" and the FTO-covered glass were imaged by AFM to gain insight into their surface topology. The titania nanoparticles have a spherical shape with approx. 50 nm in diameter, whereas the FTO seems to have a needle to rod like structure with sharp edges. From the AFM images the R_{RMS} values are calculated to quantify the surface roughness and gives an indication of the surface area. [18] To manipulate the surface roughness, we started from commercial FTO-covered glass and applied multiple layers of titania by spin-coating,

thereby decreasing the surface roughness and the surface area. The progress was monitored by AFM imaging of the coated surfaces and the decrease in roughness was quantified by calculating the R_{RMS} value from the images. The optimum smoothness was achieved after application of seven compact layers of spin coated TiO_2, reaching an average R_{RMS} of 2.0 ± 0.2 nm. This means the original surface roughness of FTO-covered glass was reduced to below 10%. This compares to around 20% of the roughness of nanoparticulate titania.

References

[1] G. Gunkel-Grabole, S. Sigg, M. Lomora, S. Lörcher, C. G. Palivan, W. P. Meier, *Biomater. Sci.,* 2015, **3**, 25.

[2] J. M. Choi, B. Yoon, K. Choi, M. L. Seol, J. M. Kim, Y. K. Choi, *Macromol. Chem. Phys.*, 2012, **213**, 610.

[3] W. Dowhan, *J. Biol. Chem.,* 2017, **292**, 10755.

[4] S. Belegrinou, J. Dorn, M. Kreiter, K. Kita-Tokarczyk, E.-K. Sinner, W. Meier, *Soft Matter*, 2010, **6**, 179.

[5] J. Vincent, *Structural Biomaterials*, Princeton Univ. Press, New Jersey, USA, 1990.

[6] A. H. Simmons, C. A. Michal, L. W. Jelinski, *Science,* 1996, **271**, 84.

[7] G. Gunkel-Grabole, C. Palivan, W. Meier, *Macromol. Mater. Eng.,* 2017, **302**, 1600363.

[8] R. Barbey, L. Lavanant, D. Paripovic, N. Schüwer, C. Sugnaux, S. Tugulu, H.-A. Klok, *Chem. Rev.*, 2009, **109**, 5437.

[9] S. Sun, A. M. Sendecki, S. Pullanchery, D. Huang, T. Yang, P. S. Cremer, *Langmuir*, 2018, **34**, 9015.

[10] Z. F. Yin, L. Wu, H. G. Yang, Y. H. Su, *Phys. Chem. Chem. Phys.*, 2013, **15**, 4844.

[11] M. A. M. Al-Alwani, A. B. Mohamad, N. A. Ludin, A. A. H. Kadhum, K. Sopian, *Renewable Sustainable Energy Rev.*, 2016, **65**, 183.

[12] S. Sharma, B. Siwach, S. K. Ghoshal, D. Mohan, *Renewable Sustainable Energy Rev.*, 2017, **70**, 529.

[13] K. Kalyanasundaram, A. Hagfeldt, G. Boschloo, L. Sun, L. Kloo, H. Pettersson, *Chem. Rev.*, 2010, **110**, 6595.

[14] B. Bozic-Weber, E. C. Constable, C. E. Housecroft, *Coord. Chem. Rev.*, 2013, **257**, 3089.

[15] R. R. L. De Oliveira, D. A. C. Albuquerque, T. G. S. Cruz, F. Yamaji, F. Leite, in *Atomic Force Microscopy - Imaging, Measuring and Manipulating Surfaces at the Atomic Scale*, Ed. V. Bellitto, Intech, London, England, 2012, Ch. 7.

[16] A. C. Arango, L. R. Johnson, V. N. Bliznyuk, Z. Schlesinger, S. A. Carter, H. H. Hörhold, *Adv. Mater.,* 2000, **12**, 1689.

[17] Q. Lu, J. Wang, A. Faghihnejad, H. Zeng, Y. Liu, *Soft Matter*, 2011, **7**, 9366.

[18] J. Qu1, A. J. Shih, *Machining Sci. Technol.*, 2003, **7**, 281.

Chapter 3

The Linker –Optimization of SALSAC approach for iron complexes

Abstract

Towards the development of active surfaces by immobilizing compartmentalized nanounits on solid surfaces, this chapter focuses on the linker, that connects the two. After the successful preparation of a smooth solid surface of titania covered glass, this chapter addresses the anchoring of a metal complex linker onto these surfaces. The aim finally is to immobilize polymersomes on a solid surface and a linker complex to connect the two components. We selected an iron terpyridine complex with an $[Fe(tpy)_2]^{2+}$ core. Suitably functionalized, this can serve as a binding unit for the surface and can also be used to connect to the polymersome. First, the terpyridine ligands had to be synthesized. Afterwards the anchoring of the iron terpyridine complex on a semiconductor (titania) surface via the SALSAC approach (´Surface-as-ligand, surface-as-complex´) could be optimized. We found that some solvents, like EtOH, MeCN and ethoxyethanol, were able to stabilize a surface bound iron terpyridine complex, which allows for a straightforward stepwise assembly of the $[Fe(tpy)_2]^{2+}$-complex. In addition we found that the anchoring ligand can, to a small extent, displace a coadsorbant. Further, water, saline, TES and HEPES buffers cause less decolorization of the surface and are considered acceptable for this system whereas phosphate buffered saline (PBS) is very effective at desorbing the $[Fe(tpy)_2]^{2+}$-complex off the surface and should therefore be avoided. Finally to confirm that the spin-coated titania layers did not change the desired ability of the surface to bind anchoring ligands and therefore $[Fe(tpy)_2]^{2+}$, the complex was assembled on the smooth surfaces. Its presence on the surface was successfully confirmed by cyclic voltammetry.

Motivation and Problem Definition

The aim of this thesis is to bind polymersomes to a titania surface on a solid support (glass). The polymer vesicles were to be linked to a titania semiconductor surface through the assembly of an iron terpyridine complex by application of the SALSAC approach (Figure 3.1). [1]

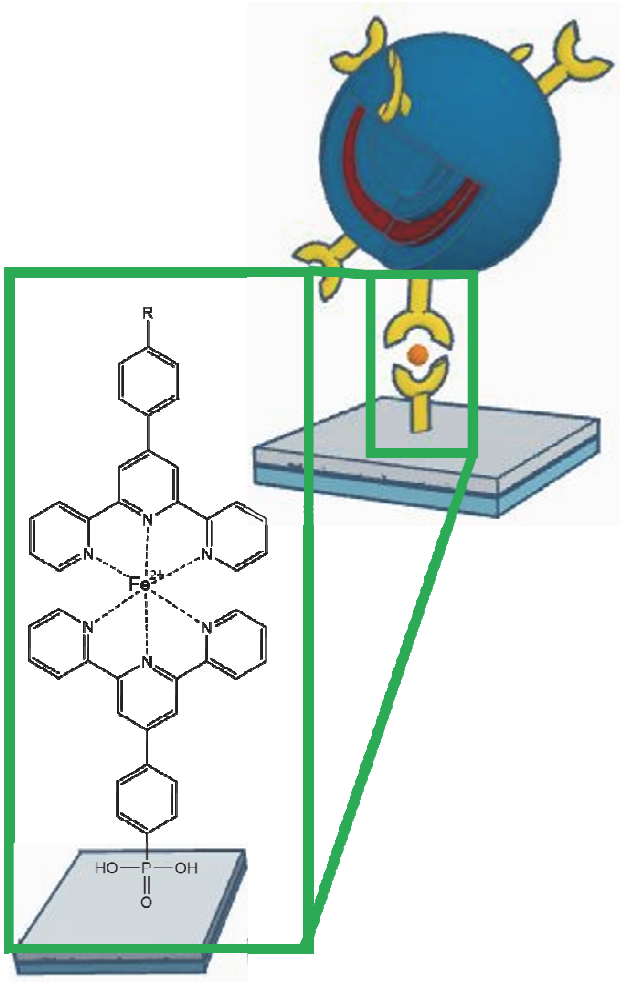

Figure 3.1*. Schematic illustration of the complex used to immobilize polymersomes on a solid surface.*

The SALSAC approach, the ´Surface-as-ligand, surface-as-complex´ strategy, was initially developed for stepwise assembly of various copper(I) complexes on a titania surface. [2] It is popular in dye-sensitized solar cell applications [3] and the general procedure is shown in Figure 3.2. In this method two routes lead to the surface bound complex on the nanoparticulate titania surface: ligand exchange (Figure 3.2 a-b-c) or consecutive, stepwise assembly (Figure 3.2a-b-d-c). For the assembly by ligand exchange, a titania covered surface

is immersed into a ligand solution. This anchoring ligand bears a carboxylic or phosphonic acid anchoring group, which can covalently attach to the titania surface. The adsorbed ligand possesses a metal binding site. In a second step, the surface is treated with a homoleptic metal complex of the type $[M(L_{ancillary})_2]^{n+}$, in which the ancillary ligand bears a metal-binding site and no anchoring site. Ligand exchange leads to the surface-bound complex $[M(L_{ancillary})(L_{anchor})]^{n+}$. Coming to the stepwise assembly, the titania covered surface is first immersed in the anchoring ligand solution, yielding the surface-bound anchoring ligand. Secondly, the anchoring ligand binds the metal upon dipping the surface in a solution of a metal salt. The last treatment is with a solution of the ancillary ligand, giving the surface bound complex $[M(L_{ancillary})(L_{anchor})]^{n+}$. This method allows for the metal complex to be assembled directly on the surface and it avoids the synthesis and purification of the complex prior to adsorption. The assembly can be performed in ambient conditions and at room temperature, a process that saves time and resources. The processes, especially the consecutive anchoring ligand-metal-ancillary ligand treatment, have a high atom efficiency and reduce waste, while allowing for a faster screening of different ligands.

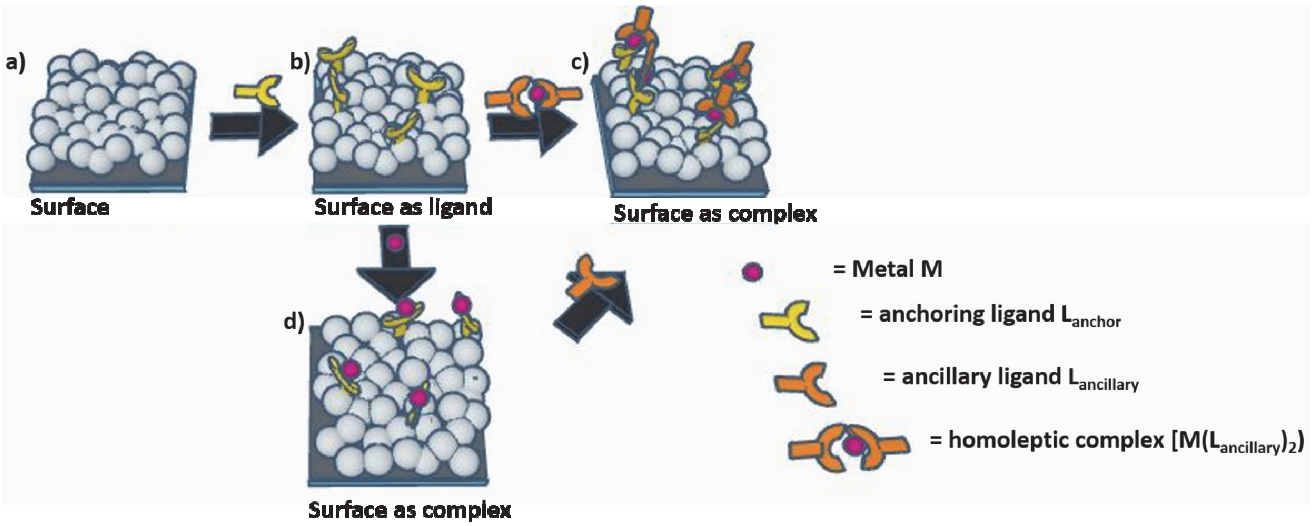

Figure 3.2. *Schematic illustration of two ´Surface-as-ligand, surface-as-complex´ strategies. Ligand exchange methodology (top): The surface a) is treated with an anchoring ligand (yellow), that adsorbs onto the titania surface, giving the surface-bound anchoring ligand b). The surface b) is then treated with homoleptic complex, which yields the surface bound heteroleptic complex c). Subsequent, stepwise assembly (bottom): The first step is the same. In a second step, the surface-bound anchoring ligand b) is reacted with a metal ion (purple), to give the metal-anchoring ligand complex d). Treatment with an ancillary ligand leads to the surface bound heteroleptic complex c).*

Copper(I) complexes tend to be very labile [4], which is an advantage allowing for the ligand exchange assembly route. However, when binding nanostructures to a surface, stability of the complex linking the structures to the surface is a must-have requirement. Iron(II)-terpyridine complexes tend to be thermodynamically stable, but show a useful reversibility upon the addition of ethylenediaminetetraacetic acid (H_4EDTA), [5] and their MLCT band can be used to detect complex formation. The binding motif in our strategy was therefore based upon the assembly of $[Fe(tpy)_2]^{2+}$. The SALSAC approach was originally based on copper(I) 1,10-phenanthroline or 2,2'-bipyridine complexes. [3] In this chapter we describe the adaption and optimization to iron(II)-terpyridine complexes.

Synthesis of 2,2':6',2''-terpyridine ligands

To immobilize polymer vesicles on the surface, a linker, in our case a $[Fe(tpy)_2]^{2+}$ complex, which is able to anchor on the semiconductor surface, is required. Therefore terpyridine ligands **1**-**4** were synthesized.

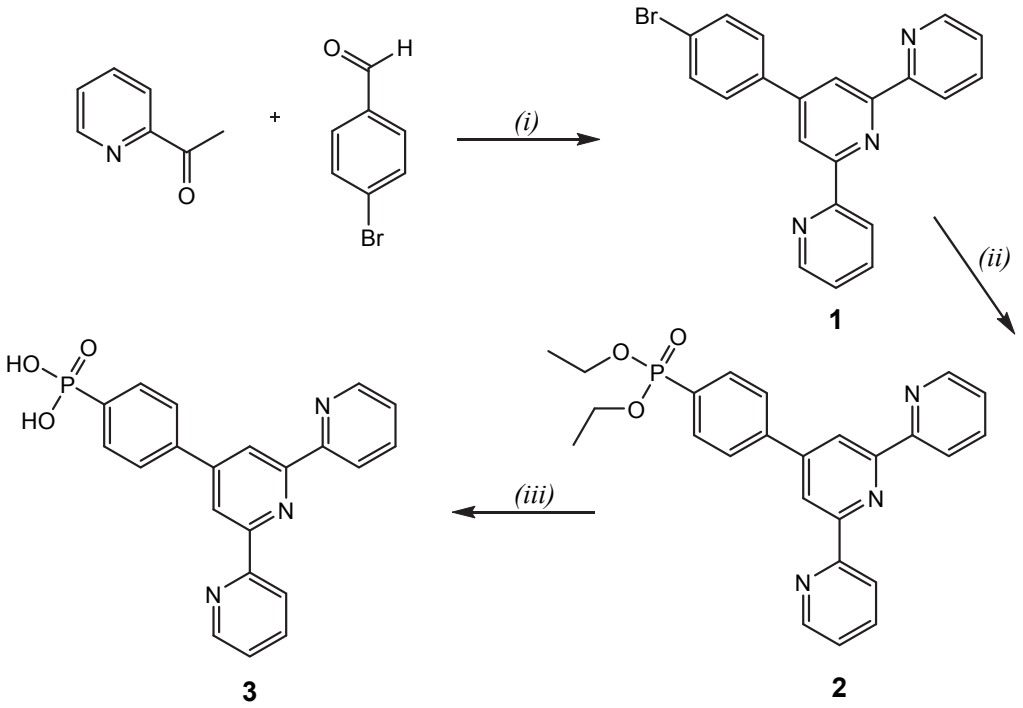

Figure 3.3. *(i) KOH, NH_3, EtOH, 24h, yield 12%; (ii) diethyl phosphite, triethyl amine, tetrakis(triphenyl phosphine)palladium, toluene, under N_2, 90°C, 4h, yield 63%; (iii) bromotrimethylsilane, DCM, under N_2, 20h, yield 82%.*

The Kröhnke method offers a very convenient way to synthesize aromatic substituted terpyridines, due to the simplicity of the one-pot procedure [6] and Figure 3.3 summarizes the synthesis of **1** and **2**. These ligands were characterized by 1H-NMR spectroscopy (Figure 3.4 and 3.5) and were in accord with the literature. [7, 8]

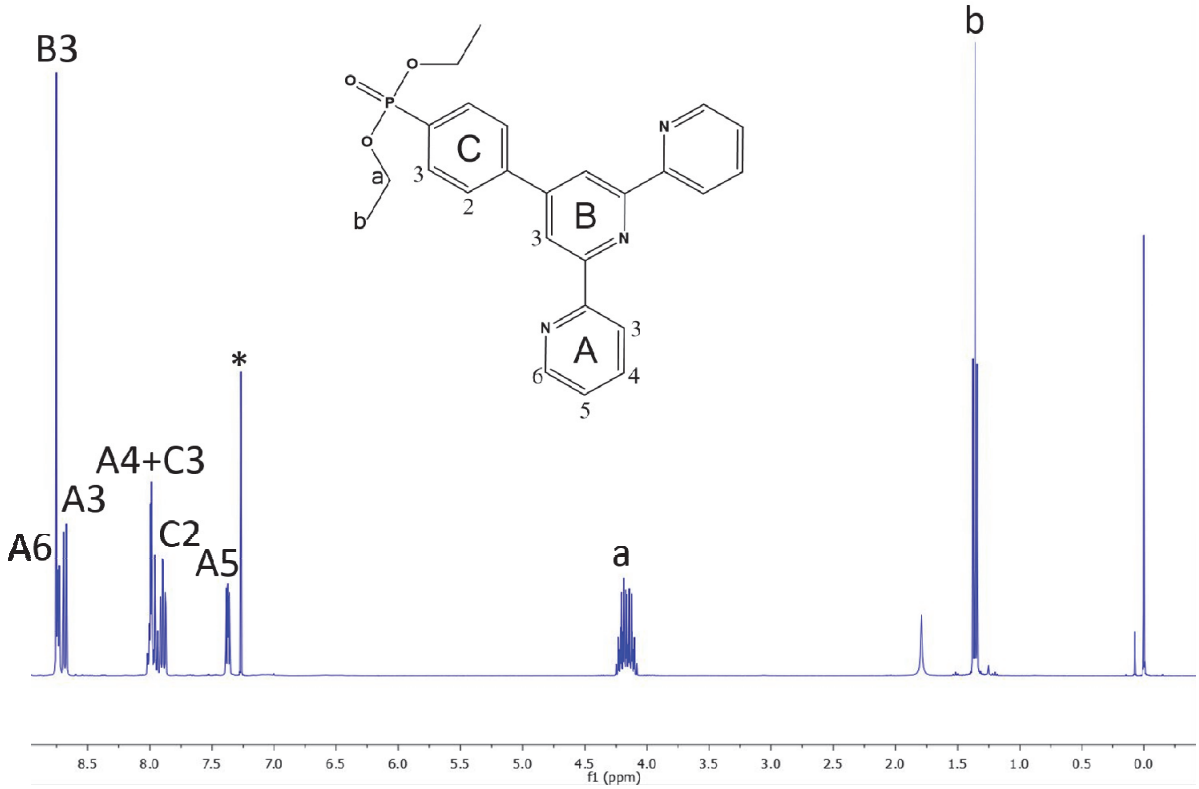

Figure 3.4. *400 MHz ^{1}H-NMR spectrum in $CDCl_3$ (*) of diethyl 4-(2,2':6',2''-terpyridin-4'-yl)phenylphosphonate (**1**).*

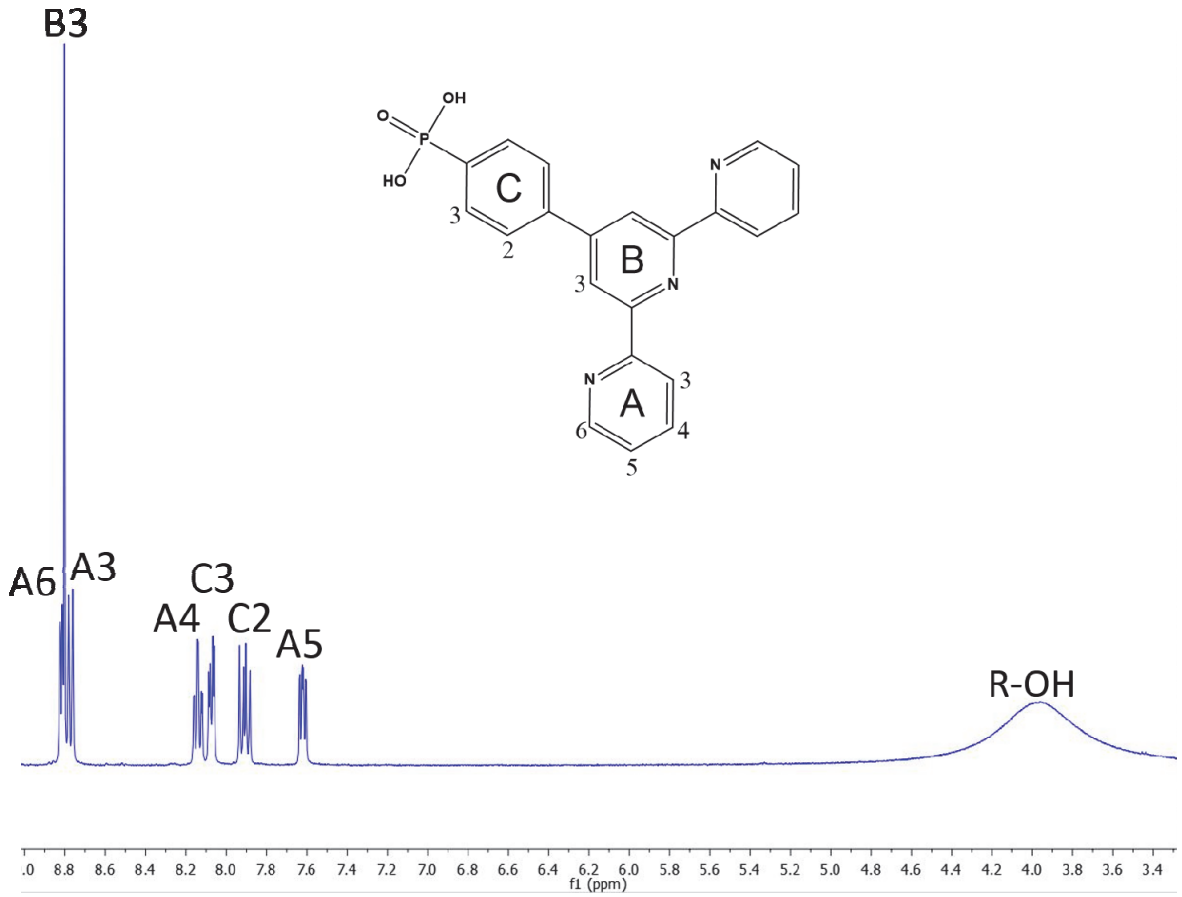

Figure 3.5. *400 MHz ^1H NMR spectrum in $(CD_3)_2SO$ (*) of (4-([2,2':6',2''-terpyridin]-4'-yl)phenyl)phosphonic acid (ligand **2**).*

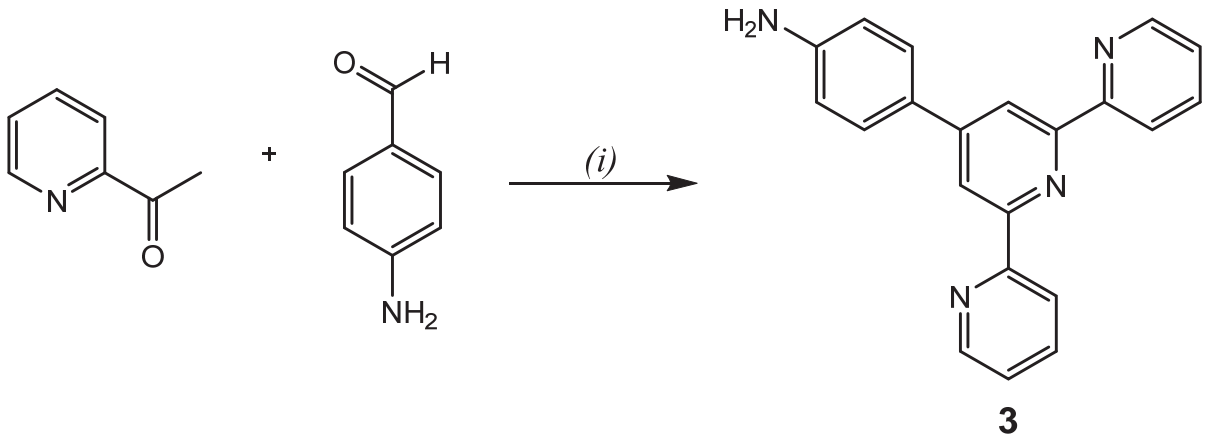

Figure 3.6. *(i) $[NH_4][O_2CMe]$, acetamide, heat, 2h; NaOH (aq), heat, 2h; $MeCO_2H$, 48% HBr (aq); $NaHCO_3$, $CHCl_3$, yield 8%*

Ligands **3** to **4** were also prepared using Kröhnke methodology (e.g. Figure 3.6) and the ^{1}H-NMR spectra matched the literature data (Figure 3.7-3.8). [7, 9-11]

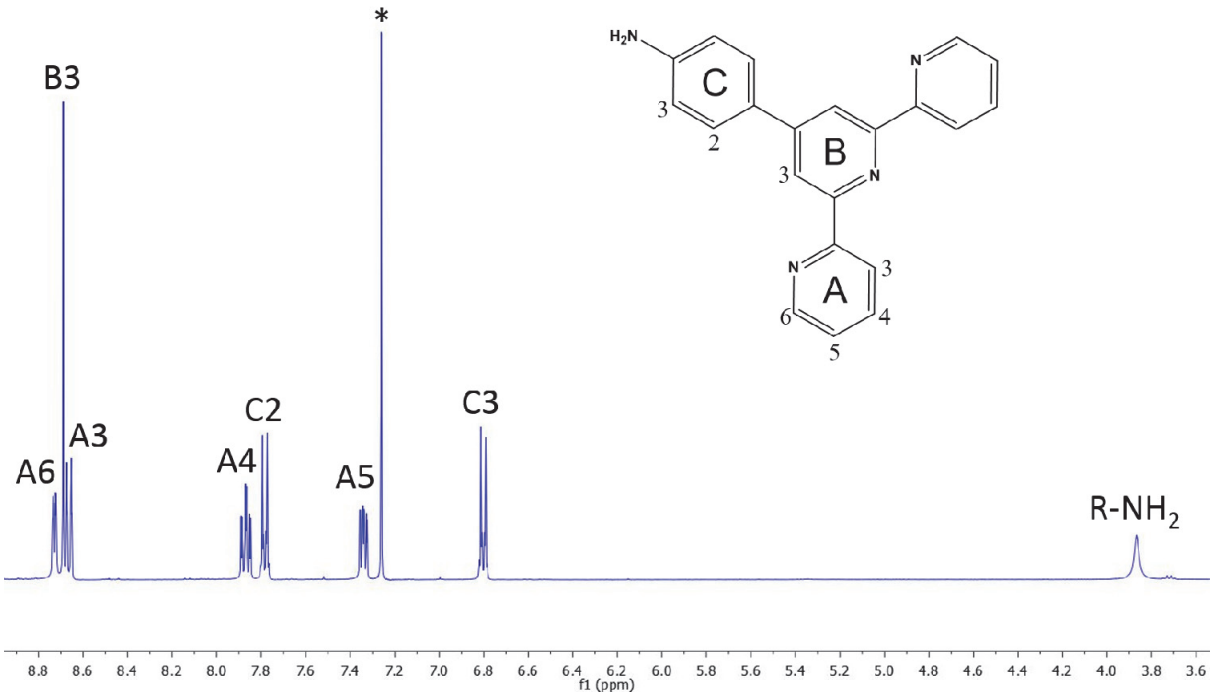

Figure 3.7. *400 MHz ^{1}H NMR spectrum in $CDCl_3$ (*) of 4-([2,2':6',2''-terpyridin]-4'-yl)aniline (ligand **3**).*

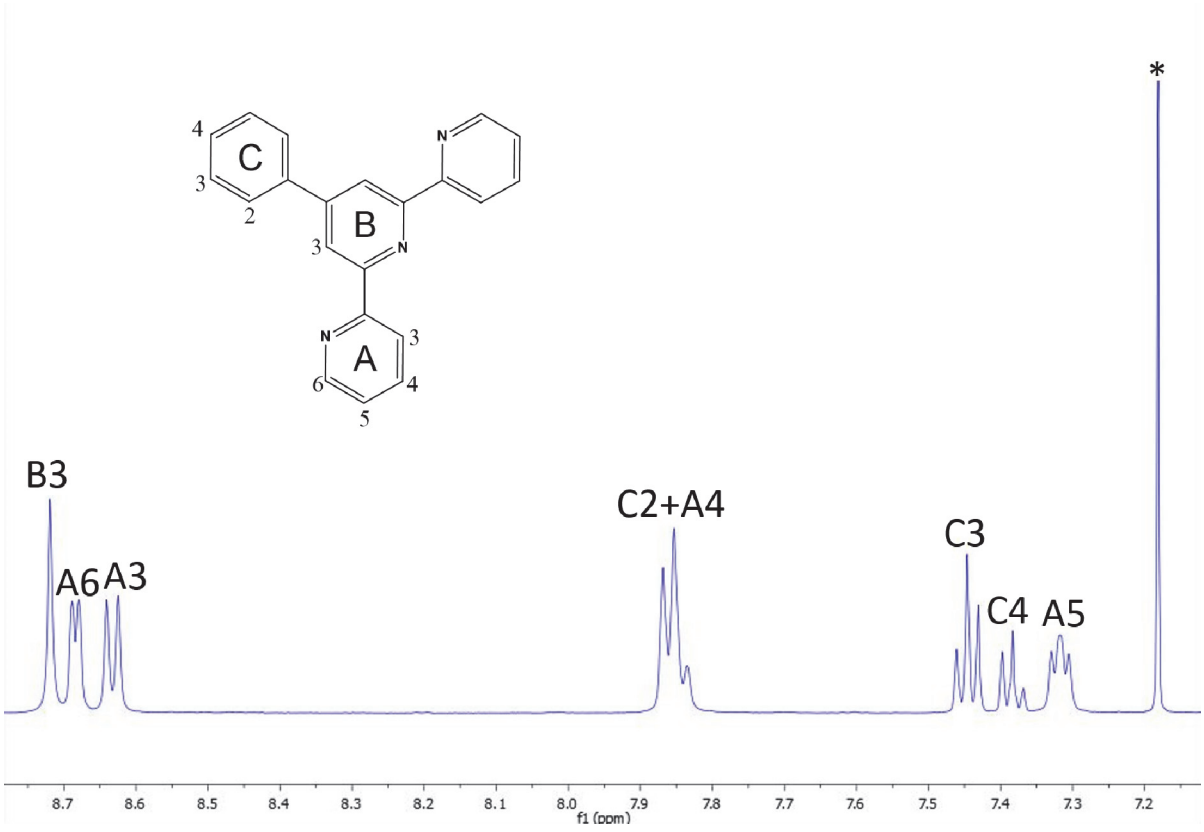

Figure 3.8. *400 MHz ^{1}H NMR spectrum in $CDCl_3$ (*) of 4'-phenyl-2,2':6',2''-terpyridine (ligand **4**).*

Surface anchoring of anchoring ligands and stepwise assembly procedure via SALSAC approach through consecutive treatment with ligand and metal salt solutions

To anchor polymer vesicles to the titania surface by stepwise assembly of a surface-bound $[Fe(tpy)_2]^{2+}$ complex, the SALSAC approach had to be adapted to conditions suitable for our system. For optimization purposes, commercially available electrodes were used as the substrate. They are covered with nanoparticulate titania, increasing the surface area greatly. The larger the surface area, the more complex can bind to the surface. This allows us to monitor the complex assembly, accompanied by intense purple coloration of the surface, by eye. The FTO/TiO_2 surfaces were cleaned and subsequently treated with ligand and aqueous iron(II) chloride solutions as described. Test Cell Titania Electrodes were washed with EtOH (HPLC) and dried at 60°C. Following the washing, they were heated on a heating plate at 450°C for 30 min. The FTO/TiO_2 surfaces were let to cool to 80-100°C and then submerged in solution 1 for 1 day (Table 2.1). They were then washed with DMSO (HPLC) and EtOH (HPLC) and dried at 60°C, followed by dipping into solution 2 for 1 day. Afterwards, they were washed with water (Milli-Q) and EtOH (HPLC), dried at 60°C and dipped into solution 3 for 3 days. Finally, they were washed with DMSO (HPLC) and EtOH (HPLC) and dried at 60°C. This procedure was used to prepare a range of different functionalized surfaces with and without coadsorbants. The reason for the different solution compositions are discussed in the following section.

Solution 1 contains compound **2** (“anchoring ligand”, 1mM) and different coadsorbants. Coadsorbant concentrations are given in Table 2.2. Solution 2 is iron(II) chloride in water (solution 2a) or EtOH (solution 2b). Solution 3 is ligand 2 (“anchoring ligand”, 1mM), functioning as ancillary ligand.

Sample	Compound	Concentration	Solvent	Dipping time [h]
Solution 1	Ligand (**2**) (anchoring ligand) + coadsorbant	1 mM	DMSO	24
Solution 2	$FeCl_2$	sat./2 mM	a) water b) EtOH	24
Solution 3	Ligand (**2**) (capping ligand)	1 mM	DMSO	72

Table 2.1. *Makeup of dipping solutions for assembly* $[Fe(\mathbf{2})_2]^{2+}$*; counter ion is chloride*

Sample code	Coadsorbant	Concentration of Coadsorbant	Ratio of Coadsorbant to anchoring ligand (**2**)
1:100 Phen	Phenylphosphonic acid	100 mM	100:1
1:10 Phen	Phenylphosphonic acid	10 mM	10:1
1:100 Decyl	Decylphosphonic acid	100 mM	100:1
1:10 Decyl	Decylphosphonic acid	10 mM	10:1
1:100 tBu	tert-Butylphosphonic acid	100 mM	100:1
1:10 tBu	tert-Butylphosphonic acid	10 mM	10:1
ligand **2**	none	0 mM	0:1

Table 2.2. Variations of solution 1; ligand **2** is always 1mM; solvent is always DMSO.

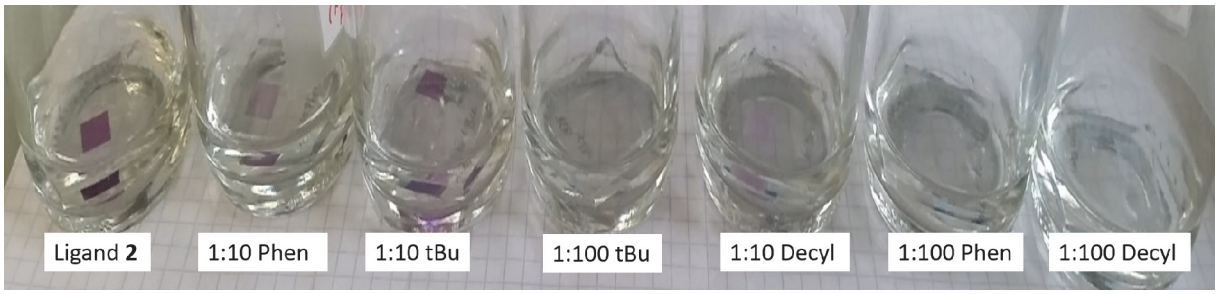

Figure 3.9. Surfaces after submerging in solution 2a), aqueous $FeCl_2$, for 1 day.

Solvent effects on stepwise assembly of $[Fe(tpy)_2]^{2+}$

Complex formation was monitored through the development of an intense purple coloration caused by the MLCT absorption band at 575 nm. For comparison, bis(4'-phenylterpyridine)iron(II) perchlorate in acetonitrile has an absorption maximum at λ_{max} = 565 nm (ε = 22 600 M^{-1} cm^{-1}). [12]

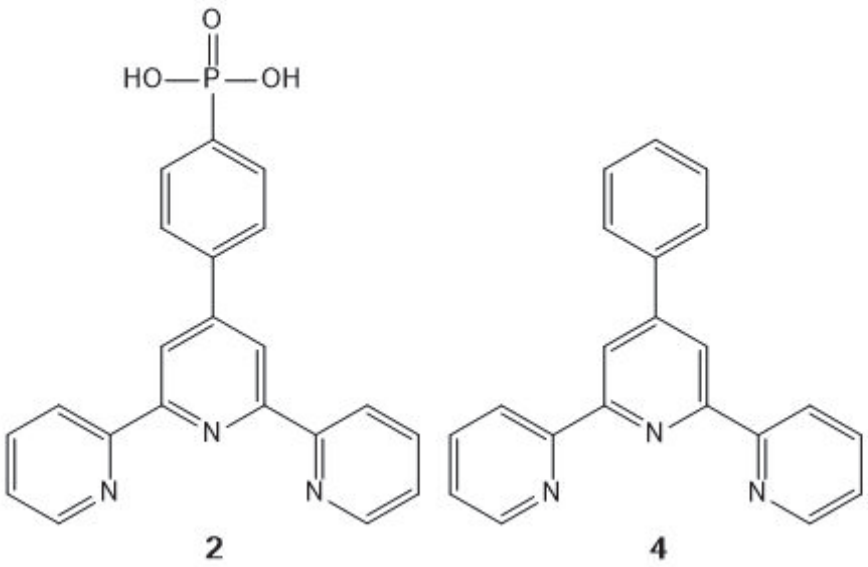

Scheme 3.1. Structures of 4-(2,2':6',2''-terpyridin-4'-yl)phenylphosphonic acid (ligand **2**) and 4'-phenyl-2,2':6',2''-terpyridine (ligand **4**)

To build the iron complex, 4-(2,2':6',2''-terpyridin-4'-yl)phenylphosphonic acid (ligand **2**, Scheme 3.1) is used as an anchoring ligand and also as the ancillary ligand in the optimization process. The $[Fe(\mathbf{2})_2]^{2+}$ complex is generated in a three-step process as outlined in Figure 3.10. The $[Fe(\mathbf{2})_2]^{2+}$ complex is produced by consecutive treatment of the substrate with three solutions, whose composition is given in Table 2.1.

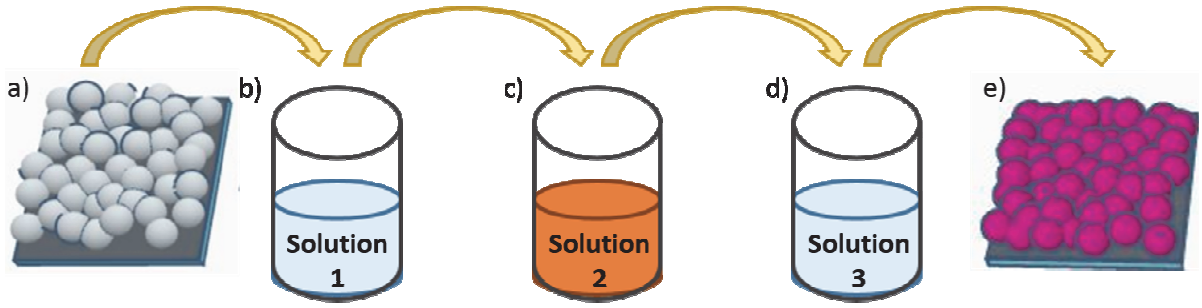

Figure 3.10. *Schematic illustration of the surface treatment. The compositions of solutions 1, 2 and 3 are given in Tables 2.1 and 2.2*

The first step consists of submerging the surface (Figure 3.10a) in a solution of compound **2** (Figure 3.10b) in DMSO. For the second treatment either an aqueous iron(II) chloride solution (solution 2a) or iron(II) chloride in EtOH (solution 2b) was used (Figure 3.10c). In a last step, the surfaces are treated with a solution of compound **2** (Figure 3.10d) in DMSO. When the surfaces were treated with aqueous iron(II) chloride, they immediately showed an intense

purple coloration, indicating the formation of surface-bound $[Fe(\mathbf{2})_2]^{2+}$ chromophore (Figure 3.11a and b), probably due to a complex with two surface-bound **2** ligands (the protonation state of **2** on the surface and in the complex is undetermined).

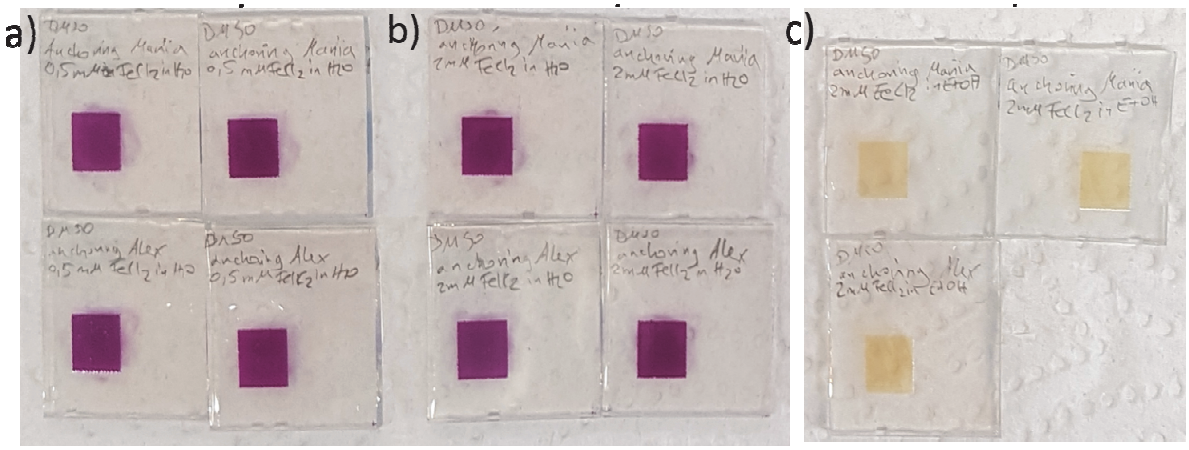

Figure 3.11. *Substrates treated consecutively with a) solution of **2** and 0.5 mM iron(II) chloride in water, b) compound **2** and 2 mM iron(II) chloride in water and c) compound **2** and 2 mM iron(II) chloride in EtOH.*

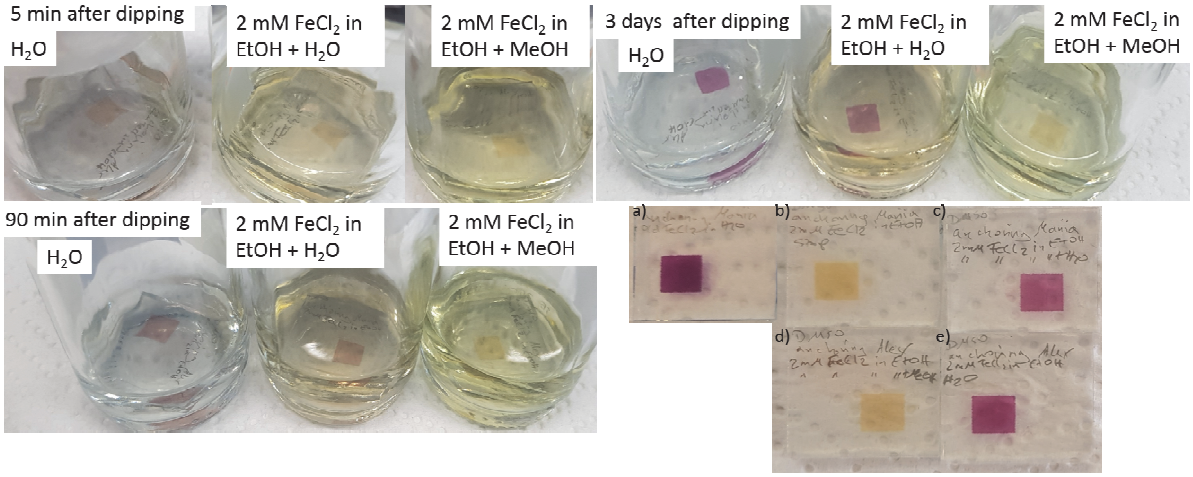

Figure 3.12*. Shows slow coloration of previously colourless surfaces bearing the $[Fe(\mathbf{2})(EtOH)_x]^{2+}$ solvato complex. a) Surface after treatment with solution 1 followed by iron(II) chloride in water b) Surface after treatment with solution 1 followed by iron(II) chloride in water c) Surface after treatment with solution 1 followed by iron(II) chloride in EtOH and re-submerged in a solution of iron(II) chloride in EtOH and water d) Surface after treatment with solution 1 followed by iron(II) chloride in EtOH and re-submerged in a solution of iron(II) chloride in EtOH and MeOH e) Surface after treatment with solution 1 followed by iron(II) chloride in EtOH and re-submerged in water*

The surfaces treated with iron(II) chloride in EtOH, did not show this coloration (Figure 3.11c), suggesting the formation of an $[Fe(\mathbf{2})Cl_n(solvent)_{3-n}]$ solvato complex. Re-submerging these

colorless surfaces in water or in a solution of iron(II) chloride in EtOH, to which water was added, slowly gives rise to purple coloring (Figure 3.12), indicating formation of a heteroleptic $[Fe(\mathbf{2})_2]^{2+}$ complex with one surface-bound **2** and one capping **2** ligand.

Variation of solvents used for the iron(II) chloride solutions (solution 2), showed the "protective solvent effect" in the sense that they prevented the homoleptic surface-bound $[Fe(\mathbf{2})_2]^{2+}$ chromophore from forming when EtOH, MeCN and ethoxyethanol were used (Figure 3.13). Instead, in water and MeOH the surfaces immediately showed purple coloration, indicative of homoleptic surface-bound $[Fe(\mathbf{2}_{surface})_2]^{2+}$ complex.

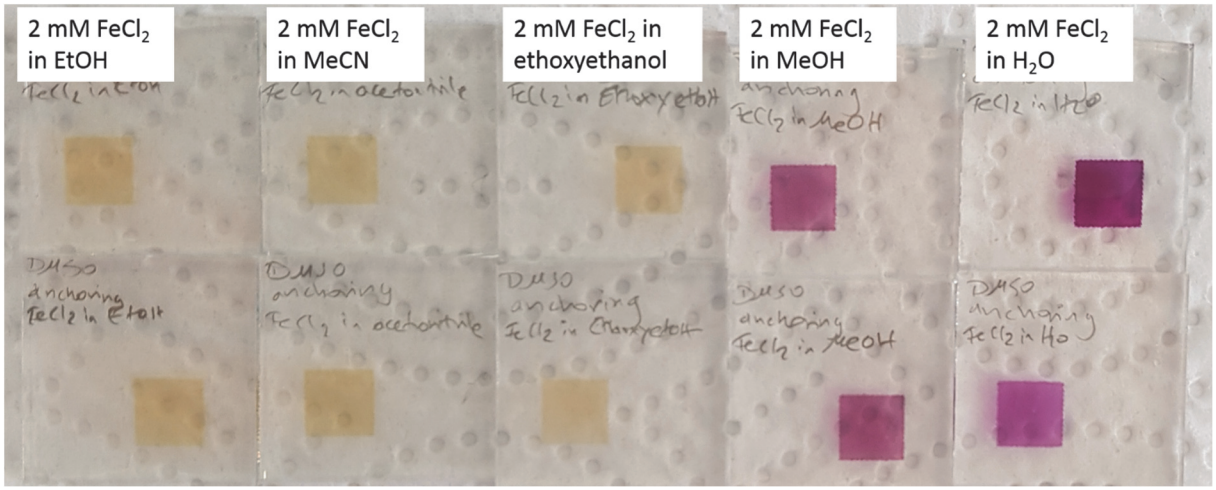

Figure 3.13. *Surfaces after treatment with solution 1 followed by iron(II) chloride in different solvents.*

Monitoring of stepwise assembly process via quartz crystal microbalance (QCM) measurement

The assembly of the $[Fe(tpy)_2]^{2+}$ complex on the surface is essential for linking the polymer vesicles to the surface. To confirm that the assembly process proceeded stepwise, the process was monitored with a quartz crystal microbalance measurement (QCM). The QCM measures frequency changes to the oscillation of a quartz crystal due to increase in mass on the crystal surface after consecutive treatment with the single components. Instead of on "Test Cell Titania Electrodes" (referred to as FTO/TiO_2 surfaces) as substrate, the iron bis-terpyridine complex was assembled on a titania-covered QCM sensor surface and monitored in real time. QCM sensor chips were treated in a UV/ozone cleaner for 10 min. They were then immersed in a 2% SDS solution for 30 min at RT, rinsed with water (milliQ), dried in a nitrogen flow and treated with UV/ozone for 10 min. [13, 14] The sensor was then mounted into the instrument

and the resonance frequency was determined. The measurement was started with DMSO until a stable baseline with frequency changes under 1 Hz/h was obtained. Flow rates were kept at 200 µL/min. During the measurement, the sensors were consecutively exposed to the dipping solutions (Table 2.1). Dipping in each solution was followed by rinsing with the corresponding solvent to rinse away non-attached compounds. The surfaces were consecutively exposed to DMSO, solution 2, DMSO, EtOH, iron(II) chloride in EtOH (2mM), EtOH, DMSO, solution 3 and DMSO and the frequency and dissipation changes were recorded in real time. Solution 1 consisted of a 1 mM solution of ligand **2**. Solution 2b was a 2 mM solution of iron (II) chloride in EtOH. Solution 3 was a 2 mM solution of 4'-phenyl-2,2':6',2''-terpyridine (ligand **4**). Every change of liquids during the measurement was continued until the frequency had been stabilized. After obtaining a stable baseline with DMSO, solution 1 was measured. Upon stabilization, DMSO flow is reinstated to remove any ligand that is not attached to the surface. The solvent is then changed to EtOH, followed by solution 2b and a rinse with EtOH. The solvent is then changed to DMSO, followed by solution 3 and a rinse with DMSO. The data was analyzed with the Sauerbrey layer model, in which the change in mass is assumed to be proportional to the negative change in frequency. N is the harmonic number and C is a constant.

$$\Delta m = -nC\Delta f$$

The Sauerbrey model is valid for small masses (compared to the crystal mass), that are rigidly adsorbed and evenly distributed. Representative data of the third and fifth overtones are presented in Figure 3.14. The data reveal a decrease in frequency (-55.1 Hz) after solution 1, indicative of surface bound ligand **2**. There is a second decrease in frequency (-92.4 - (-55.1) Hz = -37.3 Hz) after solution 2 and a third one after solution 3 (-149.0 - (-92.4) Hz = 56.6 Hz). A change in frequency by 1 Hz corresponds to an adsorbed mass of 17.7 ng per cm^2. [15] Therefore in our case it translates to 2.5 nmol/cm^2 of anchoring ligand (**2**) and 2.8 nmol/cm^2 of ancillary ligand (**4**), which is near a 1:1 ratio, as we would expect from the stoichiometry of the complex. The mass of added iron(II) chloride of 5.2 nmol/cm^2 would translate to roughly 2eq. compared to anchoring ligand (**2**), which is too high. If we consider the solvent being involved in the form of a Fe(**2**)Cl_n(solvent)$_{3-n}$ solvato complex, the calculated value would indicate, on average, three EtOH molecules per iron center, a result still in agreement with the expected stoichiometry.

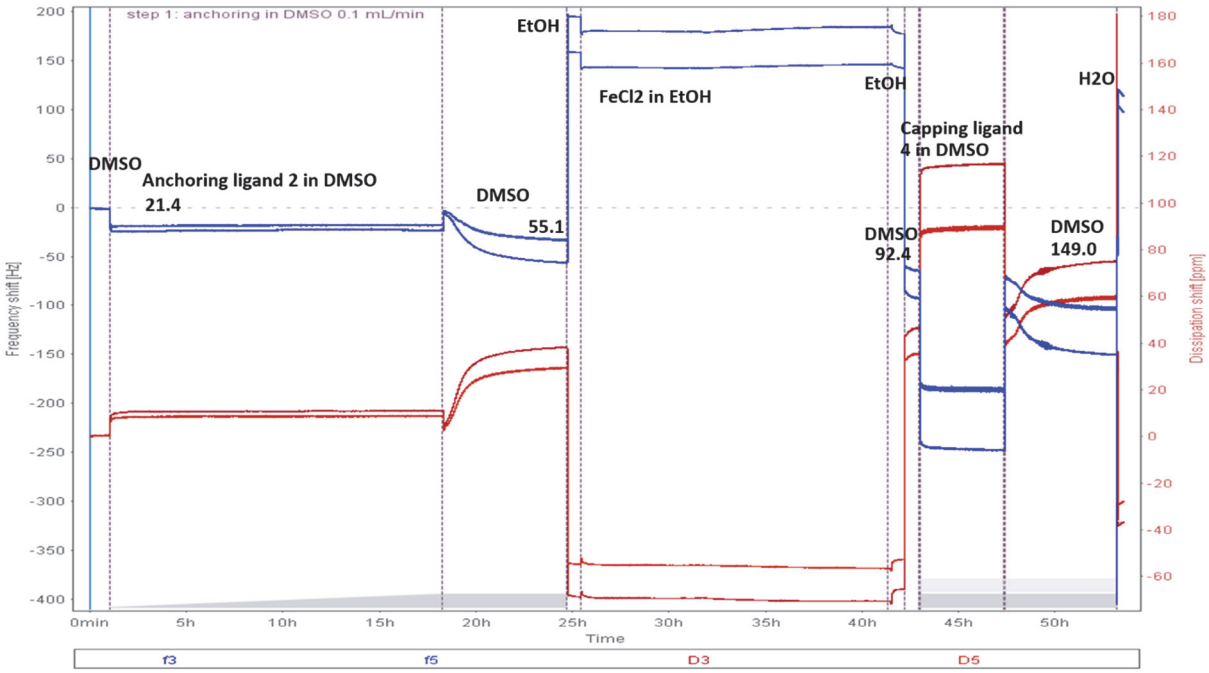

***Figure 3.14**. Representative QCM data (third and fifth overtone) for stepwise assembly of $[Fe(tpy)_2]^{2+}$ on the sensor surface. At 0-60 min the surface was rinsed with DMSO; at ca. 1-18h the surface was treated with ligand 2 in DMSO. At ca. 18h the surface was rinsed with DMSO to remove non adsorbed ligand 2 and left to stabilize until 25h, followed by rinsing with EtOH until 26h. Next, the surface was treated with iron(II) chloride in EtOH until approx. 40 h and rinsed with EtOH for 1h and with DMSO for 1 h. Then, the surface was flushed with phtpy (ligand 4) in DMSO for approx. 5 h, followed by rinsing with DMSO until frequency stabilized at 53h; Frequency shown in blue and dissipation in red; Frequency shifts [Hz] are marked on the figure.*

Coadsorbants for spatial separation of anchoring ligand in aqueous assembly

During optimization of the SALSAC approach for our iron(II) terpyridine system as a linker to bind polymersomes to the titania surface, we found that the solvent plays a key role in whether or not the homoleptic surface-bound $[Fe(\mathbf{2}_{surface})_2]^{2+}$ complex is formed. Our initial findings are summarized in Figure 3.15a and b illustrating the optimization of the SALSAC approach for $[Fe(tpy)_2]^{2+}$ motifs. The SALSAC approach is based upon the ability to functionalize a surface with an anchoring and metal-binding domain, and to react it with a metal ion, followed by an ancillary ligand to generate a surface-bound heteroleptic complex. We found that some solvents, e.g. EtOH, MeCN or ethoxyethanol, stabilize the $[Fe(tpy)]^{2+}$ moiety on the surface, enabling the SALSAC approach for the stepwise assembly of $[Fe(tpy)]^{2+}$ as illustrated in Figure 3.15a). In aqueous medium, however, we observe the typical purple

coloration, that is indicative of $[Fe(tpy)]^{2+}$-formation immediately after treatment of the surface anchored ligand with iron (Figure 3.15b). The purple color due to the homoleptic complex with two surface-bound anchoring ligands reduces the selectivity for the formation of heteroleptic surface species and needs to be minimized.

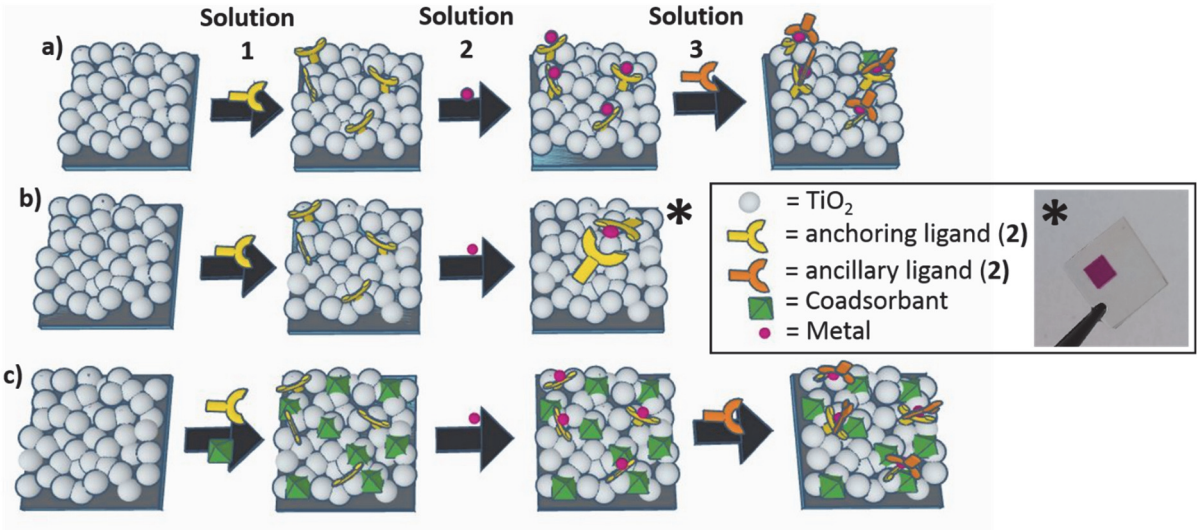

Figure 3.15. *Stepwise assembly of $[Fe(tpy)_2]^{2+}$ on the surface: a) The original SALSAC protocol in which the $[Fe(tpy)_2]^{2+}$ is assembled by consecutive treatment with anchoring ligand 2, iron(II) chloride and an ancillary ligand (here: ligand 2); b) Sequential adsorption of **2**, followed by aqueous $FeCl_2$ leads formation of a homoleptic complex, in which both ligands are surface bound c) Absorption of ligand **2** and a phosphonic acid coadsorbant, followed by aqueous $FeCl_2$ and solution of ligand **2**. TiO_2 nanoparticles are light grey, iron(II) centers purple, ligand **2** is yellow, ancillary ligand (here ligand **2**) is orange and coadsorbants are green.*

To avoid formation of the homoleptic complex with two surface-bound anchoring ligands, we introduced coadsorbants in the hope that by diluting the anchoring ligand the same would hold true for the surface occupancy of **2** (Figure 3.15c). [16-18] Three possible coadsorbants, phenylphosphonic acid, *n*-decylphosphonic acid and *tert*-butylphosphonic acid, are shown in Scheme 3.2. Phenylphosphonic acid was considered for its likeness (aromaticity) to the anchoring ligand (Scheme 3.2). *tert*-Butylphosphonic acid and *n*-decylphosphonic acid were of

interest because of their bulkiness and possibly good steric hinderance (Scheme 3). Solution 1 was altered by addition of the coadsorbants in different ratios (Table 2.2).

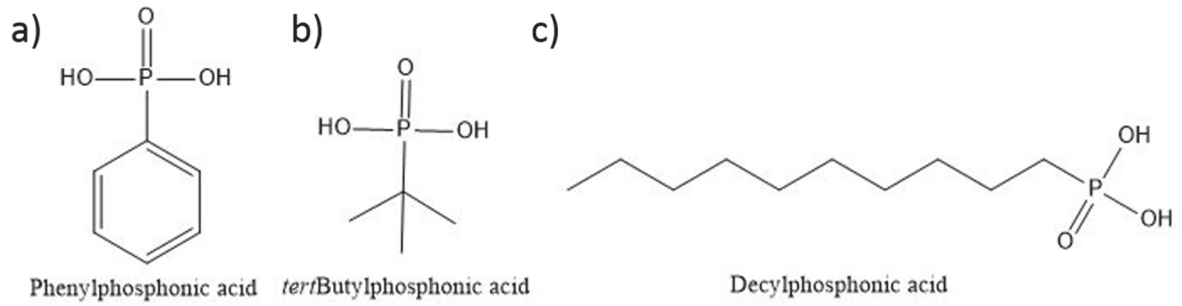

Scheme 3.2. *Structures of coadsorbants: a) Phenylphosphonic acid (Phen), b) tertButylphosphonic acid (tBu), c) Decylphosphonic acid (Decyl)*

At this point, the $[Fe(\mathbf{2})_2]^{2+}$-complex was assembled on the substrate in a three-step process (Figure 3.15c). The first step consisted of treating the surface with a mixture of ligand **2** with different ratios of coadsorbants, as indicated in Table 2.2 (p. 36). When these surfaces were now submerged in aqueous $FeCl_2$, only a pale purple coloration was visible. This indicates that formation of the homoleptic surface-bound complex is reduced compared to the case where there is no coadsorbant. The following treatment with DMSO solution of **2** generated an intense purple colour, that is presumed to be due to the heteroleptic $[(\mathbf{2}_{surface})Fe(\mathbf{2})]^{2+}$ complex with minimal amounts of the homoleptic complex $[Fe(\mathbf{2}_{surface})_2]^{2+}$.

For optimization of the ratio and type of coadsorbant, we monitored the formation of $[Fe(\mathbf{2})_2]^{2+}$ using solid-state UV-vis spectroscopy focusing on the MLCT band at 575 nm (Figure 3.16). Measurements were taken after subsequent treatment of the FTO/TiO_2 surfaces in solution 1 (ligand **2** and coadsorbant), aqueous $FeCl_2$ and then ligand **2**.

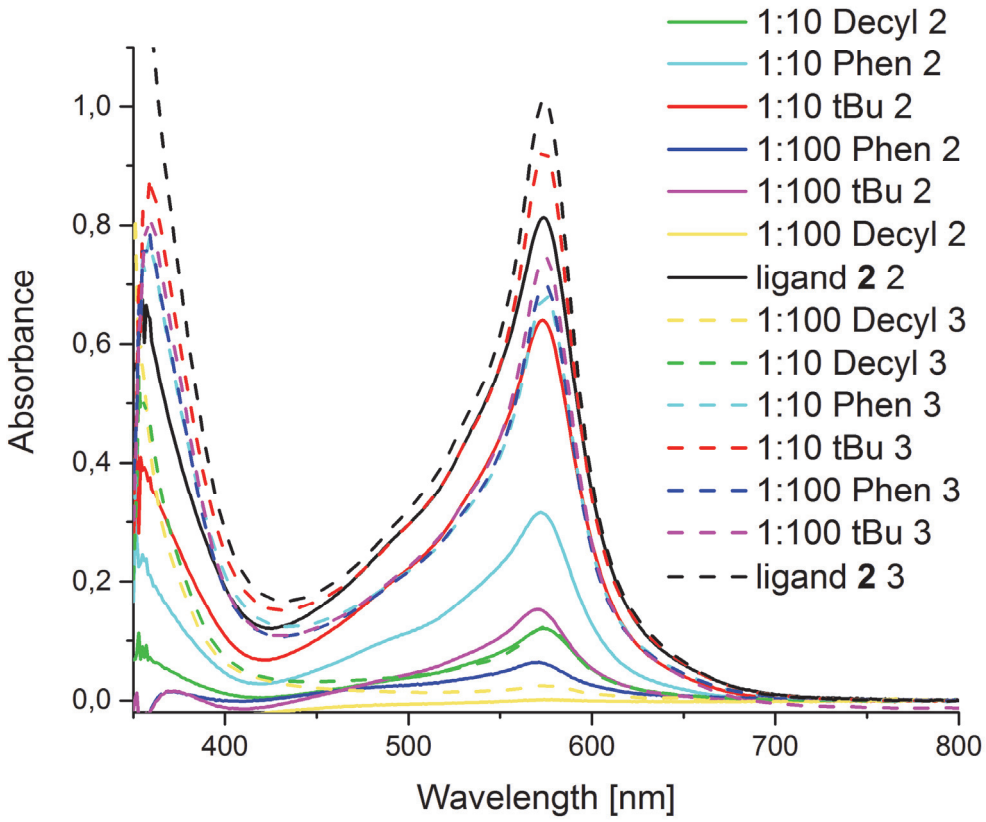

Figure 3.16 *Solid state absorption spectra of the surface bound $[Fe(tpy)_2]^{2+}$ chromophore showing the characteristic MLCT. The spectra were taken after treatment of the surface with anchoring ligand and coadsorbant (not shown), aqueous iron(II) chloride (solid lines) and anchoring ligand (dashed lines). Different colors indicate different coadsorbants or coadsorbant/anchoring ligand ratios. The composition of solutions 2 and 3 are given in Tables 2.1 and 2.2.*

After treatment with $FeCl_2$ (Figure 3.16, solid lines), the spectra suggest minimal formation of the $[Fe(tpy)_2]^{2+}$ chromophore. But the intensity increases significantly (Figure 3.16, dashed lines) after a second treatment with **2**. For better comparison the results are plotted as a column graph in Figure 3.17. In Figure 3.17a) the absorbance at 575 nm is plotted after treatment with solution 2 and after solution 3 for every coadsorbant type and ratio. Figure 3.17b) shows the difference between the two dipping steps. The highest increase can be observed for both, tert-butylphosphonic acid and phenylphosphonic acid as coadsorbants with an optimum concentration of 100 mM and 1 mM ligand 2. This indicates that the highest number of active $[Fe(tpy)]^{2+}$ moieties are generated by addition of tert-butylphosphonic acid or phenylphosphonic acid as coadsorbants. 100 mM tert-butylphosphonic acid and 1 mM ligand **2** were further used as solution 1 for experiments.

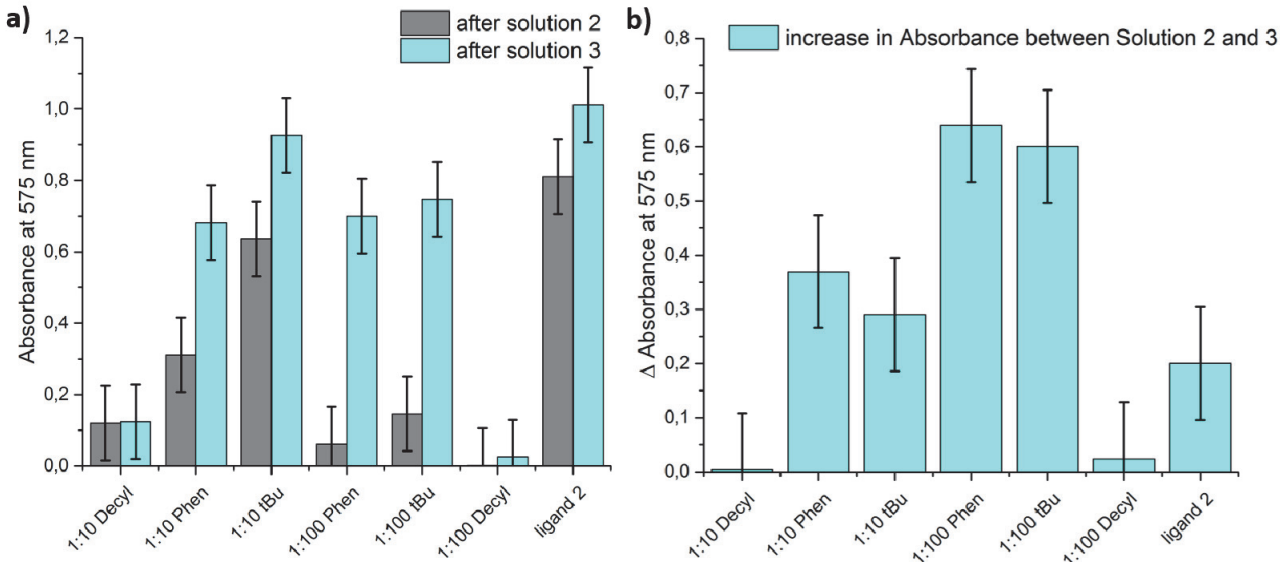

Figure 3.17. *a) Absorption at the typical $[Fe(tpy)_2]^{2+}$ related MLCT (575nm). Values taken from solid state absorption spectra (Figure 3.16a). The spectra were taken after dipping of the FTO/TiO_2 surfaces in anchoring ligand and coadsorbant (not shown), aqueous iron(II) chloride (grey) and anchoring ligand (blue). Ratio of anchoring ligand to coadsorbant is given in the label (see Table 2.1 and table 2.2). b) Differences between absorption values (grey and blue) shown in* ***a)****, which represent the increase in absorption between dipping in Solution 2 and 3.*

Detailed investigation into the assembly process

After adaptation and optimization of the SALSAC approach for $[Fe(tpy)_2]^{2+}$ complexes, further experiments were conducted to gain insight into the binding hierarchy of the (4-([2,2':6',2''-terpyridin]-4'-yl)phenyl)phosphonic acid (ligand **2**) anchoring ligand in comparison to the *tert*-butylphosphonic acid coadsorbant. Phosphonic acid anchoring groups are known to be a good anchoring group, [19, 20] especially in aqueous systems. Phosphonic acid anchoring groups have been shown to bind more strongly to metal oxide surfaces compared to carboxylic acid anchoring groups. [21-24] The carboxylic acid anchoring group, one that is commonly used to adsorb dyes to titania surfaces, can be desorbed in the presence of water, thus making a poor anchoring group in aqueous systems. [25-28] The aim of the studies described in this chapter was to investigate if the anchoring ligand was able to displace the coadsorbant from the surface. This is of special interest when ligand **2** is used as an ancillary ligand. Therefore, ligand **2** was tested for its ability to displace *tert-b*utylphosphonic acid. Ligand **2** was also compared

to 4'-phenyl-2,2':6',2''-terpyridine (ligand **4**), that bears no anchoring group, as ancillary ligand. Also, another interesting solvent effect was observed: the ability of DMSO to take out iron from the surface-bound $[Fe(tpy)]^{2+}$ moiety.

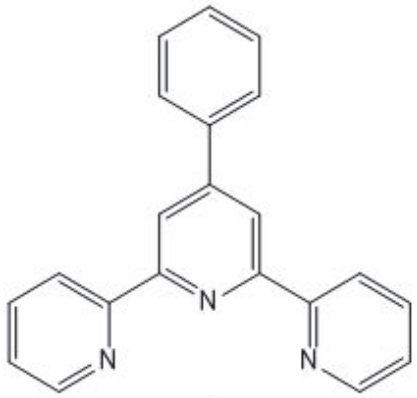

4

Scheme 3.3. *Structures of* 4'-phenyl-2,2':6',2''-terpyridine *(ligand **4**).*

Although carboxylic anchoring groups are well established for surface-functionalization, they are known to be desorbed from TiO_2 in water. [25-28] Therefore, for the optimization of the SALSAC method for iron complexes with terpyridine ligands compound **2**, bearing a phosphonic acid anchoring group, was used as an anchoring ligand.

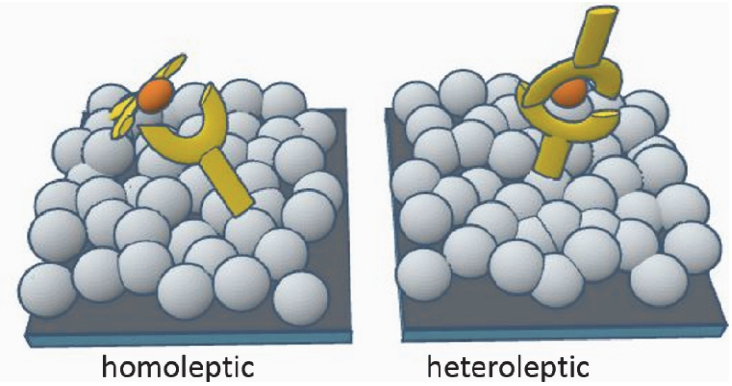

Figure 3.18. *Schematic representation of the heteroleptic $[(\mathbf{2}_{surface})Fe(\mathbf{2})]^{2+}$ and the homoleptic $[Fe(\mathbf{2}_{surface})_2]^{2+}$ complex.*

In our setup, compound **2**, bearing a phosphonic acid anchoring group, was used as an anchoring ligand and a capping ligand. So next, we wanted to verify, that in this setup indeed compound **2** can act as a capping ligand, forming the heteroleptic $[(\mathbf{2}_{surface})Fe(\mathbf{2})]^{2+}$ and not the

homoleptic $[Fe(\mathbf{2}_{surface})_2]^{2+}$ complex (Figure 3.18). Therefore ligand **2** as an ancillary ligand is compared to ligand **4** (Scheme 3.3), which bears no anchoring group.

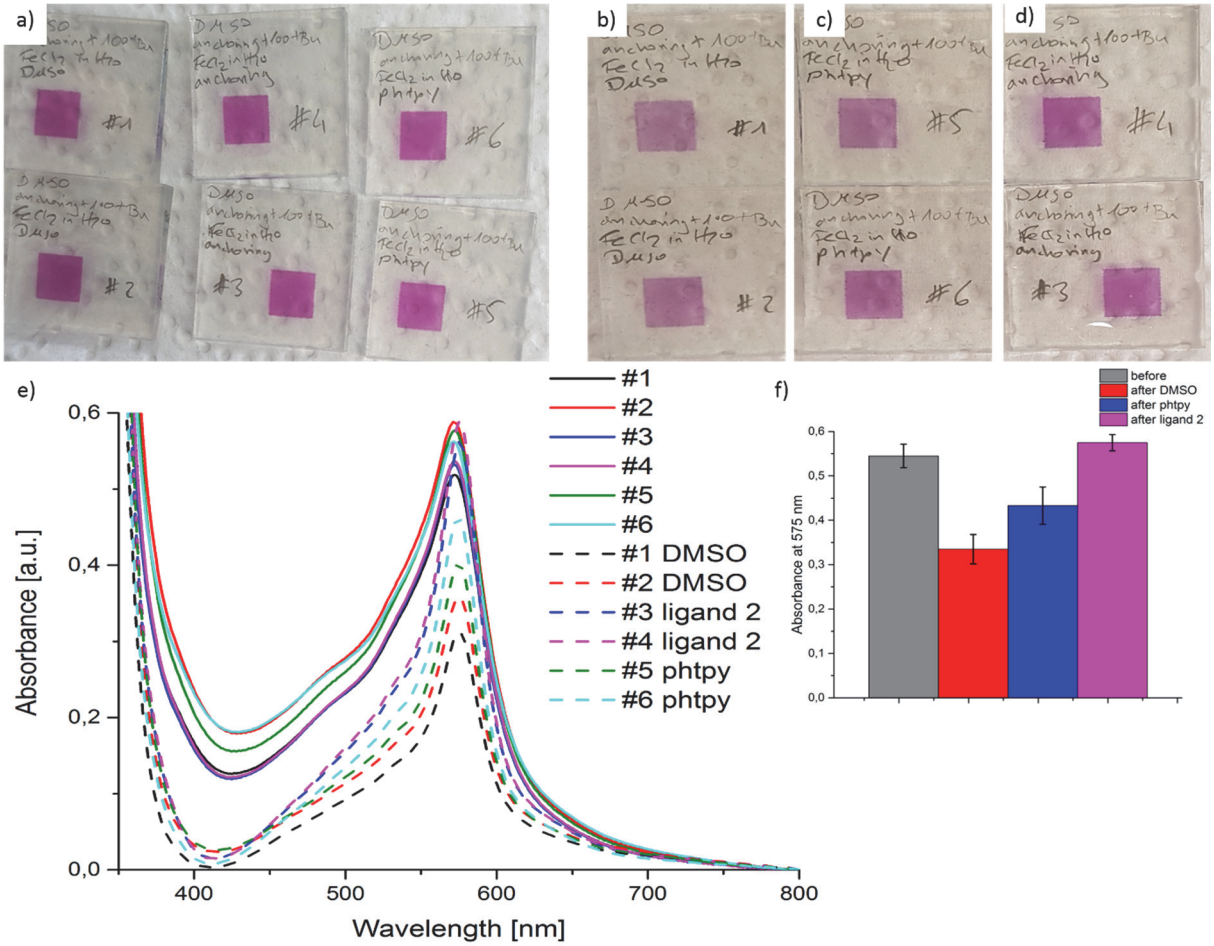

Figure 3.19. *a) Surfaces after pre-treatment with DMSO, followed by anchoring ligand and coadsorbant and then aqueous iron(II) chloride b) Surfaces after pre-treatment with DMSO, followed by anchoring ligand and coadsorbant, aqueous iron(II) chloride, then DMSO c) Surfaces after pre-treatment with DMSO, followed by anchoring ligand and coadsorbant, aqueous iron(II) chloride, then phtpy in DMSO d) Surfaces after pre-treatment with DMSO, followed by anchoring ligand and coadsorbant, aqueous iron(II) chloride, then* ***2*** *in DMSO e) Solid state absorption spectra of a) (solid lines), b) (dashed lines, black and red), c) (dashed lines, green and light blue) and d) (dashed lines, blue and pink) f) Absorption values (from e) at 575 nm before (grey) and after final treatment with pure DMSO (red), phtpy (blue) or ligand 2 (pink)*

The surfaces were pre-treated with DMSO for later comparison against pre-treatment with *tert-*butylphosphonic acid (coadsorbant). Following the pre-treatment, the surfaces were consecutively submerged in anchoring ligand and coadsorbant and then aqueous iron(II)

chloride (Figure 3.19a). To test ligand **2** against ligand **4**, a pair of surfaces was immersed in a solution of ligand **4** in DMSO (Figure 3.19c), a solution of ligand **2** (Figure 3.19d) or the DMSO control (Figure 3.19b). Comparing the surfaces before and after the last treatment, they appear paler in colour.

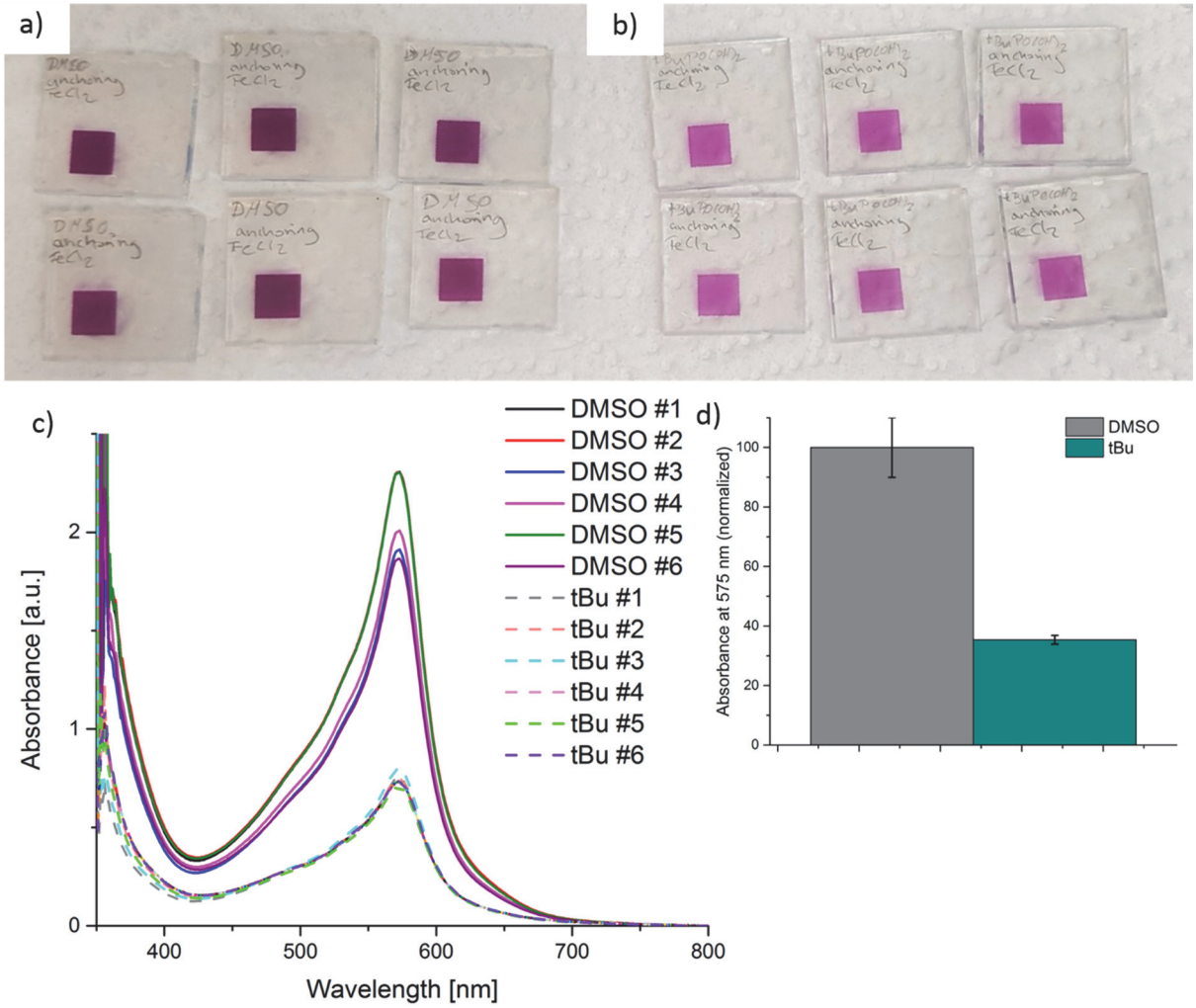

Figure 3.20. *a) Surfaces after pre-treatment with DMSO, followed by anchoring ligand and then aqueous iron(II) chloride b) Surfaces after pre-treatment with coadsorbant in DMSO, followed by anchoring ligand and aqueous iron(II) chloride c) Solid state absorption spectra of the surface bound* $[Fe(tpy)_2]^{2+}$ *chromophore showing the characteristic MLCT. The spectra were taken after pre-treatment of the surface with DMSO, followed by anchoring ligand and aqueous iron(II) chloride (solid lines) or pre-treatment with coadsorbant in DMSO, followed anchoring ligand and aqueous iron(II) chloride (dashed lines). Different colors indicate different FTO/*TiO_2 *surfaces. d) Differences between absorption values of surfaces pre-treated with DMSO (grey) vs. surfaces pre-treated with coadsorbant in DMSO (blue).*

This is confirmed in the solid-state UV-vis spectra, which were recorded before and after the final treatment (Figure 3.19e). The absorbance values at 575 nm are directly compared in Figure 3.19f. The absorbance after treatment with DMSO (red) and **4** (blue) is significantly decreased compared to before (grey). This indicates that the DMSO has some undesired effect. This will be discussed later in this chapter. However, the increased absorbance after treatment with **4** compared to treatment with pure DMSO shows the formation of heteroleptic $[Fe(\mathbf{2}_{surface})\mathbf{4}]^{2+}$ complex, confirming the presence of active $[Fe(tpy)]^{2+}$ moieties before the treatment. The even higher increase of absorbance after treatment with **2**, compared to final treatment with **4**, indicates that ligand **2** does interact with the surface, possibly displacing coadsorbant.

To verify this proposal, a set of FTO/TiO_2 surfaces was pre-treated with coadsorbant in DMSO, whereas the control was treated with DMSO only. Both sets of FTO/TiO_2 surfaces were then consecutively exposed to ligand **2**, followed by aqueous iron(II) chloride. The FTO/TiO_2 surfaces that were pre-treated with DMSO show deep purple coloration after treatment with $FeCl_2$ (Figure 3.20a), revealing the formation of surface-bound $[Fe(\mathbf{2}_{surface})_2]^{2+}$ complex. The FTO/TiO_2 surfaces that were pre-treated with coadsorbant show a paler purple coloration after treatment with $FeCl_2$ (Figure 3.20a). This observation is confirmed by solid-state UV-vis absorption spectra (Figure 3.20c). The pale purple coloration points towards the formation of a smaller amount of surface-bound $[Fe(\mathbf{2}_{surface})_2]^{2+}$ complex. This can mean one of two things: It can show that ligand **2** is in fact able to displace some, but not all coadsorbant. Another possible explanation is that the coadsorbant surface coverage is incomplete and that ligand **2** fills up the “holes” without displacement of coadsorbant.

Both sets of FTO/TiO_2 surfaces were further treated with capping ligand, **2** (Figure 3.21c) or **4** (Figure 3.21b), or DMSO (Figure 3.21a). The set, which was pre-treated with DMSO, shows no apparent difference in coloration after the last treatment when comparing the two ancillary ligands and DMSO. This can be explained by the lack of coadsorbant in this set. The homoleptic surface-bound $[Fe(\mathbf{2}_{surface})_2]^{2+}$ complex is formed upon treatment with $FeCl_2$ and no active $[Fe(tpy)]^{2+}$ moieties remain for binding of ligand **2** or **4**. However, both sets of FTO/TiO_2 surfaces show paler purple coloration, that is confirmed by the solid-state UV-vis spectra, after the last treatment compared to before, hinting at an effect caused by the DMSO.

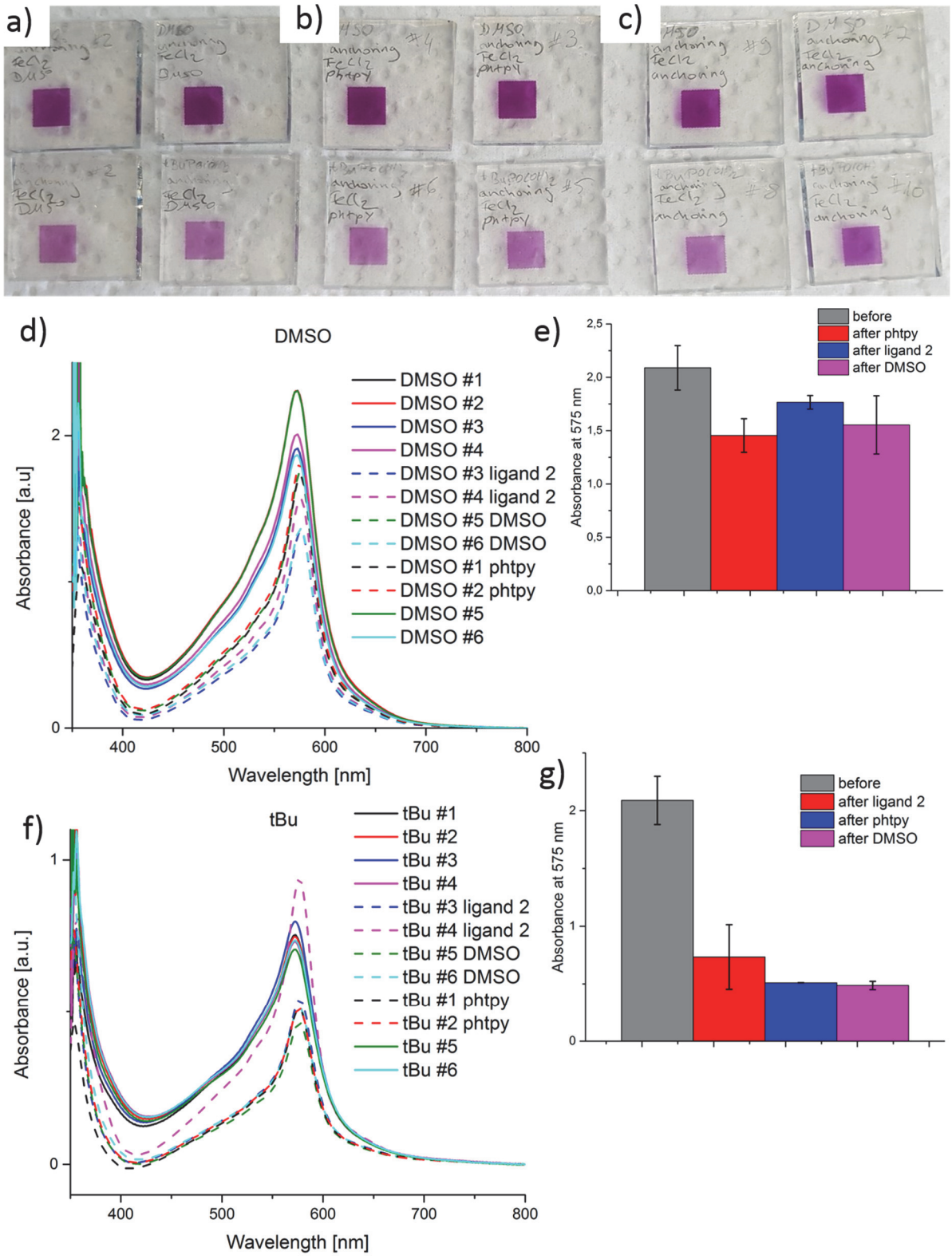

Figure 3.21. *Pictures a), b) and c) show surfaces from figure 3.20a) (top) and figure 3.20b)(bottom) after final treatment with DMSO (a),* ***4*** *(phtpy ,b) and ligand* ***2*** *(c). d) Solid state absorption spectra of the surface bound* $[Fe(tpy)_2]^{2+}$ *chromophore showing the characteristic MLCT. The spectra were taken after pre-treatment of the surface with DMSO, followed by anchoring ligand and aqueous iron(II) chloride (solid lines) and after further treatment with pure DMSO,* ***4*** *or ligand* ***2*** *(dashed lines) e)*

Absorption values taken from d) at 575 nm before (grey) and after final treatment; after further treatment with pure DMSO(pink), ***4*** *(phtpy, blue) or ligand 2 (red) f) Solid state absorption spectra of the surface bound* $[Fe(tpy)_2]^{2+}$ *chromophore showing the characteristic MLCT. The spectra were taken after pre-treatment of the surface with coadsorbant in DMSO, followed by anchoring ligand and aqueous iron(II) chloride (solid lines) and after further treatment with pure DMSO,* ***4*** *(phtpy) or ligand 2 (dashed lines) g) Absorption values taken from f) at 575 nm before (grey) and after final treatment; after further treatment with pure DMSO(pink),* ***4*** *(blue) or ligand 2 (red)*

Decoloration of the surface is evidence of a decrease of $[Fe(tpy)_2]^{2+}$ complex on the surface. This could be caused by either desorption of the complex from the surface or by decomplexation through loss of the iron center. To confirm the possible loss of the iron center both sets of cells were resubmerged in aqueous $FeCl_2$. Solid-state UV-vis spectra were recorded after dipping in aqueous $FeCl_2$, after treatment with capping ligands or DMSO and after re-treatment with aqueous $FeCl_2$ (Figure 3.22). Absorption values after final treatment with iron (II) chloride match the values before contact with DMSO, in the case of ligand 2 even exceeding the original values. This proves that $[Fe(tpy)_2]^{2+}$ can be regenerated and that DMSO is able to some extent to remove iron(II) from the complex.

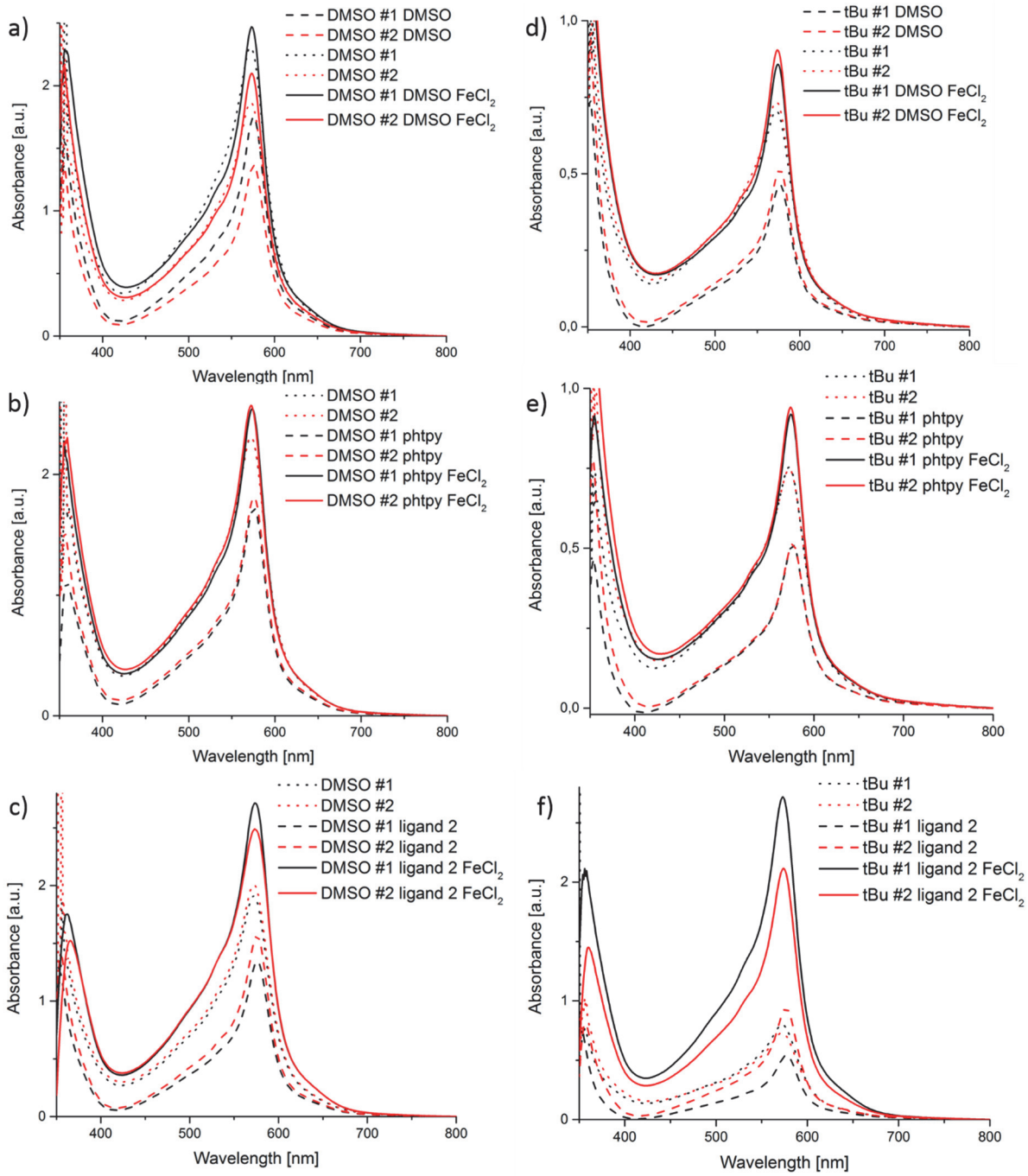

Figure 3.22. *Solid state absorption spectra of the surface bound $[Fe(tpy)_2]^{2+}$ showing the characteristic MLCT. The left hand side spectra were taken after pre-treatment of the surface with DMSO, followed by anchoring ligand, aqueous iron(II) chloride (dotted line) and DMSO (picture a, dashed line)/**4** (phtpy) (picture b, dashed line)/ligand 2 (picture c, dashed line) and finally retreated with iron(II) chloride (solid line); The right hand side spectra were taken after pre-treatment of the surface with coadsorbant in DMSO, followed by anchoring ligand, aqueous iron(II) chloride (dotted line) and DMSO (picture a, dashed line)/ **4** (phtpy) (picture b, dashed line)/ligand 2 (picture c, dashed line) and finally retreated with iron(II) chloride (solid line)*

Optimization of buffer system with regard to the $[Fe(tpy)_2]^{2+}$-complex for later polymersome attachment

In this project the $[Fe(tpy)_2]^{2+}$-complex is investigated as a linker to bind polymer vesicles to a titania surface. The previous experiments showed a strong solvent influence on the formation and stability of the complex on the surface. Polymersomes are usually formed in pH-controlled buffer conditions by self-assembly processes. A typical buffer solution is phosphate buffered saline (PBS, pH 7.4), that is possibly able to anchor to the titania surface.

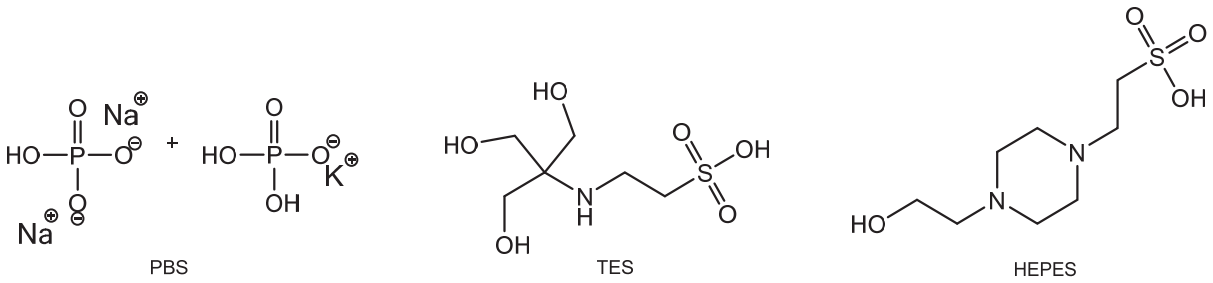

Scheme 3.4. *Structures of phosphate buffered saline (PBS), 2-(4-(2-hydroxyethyl)piperazidin-1-yl)ethane-sulfonic acid (HEPES) and N-[tris(hydroxymethyl)methyl]-2-aminoethanesulfonic acid (TES).*

Therefore, PBS and some other buffers which are generally used for polymer vesicle formation, were investigated for their effect on the surface-bound $[Fe(tpy)_2]^{2+}$-complex. Phosphate buffered saline (PBS), an aqueous solution of 20 mM 2-(4-(2-hydroxyethyl)piperazidin-1-yl)ethane-sulfonic acid (HEPES) and 50 mM NaCl (further referred to as HEPES buffer) and N-[tris(hydroxymethyl)methyl]-2-aminoethanesulfonic acid (TES), whose structures are presented in scheme 3.4), were tested against water and saline (50 mM aqueous NaCl). Commercial TiO_2 FTO/TiO_2 surfaces were functionalized with homoleptic surface-bound $[Fe(\mathbf{2}_{surface})_2]^{2+}$-complex as described before. These FTO/TiO_2 surfaces were immersed in HEPES, TES, PBS, water or saline for three days. Figure 3.23b shows the surfaces after exposure to the buffers. The surfaces show that for treatment of the purple SALSAC-modified FTO/TiO_2 surfaces with HEPES, TES, water and saline leaves the purple coloration intact, whereas treatment with PBS resulted in decolorization. Solid-state UV-vis spectra were recorded before and after exposure to the buffer solutions to quantify the decolorization (Figure 3.23a). Figure 3.23c shows the absorbance at 575 nm for each surface before (grey) and after contact with the buffer solution (green). Figure 3.23d shows the decrease in absorbance between the two values. The measurements show a small decrease in absorbance after treatment with HEPES, TES, water and saline and a large decrease after PBS treatment

(Figure 3.23a). In addition, a strong purple coloration of the PBS solution was observed. This indicates the complex being intact and desorbed from the surface as a whole by the PBS. PBS buffer should therefore be avoided.

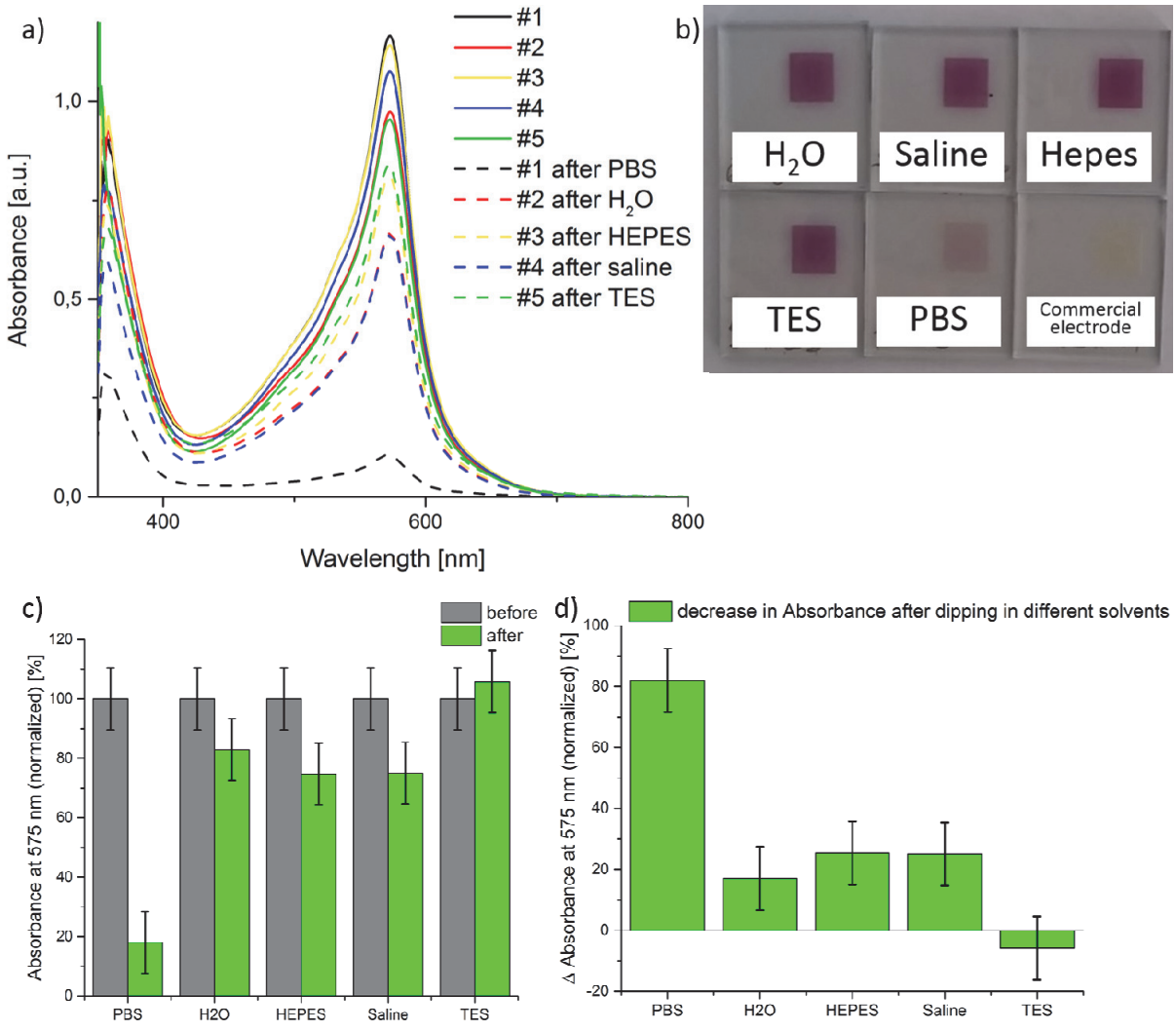

Figure 3.23. *a) Solid-state absorption spectra of [Fe(**2**)$_2$]$^{2+}$-complex on the surface before (solid lines) and after (dashed lines) treatment different aqueous buffers; b) FTO/TiO$_2$ surfaces after exposure to the buffers. c) Relative absorption at the characteristic MLCT (575nm) associated with the [Fe(tpy)$_2$]$^{2+}$ chromophore determined from a) at 575 nm before (grey, normalized to 100%) and after (green) submerging into water and different aqueous buffers; d) Differences between pairs of absorption values (grey and green) shown in c) which represents the decrease in absorbance due to the desorbed [Fe(**2**)$_2$]$^{2+}$.*

$[Fe(tpy)_2]^{2+}$complex anchoring to optimized surfaces

After the preparation of smoothed glass supported titania surfaces together with the successful binding of the linker $[Fe(tpy)_2]^{2+}$ complex to "rough" surfaces, the next step was to investigate the complex-binding to "smooth" surfaces. This step is of high interest, because these surface anchored linkers should serve as binding positions to achieve the immobilization of nanometer-sized polymersomes.

Starting from commercial FTO-covered glass, the surface roughness was decreased by spin-coating multiple titania layers onto the FTO. The highest smoothness was achieved with seven compact layers of spin coated TiO_2. To make sure that the spin coated titania layers do not alter the desired ability of the surface to bind anchoring ligands and therefore $\{Fe(tpy)_2\}^{2+}$-core, the complex has to be assembled on the smooth surfaces. To verify whether the smoothed surface is capable of binding the desired surface anchors, the homoleptic surface bound $[Fe(\mathbf{2}_{surface})_2]^{2+}$-complex was assembled on the substrate in the three-step process previously detailed. First, the surface is treated with a solution of **2**, followed by aqueous $FeCl_2$ and ligand **2** again. As a result of the decreased surface area caused by reduction of the surface roughness, less complex can be present on the surface and solid-state UV-vis spectroscopy is not sensitive enough to quantify the amount of surface-bound $[Fe(tpy)_2]^{2+}$ species. Therefore, we used cyclic voltammetry (Figure 3.24) to monitor the reversible Fe^{II}/Fe^{III} redox couple of the surface-bound $[Fe(tpy)_2]^{2+}$ species. [29] The measurements were made using the modified FTO/TiO_2 surface which served as the working electrode in a three-electrode system with platinum wire as counter electrode, silver wire as pseudo-reference electrode and 0.1 M potassium nitrate as electrolyte. The measurements were not directly referenced and later corrected to the same potential as that in $[Fe(tpy)_2][PF_6]_2$ (+0.77 V). [29] No redox process was observed when the working electrode was connected with the non-conductive glass side facing towards the counter electrode, indicating that the iron complex is bound to the TiO_2 side and not to the glass back side. A comparison of cyclic voltammograms for the commercial FTO/TiO_2 surface and for surfaces with different numbers of compact layers clearly shows the decrease in current associated with lower surface coverage of the redox-active species (Figure 3.24).

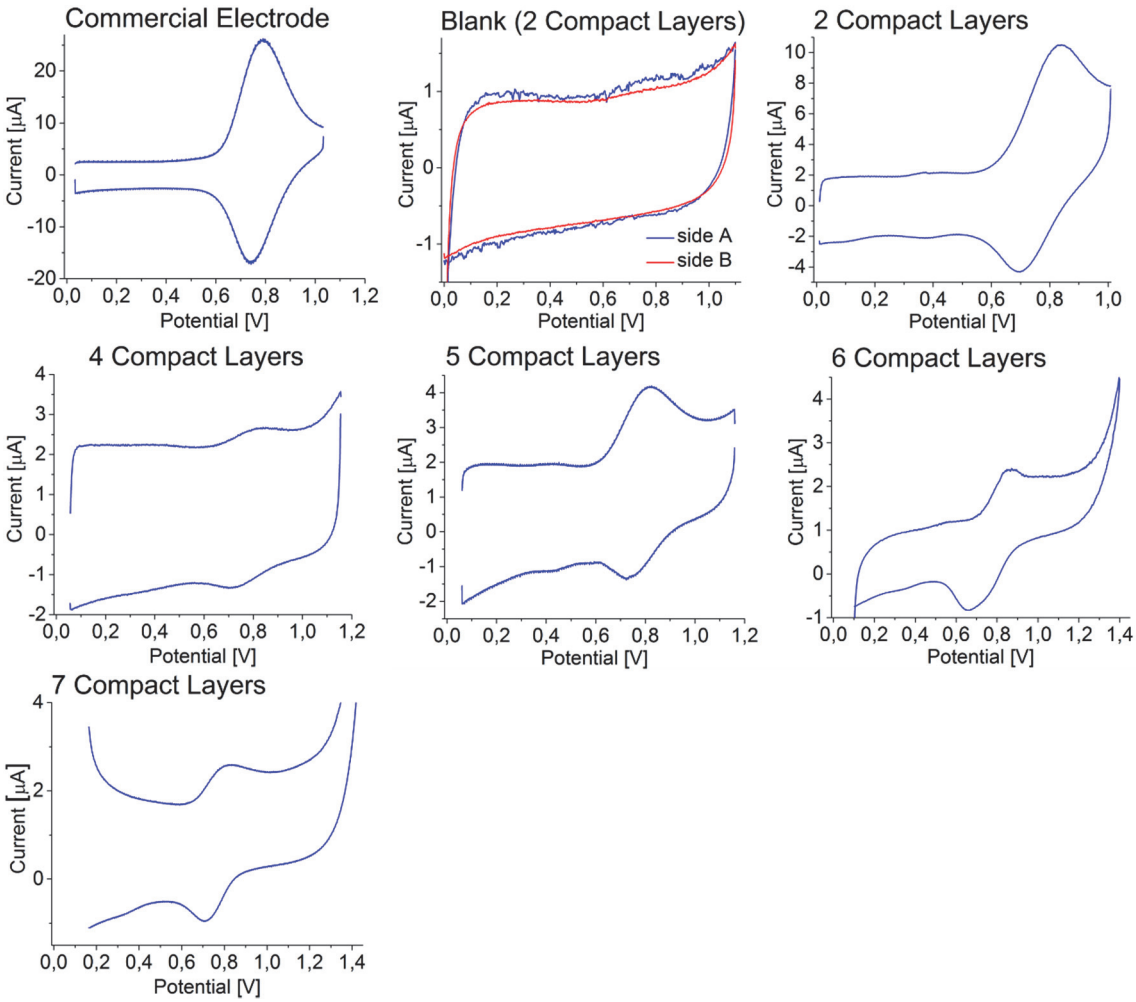

Figure 3.24. *Cyclic voltammograms of surface-bound $[Fe(\mathbf{2})_2]^{2+}$. The surfaces bear different numbers of titania layers. The setup is a three-electrode system, consisting of a glass supported FTO-TiO_2 working electrode with surface bound $[Fe(tpy)_2]^{2+}$, a platinum wire counter electrode and a silver wire pseudo-reference electrode. 0.1 M potassium nitrate is used as electrolyte. Spectra were recorded within a potential window of circa 1.2 V. Scan rates varied between 0.03 and 0.1 V s^{-1}. Measurements are not directly referenced and are normalized to the same potential than that in $[Fe(tpy)_2][PF_6]_2$ (+0.77 V).* [29]

Conclusion

In this chapter we discussed the SALSAC approach (´Surface-as-ligand, surface-as-complex´) for the stepwise assembly of complexes on a semiconductor (titania) surface; the strategy was then optimized for the iron terpyridine complex case, while it was originally developed for stepwise assembly of various copper(I) complexes on titania surfaces. We found that some solvents, like EtOH, MeCN and ethoxyethanol, were able to stabilize a surface bound iron(II) terpyridine complex, which allows for a straightforward stepwise assembly of the $[Fe(tpy)_2]^{2+}$-complex. However, solvents like water and MeOH did not show this stabilizing effect and the

use of coadsorbants had to be introduced. These coadsorbants reduce the amount of the anchoring ligand, spreading it out on the surface, thus minimizing the formation of homoleptic surface-bound $[Fe(\mathbf{2}_{surface})_2]^{2+}$. *tert*-Butylphosphonic acid and phenylphosphonic acid work equally well as coadsorbants in a coadsorbant to anchoring ligand ratio of 100:1. With the use of an appropriate solvent or the addition of coadsorbants, the formation of the heteroleptic $[(\mathbf{2}_{surface})Fe(\mathbf{2})]^{2+}$ complex could be achieved via the SALSAC approach. We found that the anchoring ligand can, to a small amount, displace coadsorbant. Furthermore the ability of ligand **2** to displace coadsorbant was tested by covering the surface with coadsorbant before treatment with **2** and by comparison against a terpyridine ligand without anchoring group as ancillary ligand. We found that, even after coverage of the surface with coadsorbant, ligand **2** can still adsorb. This is either by displacement of coadsorbant or by filling up "holes" in the surface coverage. This effect does not interfere with our purposes, though. We were able to show by use of ligand **4**, that with the use of coadsorbants $[Fe(tpy)]^{2+}$ moieties remain active for binding with non-anchoring terpyridines. It is also worth noting, that special attention should be paid to the use of DMSO as a solvent for ancillary ligands in the stepwise assembly of iron complexes. DMSO was shown to, some extend, to take iron out of the complex. For our purposes this is not a problem. Since we aim to use the complex for immobilizing polymersomes on a surface, DMSO will not be necessary after $FeCl_2$. The final surface treatment will be with aqueous solutions. Therefore various aqueous buffers were tested for their influence on the system. We can show, that the phosphate buffered saline (PBS) is very effective at desorbing the $[Fe(tpy)_2]^{2+}$-complex off the surface and should therefore be avoided. Water, saline, TES and HEPES give less decolorization and are considered acceptable for this system. Lastly, the smoothed surfaces, that were optimized by layer-by-layer deposition of spin-coated titania, were tested to confirm that the spin coated titania layers did not change the desired ability of the surface to bind anchoring ligands and therefore $[Fe(tpy)_2]^{2+}$. Cyclic voltammetry measurements confirmed the presence of the complex on the spin-coated titania surface.

References

[1] E. Schönhofer, B. Bozic-Weber, C. J. Martin, E. C. Constable, C. E. Housecroft, J. A. Zampese, *Dyes Pigm.,* 2015, **115**, 154.

[2] F. J. Malzner, C. E. Housecroft, E. C. Constable, *Inorganics*, 2018, **6**, 57.

[3] E. C. Constable, *Adv. Inorg. Chem.,* 2018, **71**, 79.

[4] H. A. Redondo, E. C. Constable, C. E. Housecroft, *Chimia*, 2009, **63**, 205.

[5] E. C. Constable, W. Meier, C. Nardin, S. Mundwiler, *Chem. Commun.*, 1999, 1483.

[6] F. Krohnke, *Synthesis,* 1976, 1.

[7] V. Spampinato, N. Tuccitto, S. Quici, V. Calabrese, G. Marletta, A. Torrisi, A. Licciardello, *Langmuir*, 2010, **26**, 8400.

[8] F. J. Malzner, S. Y.Brauchli, E. Schönhofer, E. C. Constable, C. E. Housecroft, *Polyhedron*, 2014, **82**, 116.

[9] G. D. Storrier, S. B. Colbran, D. C. Craig, *J. Chem. Soc., Dalton Trans.*, 1997, 3011.

[10] E. C. Constable, J. Lewis, M. C. Liptrot, P. R. Raithby, *Inorg. Chim. Acta,* 1990, **I78**, 47.

[11] E. C. Constable, E. L. Dunphy, C. E. Housecroft, M. Neuburger, S. Schaffner, F. Schaper, S. R. Batten, *Dalton Trans.,* 2007, 4323.

[12] J. M. Rao, D. J. Macero, M. C. Hughes, *Inorg. Chim. Acta,* 1980, **41**, 221.

[13] K. Harewood, J. S. Wolff, *Anal. Biochem.*, 1973, **55**, 573.

[14] J.Penfold, E. Staples, I. Tucker, R. K. Thomas, *Langmuir*, 2002, **18**, 5755.

[15] T. P. Dumont (2006). *Laser interaction with materials: From transparent materials to thin films* (Doctoral dissertation). Available from ETH Library. (DISS. ETHNO. 16620). DOI: 10.3929/ethz-a-005209645

[16] C.-l. Jung, J. Lim, J.-H. Park, K.-H. Kim, C.-H. Han, Y. Jun, *RSC Adv.,* 2013, **3**, 20488.

[17] H. Shen, H. Lin, Y. Liu, X. Li, J. Zhang, N. Wang, J. Li, *Electrochim. Acta,* 2011, **56**, 2092.

[18] N. R. Neale, N. Kopidakis, J. van de Lagemaat, M. Grätzel, A. J. Frank, *J. Phys. Chem. B.,* 2005, **109**, 23183.

[19] B. J. Brennan, M. J. L. Portoles, P. A. Liddell, T. A. Moore, A. L. Moore, D. Gust, *Phys. Chem. Chem. Phys.,* 2013, **15**, 16605.

[20] D. G. Brown, P.A. Schauer, J. Borau-Garcia, B. R. Fancy, C. P. Berlinguette, *J. Am. Chem. Soc.,* 2013, **135**, 1692.

[21] M. Nilsing, S. Lunell, P. Persson, L. Ojamae, *Surface Sci.,* 2005, **582**, 49.

[22] M. Nilsing, P. Persson, L. Ojamae, *Chem. Phys. Lett.,* 2005, **415**, 375.

[23] R. Luschtinetz, J. Frenzel, T. Milek, G. Seifert, *J. Phys. Chem. C,* 2009, **113**, 5730.

[24] R. Luschtinetz, S. Gemming, G. Seifert, *Eur. Phys. J. Plus,* 2011, 126.

[25] Y. Ooyama, T. Sato, Y. Harima, J. Ohshita, *J. Mater. Chem. A,* 2014, **2**, 3293.

[26] P. Giannopoulos, A. Nikolakopoulou, A. K. Andreopoulou, L. Sygellou, J. K. Kallitsis, P. Lianos, *J. Mater. Chem. A,* 2014, **2**, 20748.

[27] L. Wang, X. Yang, X. Wang, L. Sun, *Dyes Pigm.,* 2015, **113**, 581.

[28] L. Zhang, J. M. Cole, *ACS Appl. Mater. interfaces,* 2015, **7**, 3427.

[29] H. S. Chow, E. C. Constable, C. E. Housecroft, M. Neuburger, S. Schaffner, *Dalton Trans.* 2006, **23**, 2881.

Chapter 4

The Polymer Nanocontainers - Preparation of tpy-functionalized polymersomes

Abstract

The focus of this chapter is on the production of nanoscale-sized vesicles made out of a triblock copolymer based on PMOXA-PDMS-PMOXA ($A_6B_{44}A_6$) which was modified with an aldehyde group to allow their immobilization of the solid surface via a linker. The terminal hydroxyl groups of the bifunctional amphiphilic triblock copolymer $A_6B_{44}A_6$ were oxidized using DMP to aldehydes in $A_6B_{44}A_6$-CHO, with an aldehyde content of 0.5%. Polymersomes were assembled using the film rehydration method from modified and unmodified copolymer. A combination of TEM, SLS/DLS and FCS provided evidence for radii in the range of 50 – 100 nm. Polymersomes were modified by Schiff base condensation of the primary amino group of a tpy ligand to the aldehyde end group of the polymersomes.

Motivation and Problem Definition

The field of nanotechnology is rapidly expanding and polymeric nanocompartments play a significant role due to their usage in a vast variety of applications, like drug delivery systems, as models for artificial cells, for sensing purposes, or even in food packaging. [1] Reasons for this are on one hand their increased mechanical stability compared with lipid vesicles (liposomes) and on the other hand that they exhibit biocompatibility and reduced toxicity depending on the type of polymer used. [2] Further, there is the possibility to achieve membrane permeability by various methods. The polymer membranes can be chemically modified to enable responsiveness to various stimuli such as pH, light and temperature, which can be used to release cargo under specific conditions. [3-5] Alternatively appropriate polymers, which form a porous membrane, can be selected and no external stimulus is needed. Another option to obtain membrane permeability is if the hydrophobic part of the di- and triblock copolymers is flexible enough as, for example, in the case of PDMS. In this case, ion-channels, transporters, pore-forming peptides and membrane proteins can be inserted with full functionality into these polymer membranes, which are up to 5 times thicker than the lipid counterparts. [6] Membrane permeabilization together with the possibility of encapsulating enzymes inside the cavities of these polymersomes allows the creation of nanoreactors, where substrates and products can pass through the membrane via biopores and the enzyme reaction can take place inside the confined spaces of the polymersomes. [7]

By immobilizing polymer nanocompartments or even nanoreactors on surfaces, the functionality of the surface can be greatly increased. Towards our aim of surface-immobilized polymersomes, in this chapter we discuss the formation, characterization and functionalization of the polymer nanocompartments based on PMOXA-PDMS-PMOXA. Our functionalization route of choice to achieve tpy-functionalized polymersomes with the ability to anchor to our previously modified surfaces, was a three step strategy shown in Figure 4.1. We started from the triblock copolymer (Figure 4.1a), which we equipped with a responsive functionality (Figure 4.1b). In the next step, polymersomes were prepared from this copolymer (Figure 4.1c). Lastly, these polymersomes were equipped with a tpy moiety (Figure 1d) through a condensation reaction.

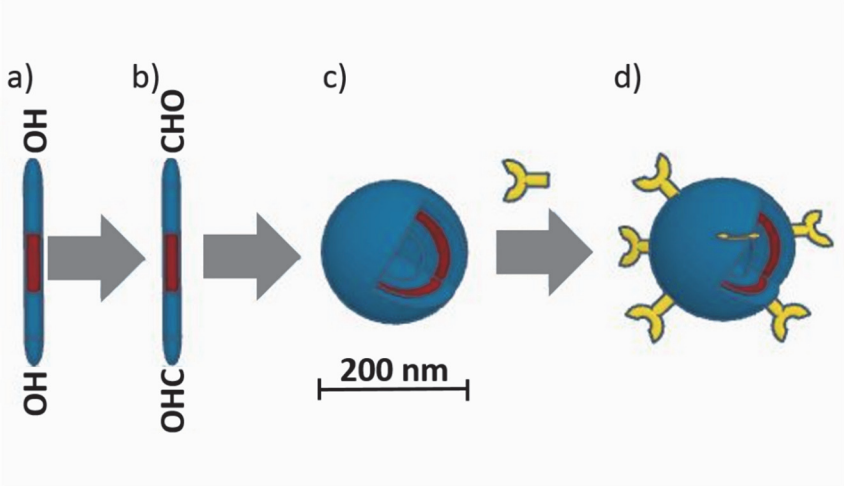

Figure 4.1. *Schematic illustration of the functionalization route. A hydroxy terminated bifunctional amphiphilic block copolymer (a) can be functionalized with a reactive aldehyde group by oxidation (b) and self-assembled into spherical nanostructures (c). These nanostructures can be equipped with a tpy functionality (d).*

Polymer synthesis and modification

In order to produce polymersomes to anchor to the surface, an amphiphilic block copolymer was synthesized. The hydroxyl end groups of the copolymer needed to be oxidized in order to later, after polymersome assembly, bind terpyridine ligands. This part of the work was done in collaboration with Dr. Adrian Dinu.

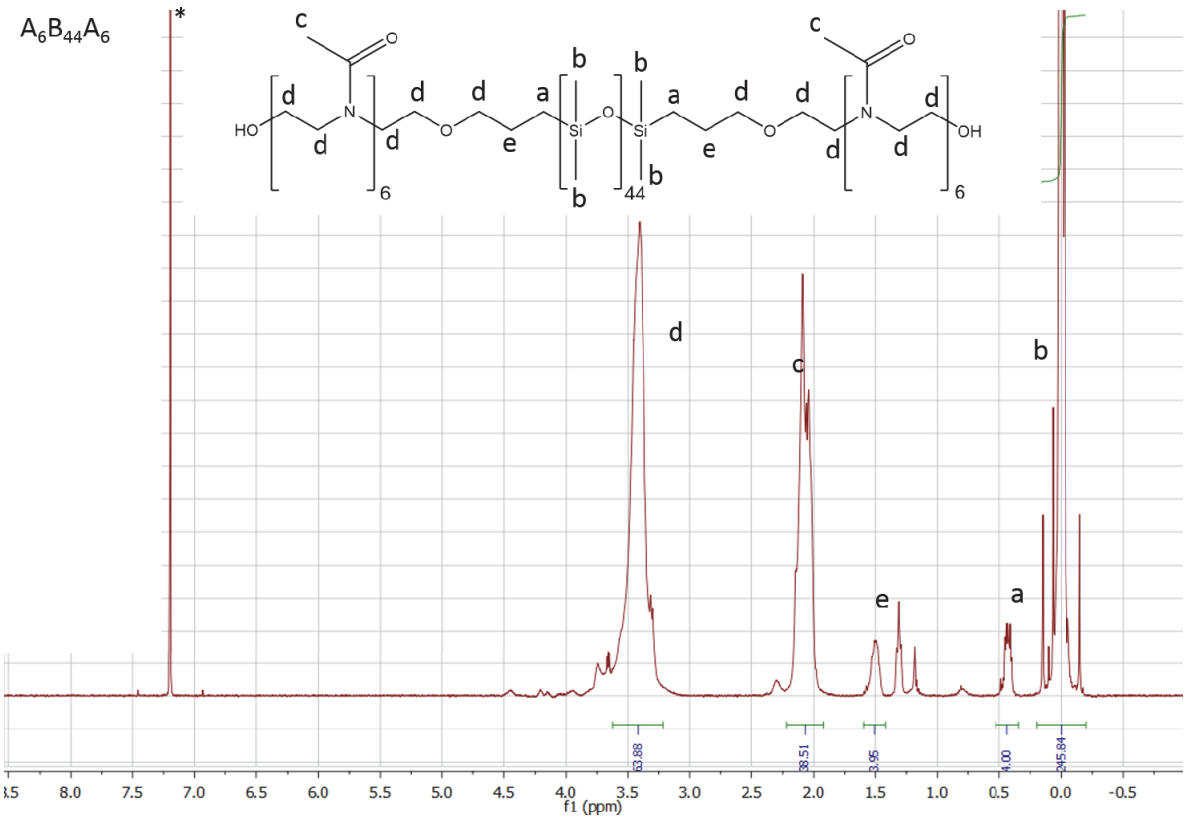

Figure 4.2. *400 MHz ^{1}H-NMR spectrum of poly(2-methyloxazoline - poly(dimethylsiloxane - poly(2-methyloxazoline) ($A_6B_{44}A_6$) in $CDCl_3$ (*)*

Synthesis of $PMOXA_6$–$PDMS_{44}$–$PMOXA_6$ ($A_6B_{44}A_6$): $A_6B_{44}A_6$ was synthesized according to the literature. [6-7] The ^{1}H-NMR spectrum is presented in Figure 4.2.

Synthesis of the aldehyde terminated $PMOXA_6$–$PDMS_{44}$–$PMOXA_6$, $A_6B_{44}A_6$-CHO: The hydroxyl terminated $A_6B_{44}A_6$ was oxidized to the aldehyde terminated $A_6B_{44}A_6$-CHO by a mild oxidation using Dess-Martin periodinane (DMP), in accordance with a published protocol with minor modifications. [8] The ^{1}H-NMR spectrum is presented in Figure 4.3.

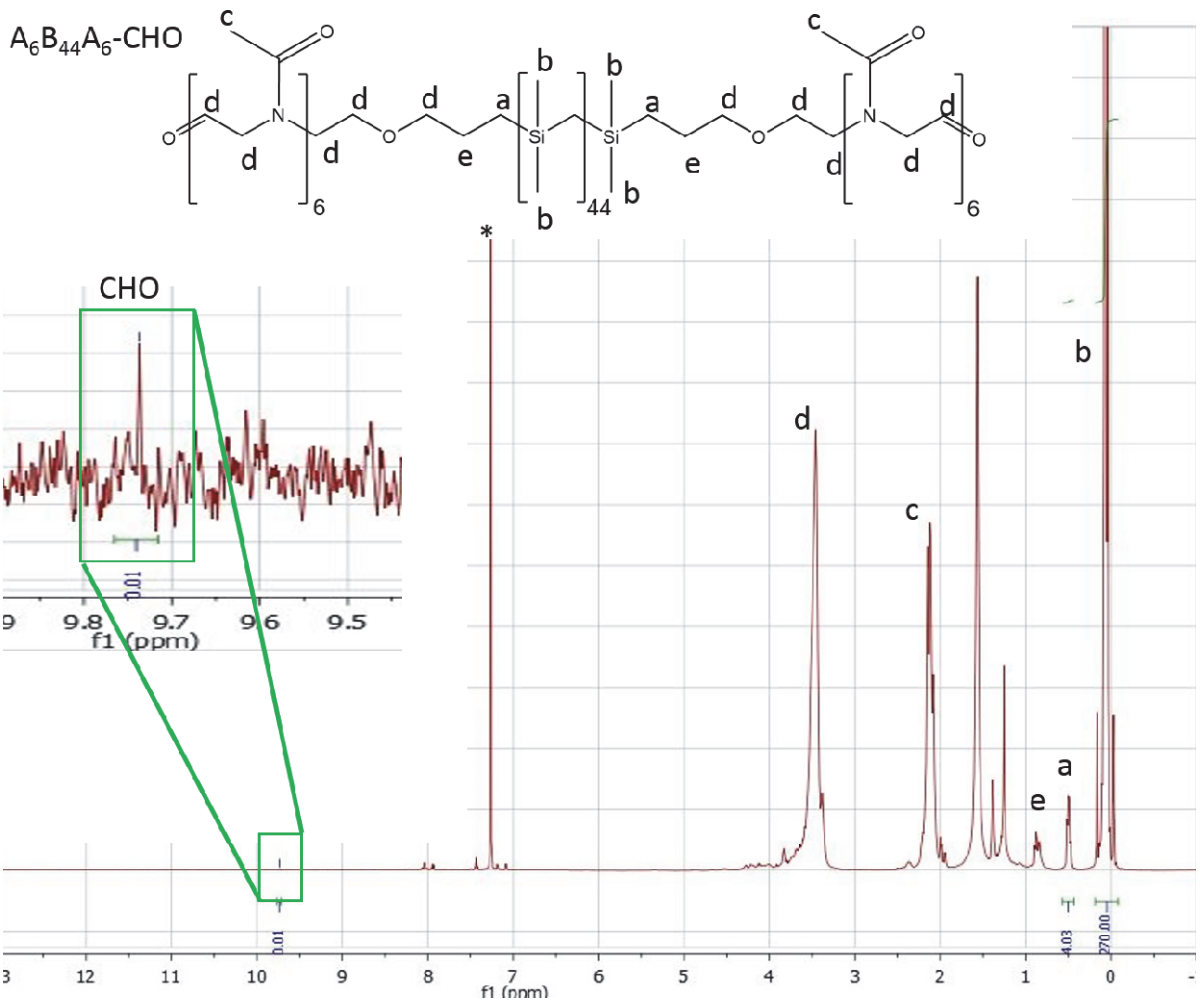

Figure 4.3. *400 MHz ^{1}H-NMR spectrum of aldehyde terminated poly(2-methyloxazoline - poly(dimethylsiloxane - poly(2-methyloxazoline) ($A_6B_{44}A_6$-CHO) in $CDCl_3$ (*)*

Comparison between the NMR spectra of $A_6B_{44}A_6$ (Figure 4.2) and $A_6B_{44}A_6$-CHO (Figure 4.3) shows that the characteristic peaks for PMOXA, at δ2.0–2.3 ppm and δ3.2–3.9 ppm, and PDMS, at at δ0.07 ppm, are present. This indicates, that the polymer backbone is unaltered by the oxidation procedure. In addition, the NMR spectrum of $A_6B_{44}A_6$-CHO (Figure 4.3) shows a small aldehyde signal, when zooming in to the region between δ9.5 and 9.9 ppm. From this signal, the amount of aldehyde present in the oxidized copolymer $A_6B_{44}A_6$-CHO was calculated to be 0.5% and the remaining 99.5% is the hydroxyl precursor. This level of aldehyde derivative was sufficient for modification of the polymersome with tpy functional groups.

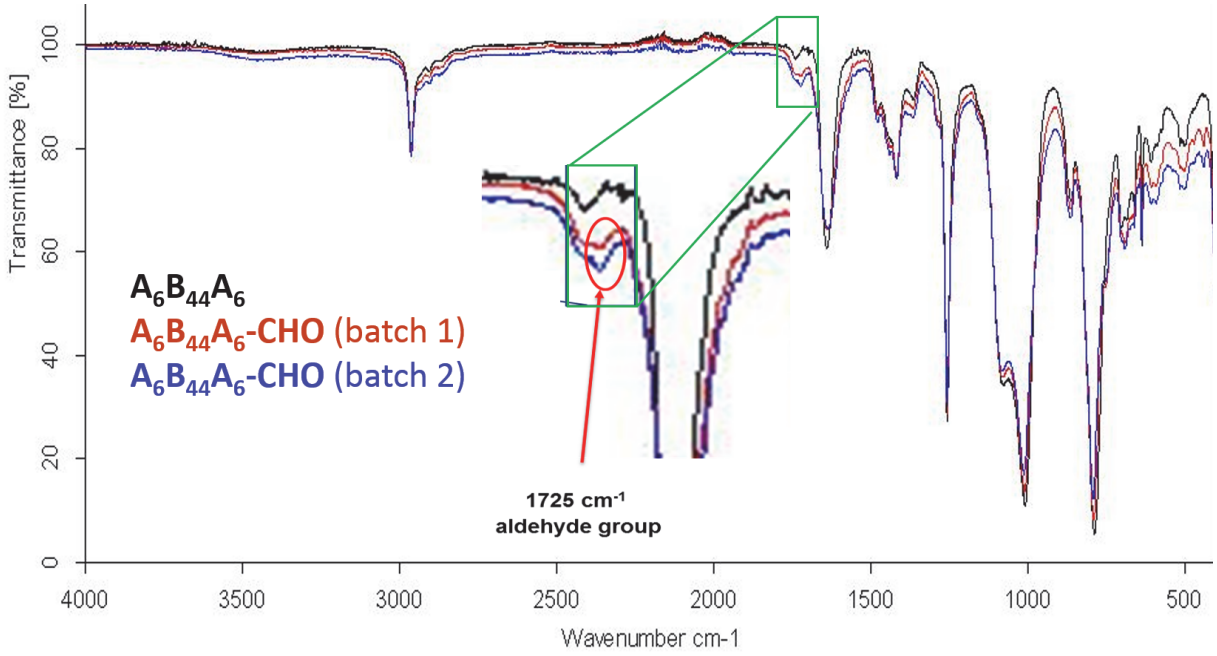

Figure 4.4. *FT-IR spectra of the hydroxyl-terminated $A_6B_{44}A_6$ copolymer (black line) and two batches of the aldehyde-terminated $A_6B_{44}A_6$-CHO copolymer (red and blue lines).*

This is confirmed by the almost identical FT-IR spectra of the two copolymers before (Figure 4.4 black line) and after oxidation (Figure 4.4 red and blue lines). It shows that the polymer chain was not altered by the oxidation. Moreover, in the zoomed-in region, a characteristic band at 1725 cm^{-1} is visible as a 'shoulder' for the aldehyde-terminated polymers (Figure 4.4 red and blue lines). This establishes successful oxidation of the copolymer hydroxyl to an aldehyde end group. The characteristics of both copolymers, the hydroxy-terminated $A_6B_{44}A_6$ and the aldehyde-terminated $A_6B_{44}A_6$-CHO, are listed in Table 4.1. The $A_6B_{44}A_6$-CHO copolymer with an aldehyde content of 0.5% is used for further experiments without further purification.

Polymer	**Sample Code**	**Composition $(A_m\text{-}B_n\text{-}A_m)^a$**	**M_n [kg/mol]^b**	**PDI^c**	**$f_{hydrophilic}$ [w/w, %]**	**Aldehyde-terminated Polymer [%]^a**
Bifunctional hydroxyl-terminated triblock copolymer	$A_6B_{44}A_6$	$PMOXA_6\text{-}PDMS_{44}\text{-}PMOXA_6$	4.5	1.8	25	0

Bifunctional aldehyde-terminated triblock copolymer	$A_6B_{44}A_6$-CHO	$PMOXA_6$-$PDMS_{44}$-$PMOXA_6$	4.5	1.8	25	0,5

Table 4.1. *Overview giving the characteristics of copolymers $A_6B_{44}A_6$ and $A_6B_{44}A_6$-CHO; [a]Determined by ^{1}H-NMR, [b,c]Determined by GPC.*

Preparation of polymersomes and their characterization

On the route towards surface immobilized polymersomes, it was necessary to prove the self-assembly of the polymer into nanocompartments and conduct full characterization before continuing with the terpyridine modification required for surface anchoring. Polymersomes were formed in three buffer solutions, in PBS, TES, HEPES, using the film rehydration method. [9]

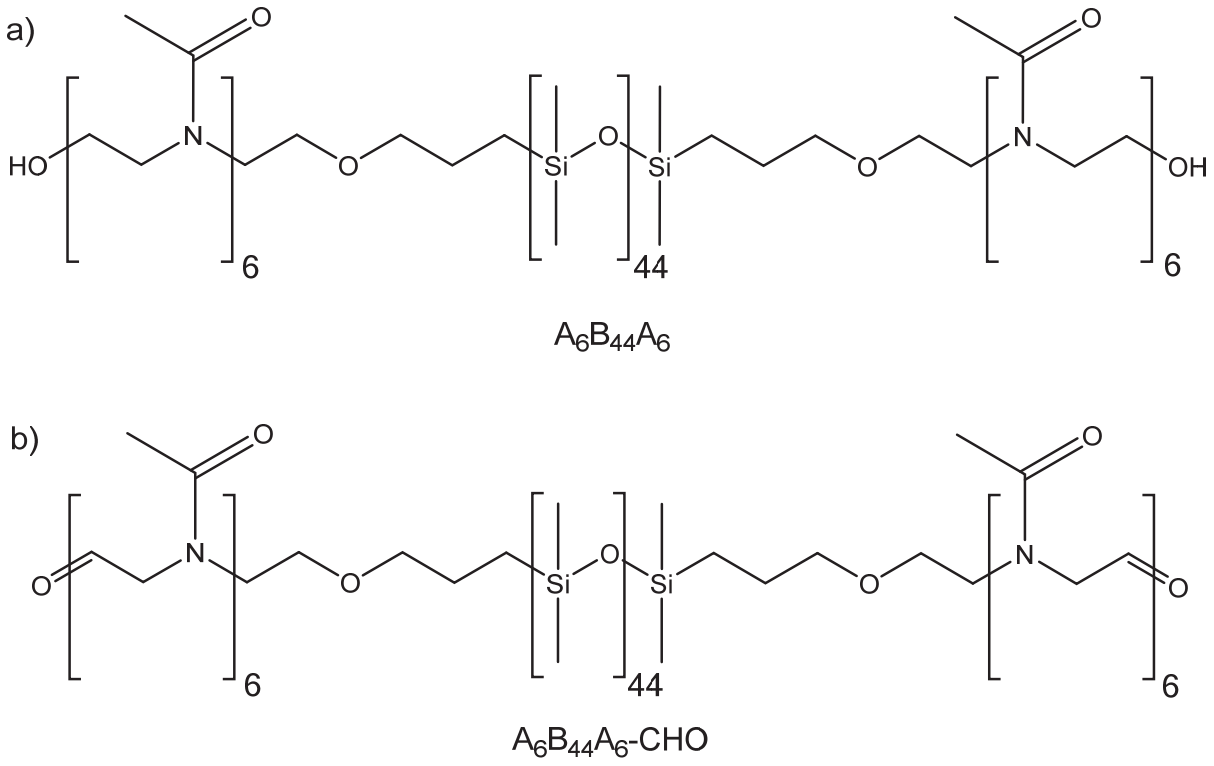

Scheme 4.1. *Structure of poly(2-methyloxazoline - poly(dimethylsiloxane - poly(2-methyloxazoline) ($A_6B_{44}A_6$) and the aldehyde modified poly(2-methyloxazoline - poly(dimethylsiloxane - poly(2-methyloxazoline) ($A_6B_{44}A_6$-CHO)*

The polymers, $A_6B_{44}A_6$ and $A_6B_{44}A_6$-CHO (Scheme 4.1), were dissolved in a small amount of chloroform. It is important to use freshly opened chloroform to prevent the reaction of the aldehydic end group of the polymer with HCl, which is one of the products of chloroform hydrolysis. [10] Alternatively chloroform can be filtered through basic aluminum oxide to remove HCl. Upon slow removal of the solvent, the polymer forms a thin film on the flask walls. Aqueous buffer is added and after gentle stirring overnight, the sample is extruded through a 200 nm pore sized filter. To choose the optimum buffer for the surface-immobilization of the polymersomes, the self-assembly process was carried out in three different buffers, PBS, TES and HEPES. The stability of the nanostructures was checked via transmission electron microscopy (TEM). TEM micrographs (Figure 4.5) indicate the formation of hollow spherical structures, with radii of up to 100 nm and a smaller population of smaller assemblies, most probably with micellar architectures. Minor amounts of smaller worm-like structures are observed, but these do not influence the experiments.

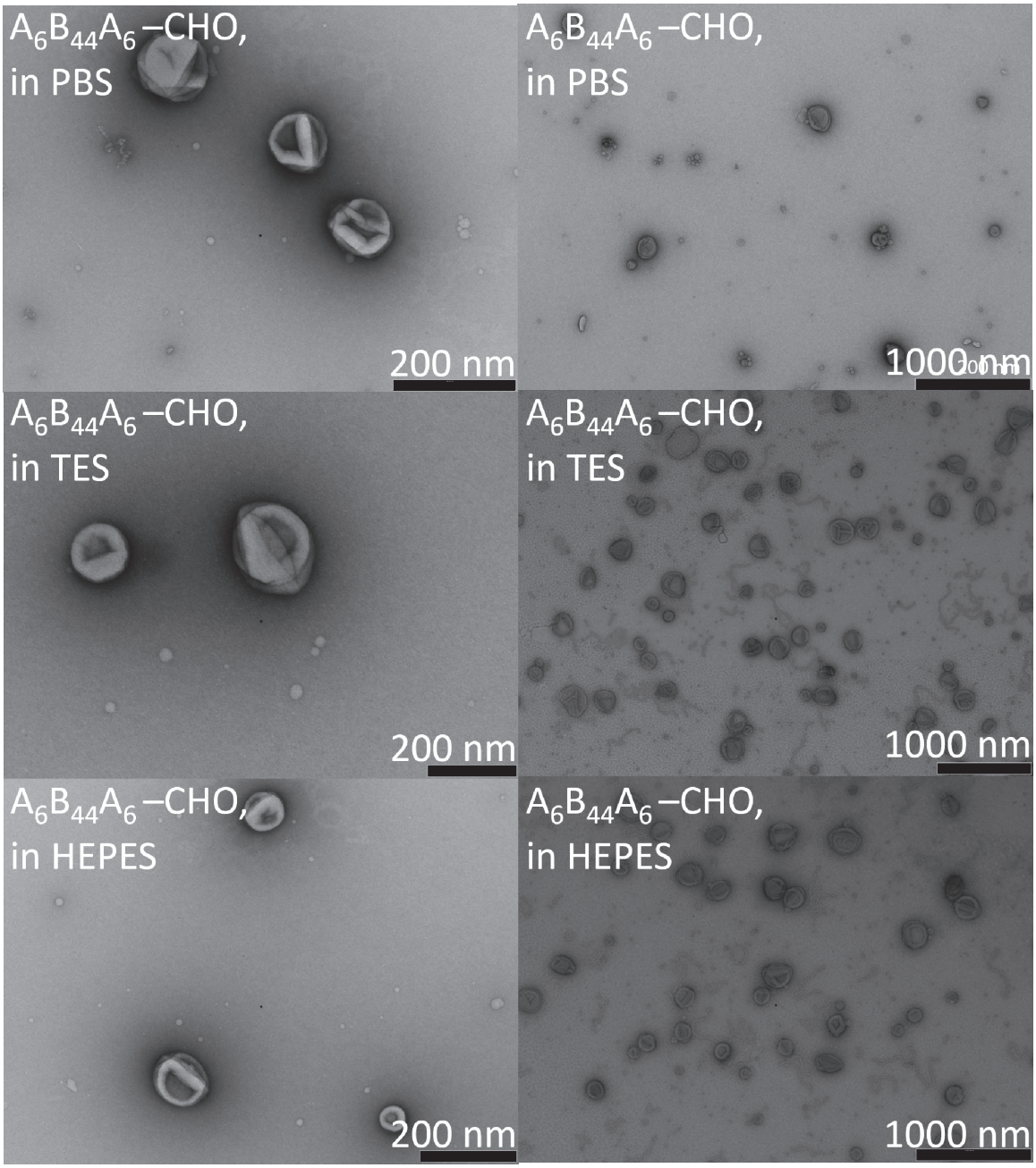

Figure 4.5. *TEM micrographs of polymersomes of modified polymer ("$A_6B_{44}A_6$-CHO") in different buffers.*

As can be seen from these micrographs, all three buffers are suitable for the self-assembly of polymersomes from $A_6B_{44}A_6$ and $A_6B_{44}A_6$-CHO. As discussed in chapter 3, PBS is very effective at removing $[Fe(tpy)_2]^{2+}$-linker units off the surface and is therefore not suitable as a solvent for the surface immobilization of polymersomes via this linking system. HEPES and TES are equally good buffers for the nanostructure self-assembly and both are considered acceptable

for the $[Fe(tpy)_2]^{2+}$-based linking system. Therefore, we decided to continue with the use HEPES (20 mM HEPES and 50 mM NaCl at pH 5.3) as a buffer for the rest of the project.

Before proceeding with the polymersome modification, it was necessary to fully characterize polymersome geometry, size and dye encapsulation efficiency. Therefore, $A_6B_{44}A_6$ and $A_6B_{44}A_6$-CHO block-copolymers were formed using the film rehydration [10] method at pH 5.3, with and without the fluorescent dye sulforhodamine B (1mM SRB in HEPES). After polymersome formation and extrusion to 200 nm, the free dye was cleaned off by using desalting devices, followed by dialysis against HEPES. The polar fluorescent SRB acts as a tracker encapsulated within the cavities of the polymer vesicles, thus proving the polymersome`s ability for cargo uptake. Additionally, SRB enables characterization specifically with fluorescence techniques. The quantity of enclosed SRB fluorophore (λ=563 nm) in the polymersomes was determined by UV-vis spectroscopy. The encapsulation efficiency (EE) is expressed as a percentage. It is defined as the ratio between the SRB concentration used for the film rehydration (C0) and the SRB concentration after encapsulation and purification (C1).

$$EE\ [\%] = {}^{C1}/_{C0}$$

Encapsulation efficiencies of up to 7% were obtained. The supramolecular structures were further analyzed using a combination of fluorescence correlation spectroscopy (FCS) and light-scattering.

FCS, is a well-established analysis method of fluorescence intensity fluctuations and holds great interest for determining interactions of fluorescent dyes with nanostructures, such as binding or encapsulation. [11, 12] It was used to confirm encapsulation of hydrophilic SRB in $A_6B_{44}A_6$ and $A_6B_{44}A_6$-CHO polymersomes, as well as for obtaining sizing information on the vesicular structures (Figure 4.6). The encapsulation of SRB within the polymersomes made out of $A_6B_{44}A_6$ and $A_6B_{44}A_6$-CHO occurred during the self-assembly process in which an SRB solution was used for rehydration. SRB encapsulated inside the cavities of the vesicles manifests itself in longer diffusion times of 7017 ± 4278 µs for $A_6B_{44}A_6$ nanostructures and 10957 ± 7854 µs for $A_6B_{44}A_6$-CHO nanostructures compared to 32 ± 2 µs for free SRB in solution. No unspecific binding was observed for empty $A_6B_{44}A_6$-CHO vesicles mixed with SRB solution. Negligible unspecific binding was observed for empty $A_6B_{44}A_6$ vesicles mixed with SRB solution in the form of a shift to longer diffusion times. When comparing the counts per molecule (CPM) for SRB-loaded $A_6B_{44}A_6$ nanocontainers, and empty $A_6B_{44}A_6$ nanocontainers

placed in an SRB solution measures of the fluorescence intensity of the auto correlation curves were CPM = 321 KHz and CPM = 9.8 KHz respectively. Thus, the unspecific binding is determined to be only a maximum of 3% of the fluorescence. The experimental auto-correlation curves and their fits based on two distinct populations of nanostructures are shown in Figure 4.6.

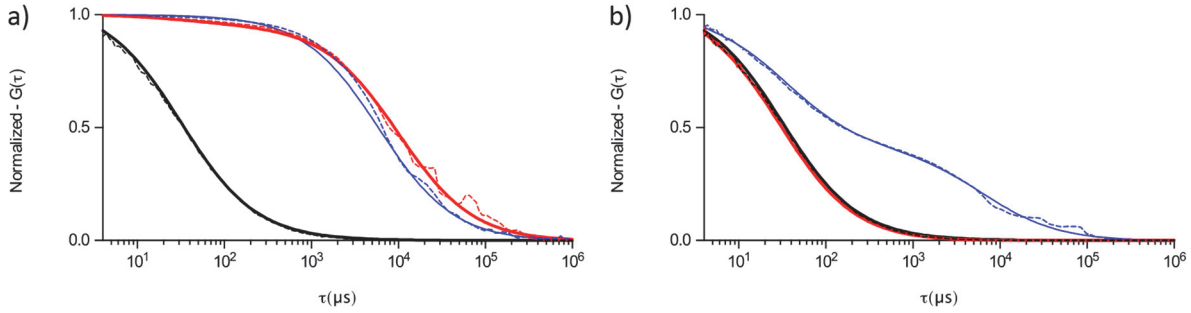

Figure 4.6. *Normalized FCS auto correlation curves; dotted lines show experimental values and solid lines show fitted values. Polymer vesicle auto correlation curves were fitted using a two-component model including a triplet state. Curves are normalized to 1 a) autocorrelation curves of free SRB in HEPES (black), SRB encapsulated in $A_6B_{44}A_6$ polymersomes (blue), SRB encapsulated in $A_6B_{44}A_6$-CHO polymersomes (red). b) Unspecific binding: autocorrelation curves of free SRB in HEPES (black), SRB mixed with $A_6B_{44}A_6$ vesicles (blue), SRB mixed with $A_6B_{44}A_6$-CHO vesicles (red).*

Light-scattering, may also be used to gain insight into the size and morphology of nanostructures. Dynamic light scattering (DLS) is a technique that can be used to determine the hydrodynamic radius (R_h), as well as the size distribution of particles in a solution or suspension. [13] Static light scattering (SLS), on the other hand, can be used to determine the radius of gyration (R_g) and average molecular weight M_w of nanoassemblies or macromolecules in solution. In combination, DLS and SLS provide the ρ-factor, which is the ratio of the two radii:

$$\rho = {}^{Rg}/_{Rh}$$

The form factor ρ gives an indication of the morphology of the assembled structures, reflecting the radial density distribution of the particle. Typical values for ρ are available in the literature, such as ρ = 1.5-1.8 for random coils, ρ = 0.78 for solid spheres and ρ = 1.0 for hollow spheres. [14-16] It is 0.95 for $A_6B_{44}A_6$ and 0.96 nm for $A_6B_{44}A_6$-CHO, which correspond to hollow spheres.

This corresponds to what is seen in TEM micrographs, which confirm the presence of large vesicular structures. The nanostructures assembled from $A_6B_{44}A_6$ and $A_6B_{44}A_6$-CHO are characterized with an R_h around 77 ± 4 and 78 ± 4 nm respectively. R_g is around 73 nm for $A_6B_{44}A_6$ and 75 nm for $A_6B_{44}A_6$-CHO. DLS data also show a minor population of smaller sized structures, which are also the same order of magnitude as in the TEM micrographs. In general the sizing information determined from SLS and DLS is in accordance with the diffusion times determined by FCS (Figure 4.6). In the light scattering data analysis, large aggregates (R_h > 500 nm) were omitted. To summarize, polymersomes have been formed based on $PMOXA_6$-$PDMS_{44}$-$PMOXA_6$ with and without aldehyde surface modification and were characterized to be hollow spheres with a diameter of roughly up to 100 nm. The analysis data are presented in Table 2.4.

Sample (Polymer) Code	SLS/DLS			FCS			UV-vis
	R_h [nm]	R_g [nm]	$\rho = R_g/R_h$	Diffusion time [µs]	Rh [nm]	Number of SRB molecules per polymersome	EE[%]
$A_6B_{44}A_6$	77 ± 4	73	0,95	7017 ± 4278	61.1± 37.3	44	7
$A_6B_{44}A_6$-CHO	78 ± 4	75	0,96	10957 ± 7854	95.43± 68.40	30	3

Table 4.2. *Characterization of nanostructures from $A_6B_{44}A_6$ and $A_6B_{44}A_6$-CHO.*

Modification of polymersomes by tpy attachment

After self-assembly of polymersomes from aldehyde activated block-copolymers and their thorough characterization in terms of size and morphology, these polymersomes now had to be equipped with a tpy functionality to be able to prepare polymersome-modified surfaces.

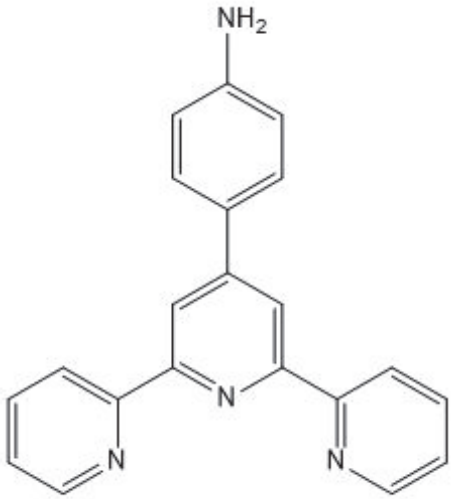

3

Scheme 4.2. Structure of *4-([2,2':6',2''-terpyridin]-4'-yl)aniline (ligand **3**)*

After self-assembly of polymersomes from $A_6B_{44}A_6$-CHO block-copolymers via film rehydration, the polymersomes were modified by addition of ligand **3** (Scheme 4.2, 2 eq **3** per 1 eq of polymer) in THF (samples further referred to as "ligand"). As a control, polymersomes were also prepared from $A_6B_{44}A_6$, to which ligand **3** in THF was added. A second control was made by adding only THF to both polymersomes from $A_6B_{44}A_6$-CHO and $A_6B_{44}A_6$ (samples further referred to as "no ligand"). The Schiff base condensation results in the covalent attachment of the tpy unit to the polymersome. The imine forms under mild conditions in aqueous medium (Scheme 4.3). No catalyst was necessary. [17, 18] Excess ligand was removed by dialysis against HEPES.

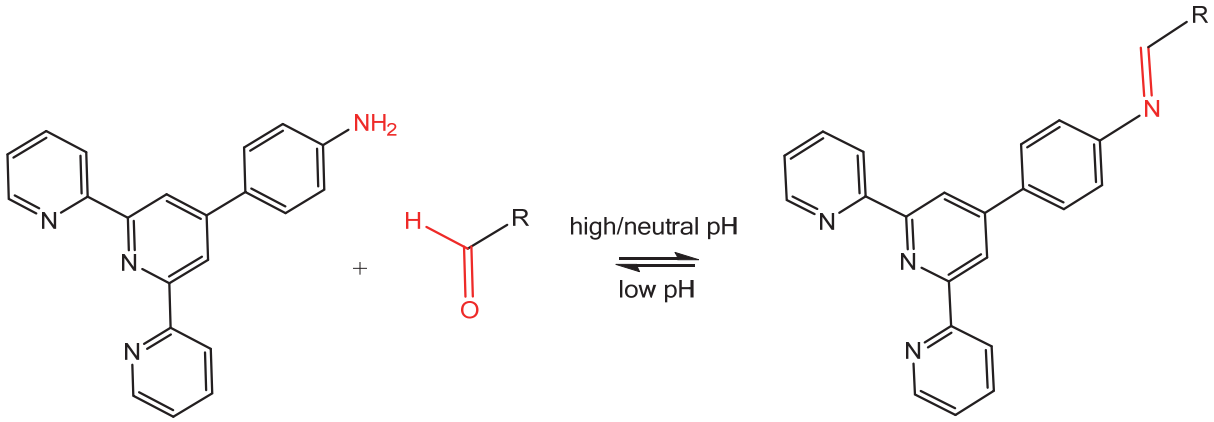

Scheme 4.3. *Imine formation, or Schiff base reaction, from a primary amine and an aldehyde. R represents the polymersome.*

To ensure polymersome stability in the presence of ligand **3** in THF, TEM micrographs (Figure 4.7) were recorded after addition of **3** in THF or THF alone. They show spherical assemblies and radii similar to those observed before addition of **3**/THF. Collapsed vesicular structures in the micrographs point towards the polymersomes preserving their spherical shape upon addition of ligand **3**/THF, i.e. they are spherical prior to their collapse during the TEM measurement.

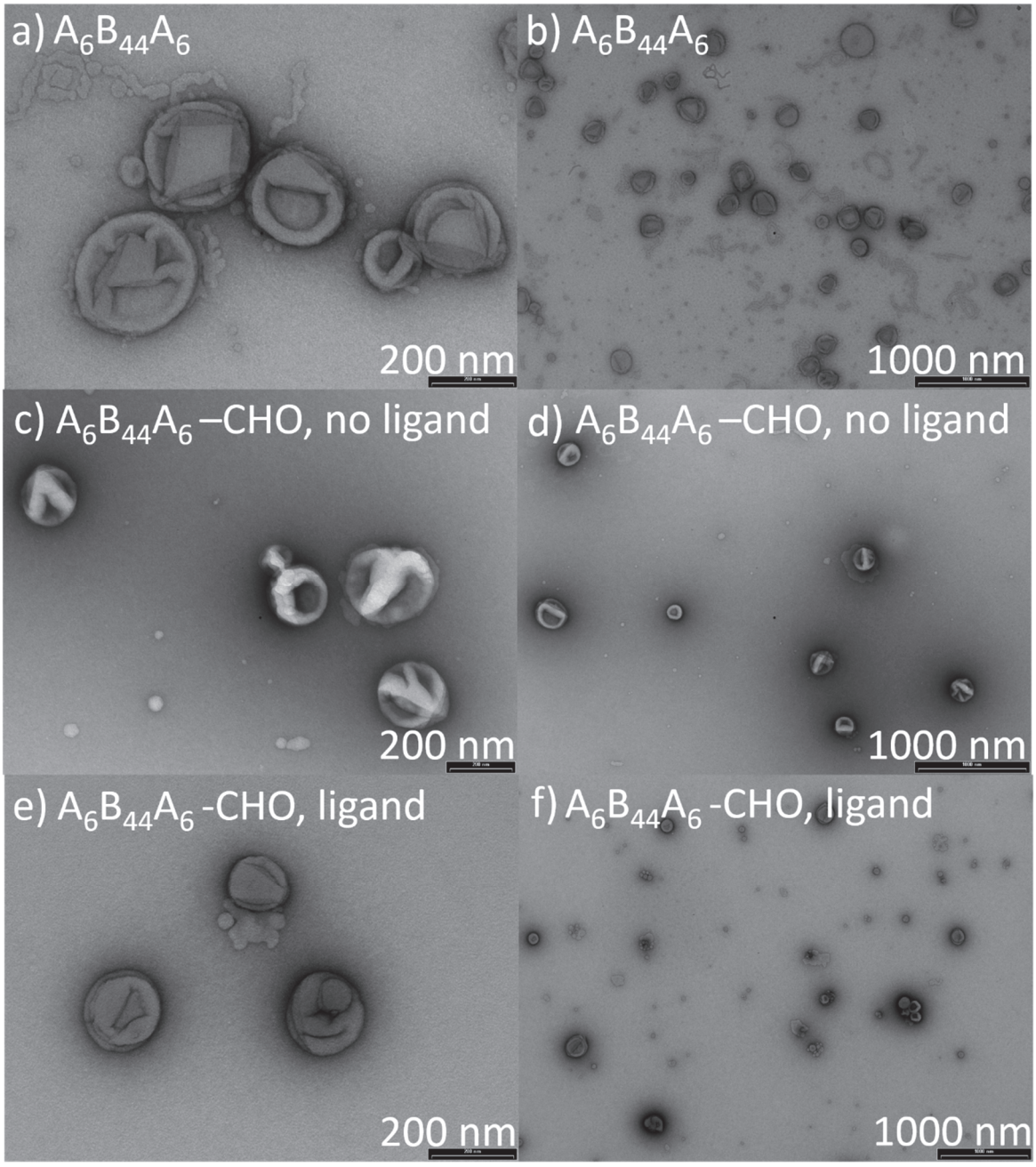

Figure 4.7. *TEM micrographs of a,b) polymersomes from unmodified polymer (sample "$A_6B_{44}A_6$"); c,d) polymersomes from aldehyde functionalized polymer in the presence of THF (sample "$A_6B_{44}A_6$-CHO, no*

*ligand"); e,f) polymersomes from aldehyde functionalized polymer in the presence of ligand **3** in THF (sample "$A_6B_{44}A_6$-CHO, ligand")*

Conclusion

In this chapter, we discussed modification of an amphiphilic block copolymer, the formation and characterization of polymer vesicles and their functionalization with tpy units. The terminal hydroxyl groups of the bifunctional amphiphilic triblock copolymer $A_6B_{44}A_6$ were successfully oxidized to aldehyde end groups in $A_6B_{44}A_6$-CHO using Dess-Martin periodinane (DMP). Both polymers were characterized and the aldehyde content was determined to be 0.5% with the remaining 99.5% being the hydroxyl terminated precursor. Both polymers were self-assembled into nanostructures with and without the fluorescent SRB and fully characterized by TEM, light scattering, UV-vis and FCS. They were shown to assemble into hollow spheres with dye encapsulation efficiencies of up to 7%, whereas unspecific binding was shown to be between 0 to 3%. Polymersomes formed from $A_6B_{44}A_6$-CHO have a hydrodynamic radius, R_h, of 78 nm on average and a radius of gyration, R_g, of approximately 75 nm. Polymersomes from $A_6B_{44}A_6$ have radii in the same order of magnitude, of 77 nm (R_h) and 73 nm (R_g). Lastly, polymer vesicles from aldehyde-terminated copolymer were modified by condensation with ligand **3**, which led to the covalent attachment of a tpy unit to the polymersomes.

References

[1] K. Langowska, J. Kowal, C. G. Palivan, W. Meier, *J. Mater. Chem. B,* 2014, **2**, 4684.

[2] P. Tanner, O. Onaca, V. Balasubramanian, W. Meier, C. G. Palivan, *Chem. Eur. J.*, 2011, **17**, 4552.

[3] X. Hu, Y. Zhang, Z. Xie, X. Jing, A. Bellotti, Z. Gu, *Biomacromolecules*, 2017, **18**, 649.

[4] Z. Y. Qiao, J. Cheng, R. Ji, F.-S. Du, D.-H. Liang, S.-P. Ji, Z.-C. Li, *RSC Adv.*, 2013, **3**, 24345.

[5] C. Sanson, J.-F. Le Meins, C. Schatz, A. Soum, S. Lecommandoux, *Soft Matter*, 2010, **6**, 1722.

[6] F. Itel, M. Chami, A. Najer, S. Lörcher, D. Wu, I. A. Dinu, W. Meier, *Macromolecules*, 2014, **47**, 7588.

[7] C. Nardin, S. Thoeni, J. Widmer, M. Winterhalter, W. Meier, W. *Chem. Commun.,* 2000, **15**, 1433.

[8] J. Ł. Kowal, J. K. Kowal, D. Wu, H. Stahlberg, C. G. Palivan, W. P. Meier, *Biomaterials* 2014, **35**, 7286.

[9] B. M. Discher, Y.-Y. Won, D. S. Ege, J. C.-M. Lee, F. S. Bates, D. E. Discher, D. A. Hammer, *Science* 1999, **284**, 1143.

[10] S. C. Chuang, J. W. Bozzelli, *Environ. Sci. Technol.*, 1986, **20**, 568.

[11] A. Najer, D. Wu, A. Bieri, F. Brand, C. G. Palivan, H.-P. Beck, W. Meier, *ACS Nano,* 2014, **8**, 12560.

[12] X. Zhang, M. Lomora, T. Einfalt, W. Meier, N. Klein, D. Schneider, C. G. Palivan, *Biomaterials*, 2016, **89**, 79.

[13] H. Gould, J. Tobochnik, *Am. J. Phys.*, 1999, **67**, 1043.

[14] J. Hotz, W. Meier, *Langmuir,* 1998*,* **14**, *5.*

[15] S. U. Egelhaaf, P. Schurtenberger, *J. Phys. Chem*., 1994, **98**, 8560.

[16] W. Burchard, In *Physical Techniques for the Study of Food Biopolymers*, Ed. S. B. Ross-Murphy, Blackie Academics & Professional, Glasgow, 1994.

[17] W. Qin, S. Long, M. Panunzio, S. Biondi, *Molecules,* 2013, **18**, 12264.

[18] M. J. O'Donnell, R. L. Polt, *J. Org. Chem.,* 1982, **47**, 2663.

Chapter 5

Surface Anchoring of Polymersomes

Abstract

Terpyridine-modified polymersomes were immobilized on smooth FTO/TiO_2 surfaces and on titania-coated quartz crystal sensors through the previously optimized stepwise assembly of an iron(II) terpyridine complex connecting the two components, surface and polymersomes. The successful immobilization was monitored by CLSM measurements and it was confirmed, that binding depends solely on the co-presence of the ligand 4-([2,2':6',2''-terpyridin]-4'-yl)aniline and the aldehyde group on the polymer. We also found that shaking the sample during the surface immobilization has no significant effect. Single vesicles with preserved architectures were imaged by AFM and their heights were measured. Height traces showed that they were between 20 and 70 nm, with the majority around 20 nm in height, which is in accordance with twice the membrane thickness of the amphiphilic triblock copolymer.

Motivation and Problem Definition

Active surfaces have become more and more popular. They can be engineered to respond to their environment by signaling changes or actively producing compounds on demand. They usually consist of a solid support to which active substances such as enzymes, antibodies or functional synthetic molecules can be covalently attached to achieve stimuli-responsiveness. For their tunable properties, the application spectrum for active surfaces is broad. Applications include self-healing surfaces, sensors and antibacterial surfaces. [1-8] One elegant strategy towards the creation of active surfaces is the immobilization of nanocompartments on solid substrates. The usage of polymersomes is favored due to their higher mechanical stability compared with liposomes and the possibility to modify and decorate their membrane which makes them ideal candidates for sensors and cargo release systems based on different stimuli. Further, polymersomes were used to protect active molecules like sensitive enzymes from the environment by their encapsulation inside these confined spaces and if the membrane is equipped with biopores enzymatic reactions can be carried out on demand inside the cavities of these so called nanoreactors. The immobilization of polymersomes in general is an elegant solution towards the generation of active surfaces for bio-applications.

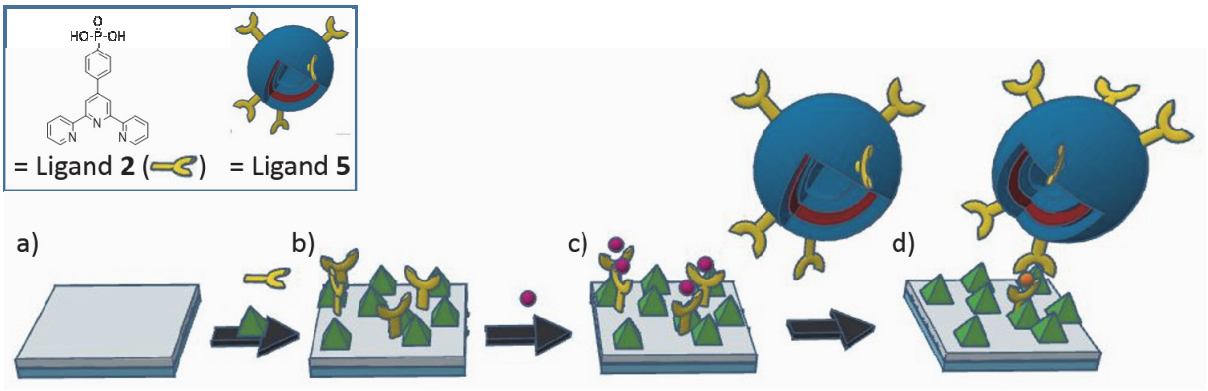

Figure 5.1. *Schematic representation of stepwise assembly process, that leads to surface-bound polymersomes. The ligand introduced in going from a) to b) is ligand* ***2****. The tpy-functionalized polymersome introduced in step c) is called ligand* ***5****. Coadsorbants are shown in green.*

Therefore, the focus this chapter is the immobilization of polymersomes on solid surfaces via the $[Fe(tpy)]^{2+}$-core unit, meaning all the single components, which were optimized in the previous chapters have now to be put together. (Figure 5.1). The smoothed FTO/TiO_2 surfaces (Figure 5.1a) were treated with a mixture of ligand **2** and the coadsorbant *tert*-

butylphosphonic acid to obtain spatially separated surface-anchored ligand **2** (Figure 5.1b). By subsequent treatment with aqueous iron(II) chloride the active $[Fe(\mathbf{2})]^{2+}$ moiety was generated on the surface (Figure 5.1c), which is then able to bind terpyridine-modified polymersomes to get surface immobilized polymersomes (Figure 5.1d).

Surface anchoring of polymersomes

The smoothed, glass-supported titania surface was treated with ligand **2**, then $FeCl_2$ (aq), then tpy-functionalized polymersome. The smoothed surfaces described in chapter 2, i.e. the FTO-glass substrate covered with 7 spin-coated titania layers, was treated as described in chapter 3. The optimized conditions for surface anchoring of $[Fe(tpy)_2]^{2+}$ were used, with the exception that instead of the ancilliary ligand **2** or **4**, that were used in chapter 3, the tpy-functionalized polymersomes were used. The tpy-modified polymersome vesicles are now used as a ligand and are further referred to as **5**. This means the first dipping step consists of a solution of 100 mM *tert*-butylphosphonic acid and 1 mM ligand **2**. This was followed by treatment with aqueous $FeCl_2$ and finally by treatment with **5**.

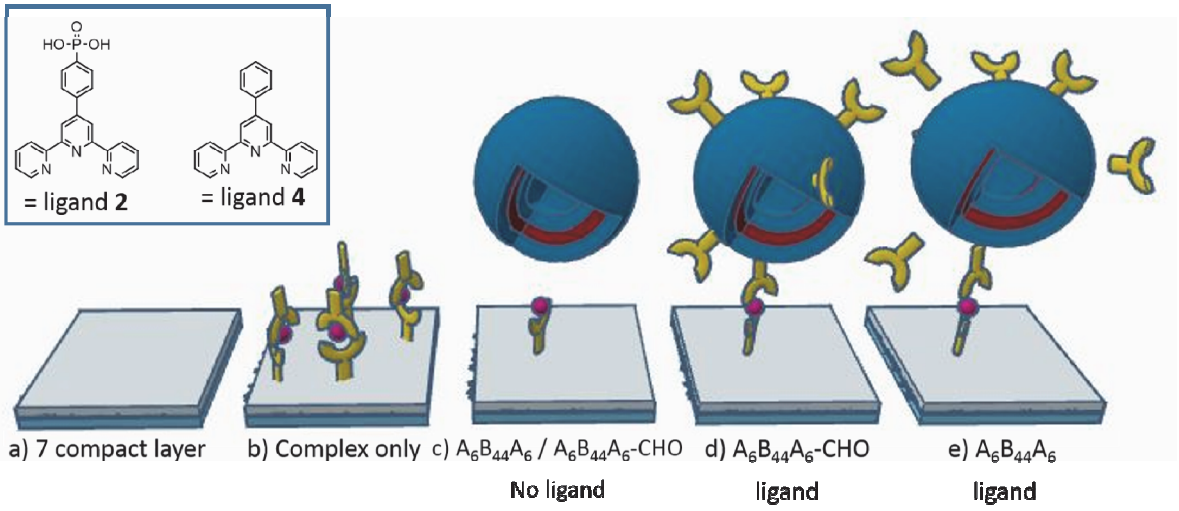

Figure 5.2. *Schematic representation of sample codes used for surface characterization measurements (CLSM, liquid AFM); a) control "7 compact layer": spin coated titania surfaces without any complex on the surface; b) control "Complex only": the $[Fe(\mathbf{2})(\mathbf{4})]^{2+}$-complex on the spin coated titania surfaces; c) references "$A_6B_{44}A_6$ / $A_6B_{44}A_6$-CHO No ligand": modified or unmodified polymer without any ligand; d) sample "$A_6B_{44}A_6$-CHO ligand": surface-anchored $[Fe(\mathbf{2})(\mathbf{5})]^{2+}$; e) reference "$A_6B_{44}A_6$ ligand": polymersomes from unmodified polymer with ligand **4** in the same solution. Consider that polymersomes, complex and surface are not scaled to their relative sizes.*

To prove anchoring of the polymersomes, imaging of the surfaces was carried out using CLSM and AFM. Both AFM and CLSM measurements were conducted in liquid to preserve the polymersomes' architectures. All polymersomes were formed in the presence of the fluorescent dye SRB as described in the previous chapter. Figure 5.2 illustrates the makeup of the surfaces to generate the polymersome decorated sample, as well as the references and the controls. Controls were FTO-glass with 7 spin-coated titania layers, without (Figure 5.2a, sample "7 compact layers") and with surface anchored [Fe(**2**)(**4**)]$^{2+}$ (Figure 5.2b, sample "complex only"). References were generated assembling [Fe(**2**)]$^{2+}$ on the surface followed by treatment with polymersomes from modified or unmodified polymer without any ligand (Figure 5.2c, sample "$A_6B_{44}A_6$ no ligand" and "$A_6B_{44}A_6$-CHO no ligand") or polymersomes from unmodified polymer with ligand **4** in the same solution (Figure 5.2e, sample "$A_6B_{44}A_6$ ligand"). The sample (Figure 5.2d, sample "$A_6B_{44}A_6$-CHO ligand") with surface-bound polymersomes was generated by assembling [Fe(**2**)]$^{2+}$ followed by treatment with **5**. To determine whether shaking has an effect on surface binding, some samples were placed on a shaker during the last step dipping procedure (sample "shaking"), whereas some were not (sample "no shaking").

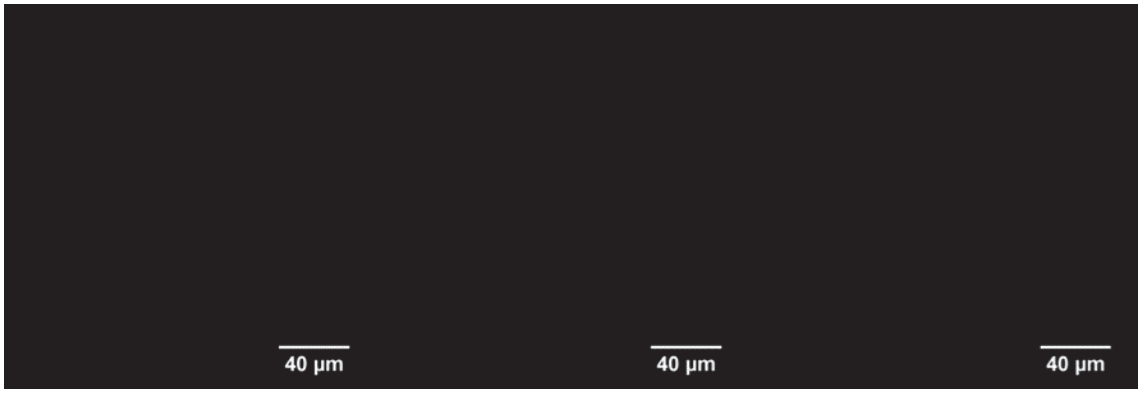

Figure 5.3. *CLSM (raw) images of 3 different spots on the control "7 compact layer".*

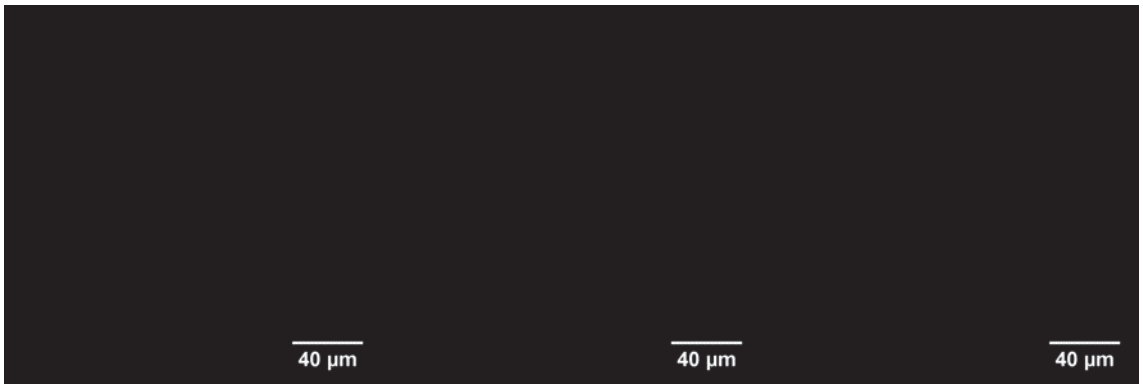

Figure 5.4. *CLSM (raw) images of 3 different spots on the control "complex only".*

No fluorescence signal was detected when measuring different spots on the two controls “7 compact layer” and “complex only”, revealing, that neither surface, nor the $[Fe(tpy)_2]^{2+}$ complex exhibit fluorescence (Figure 5.3 and 5.4).

The samples “$A_6B_{44}A_6$ ligand no shaking” (Figure 5.5) and “$A_6B_{44}A_6$ ligand shaking” (Figure 5.6) show, with very few exceptions, almost no fluorescence. The images, that show fluorescence, show inhomogeneous patches assumed to be agglomerates. Very likely these remnants resulted from the tweezers, which were used to hold the sample and the area under the tweezers was not adequately washed. Nevertheless, the intensities from these images were taken into account for the average values.

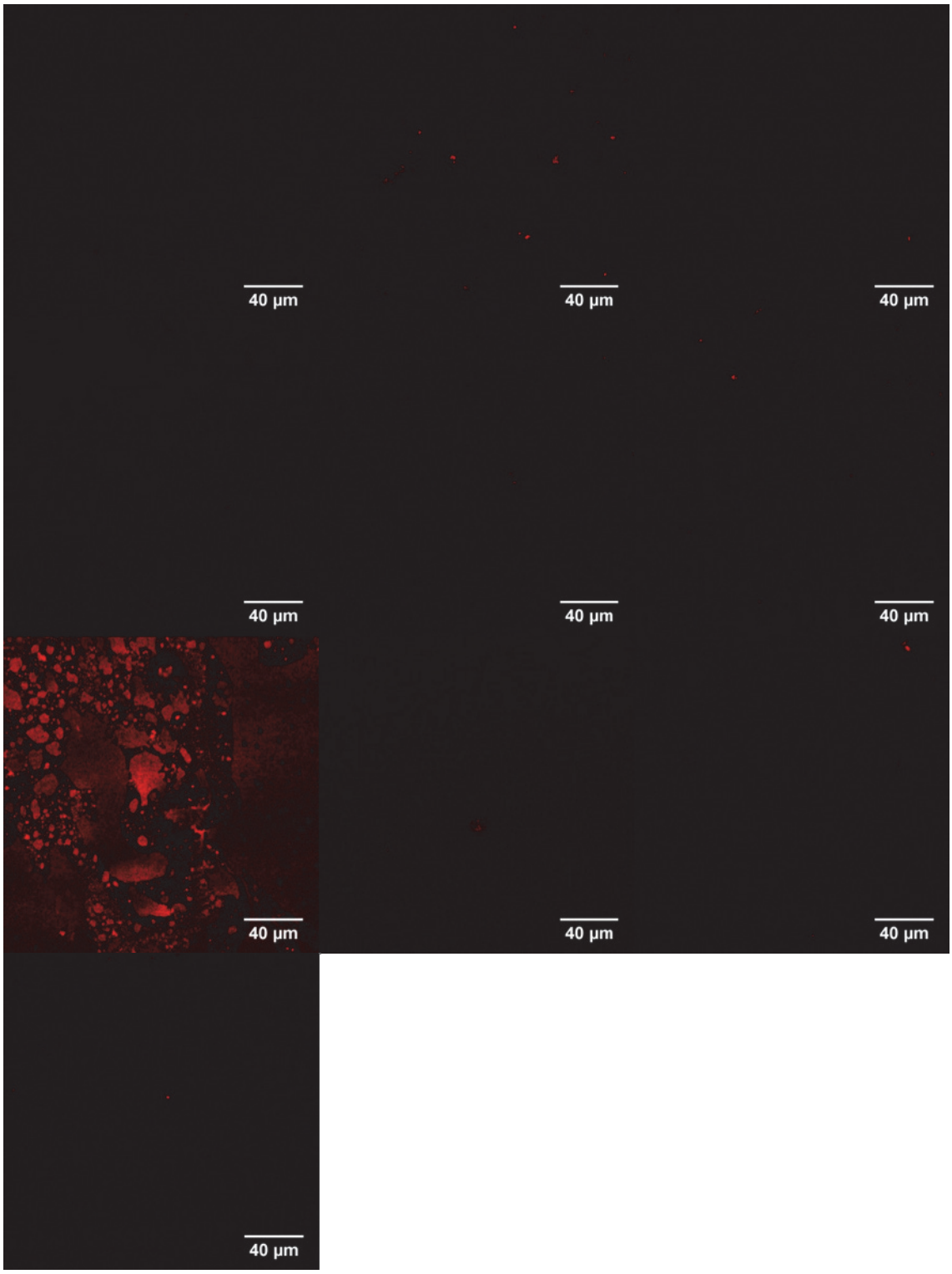

Figure 5.5. *CLSM (raw) images of 10 different spots on the sample "$A_6B_{44}A_6$ ligand no shaking".*

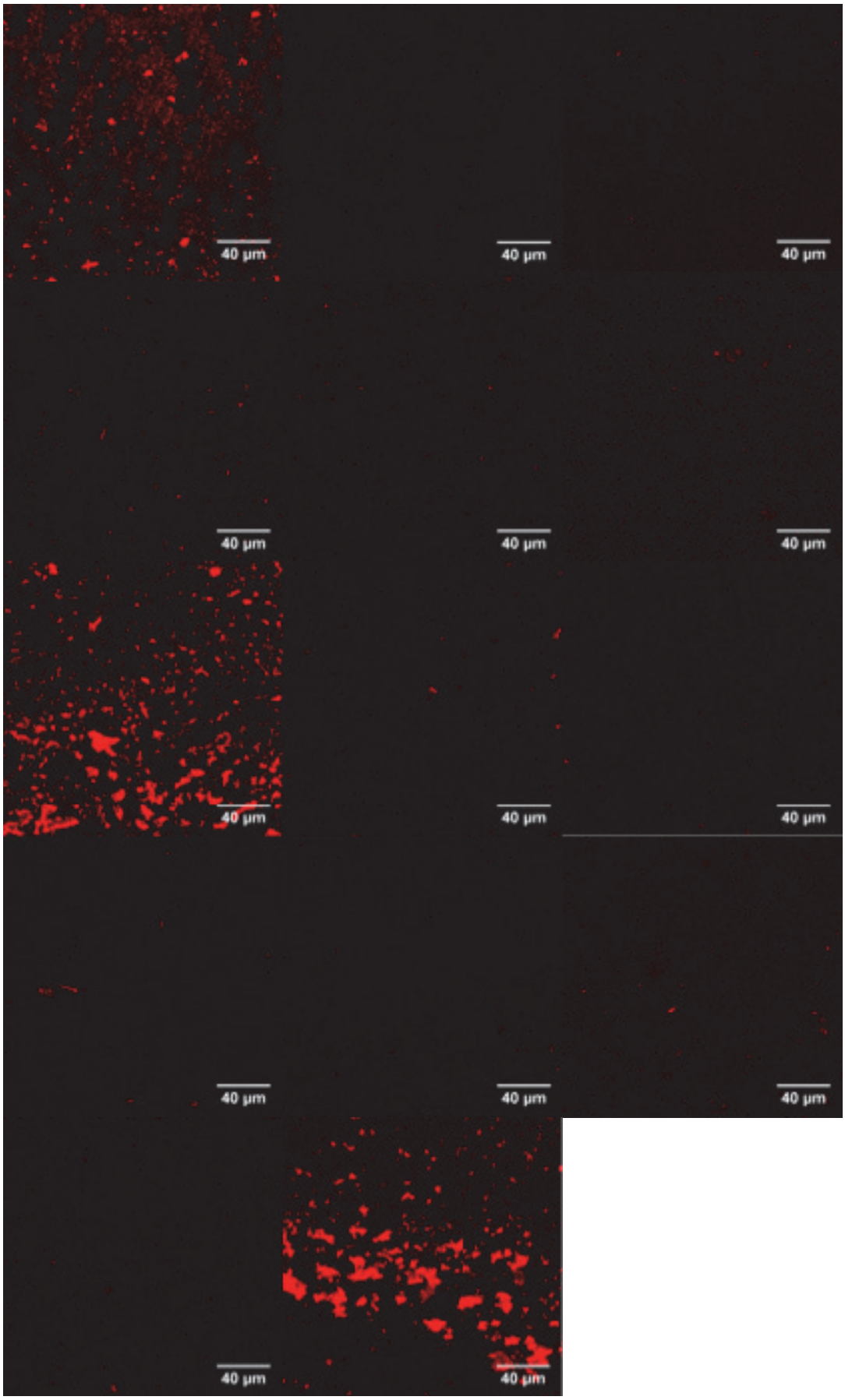

Figure 5.6. *CLSM (raw) images of 14 different spots on the sample "$A_6B_{44}A_6$ ligand shaking".*

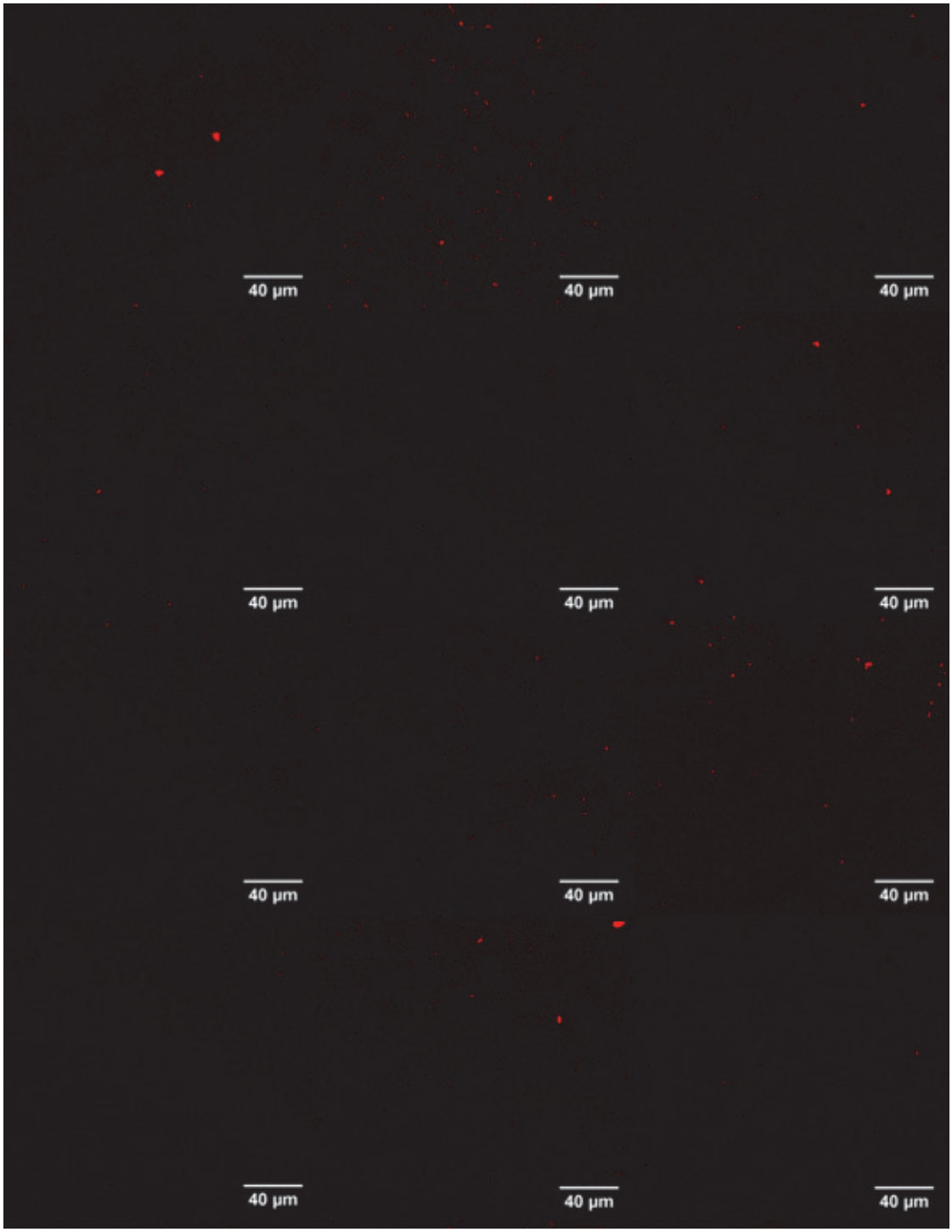

Figure 5.7. *CLSM (raw) images of 12 different spots of sample "$A_6B_{44}A_6$ no ligand no shaking".*

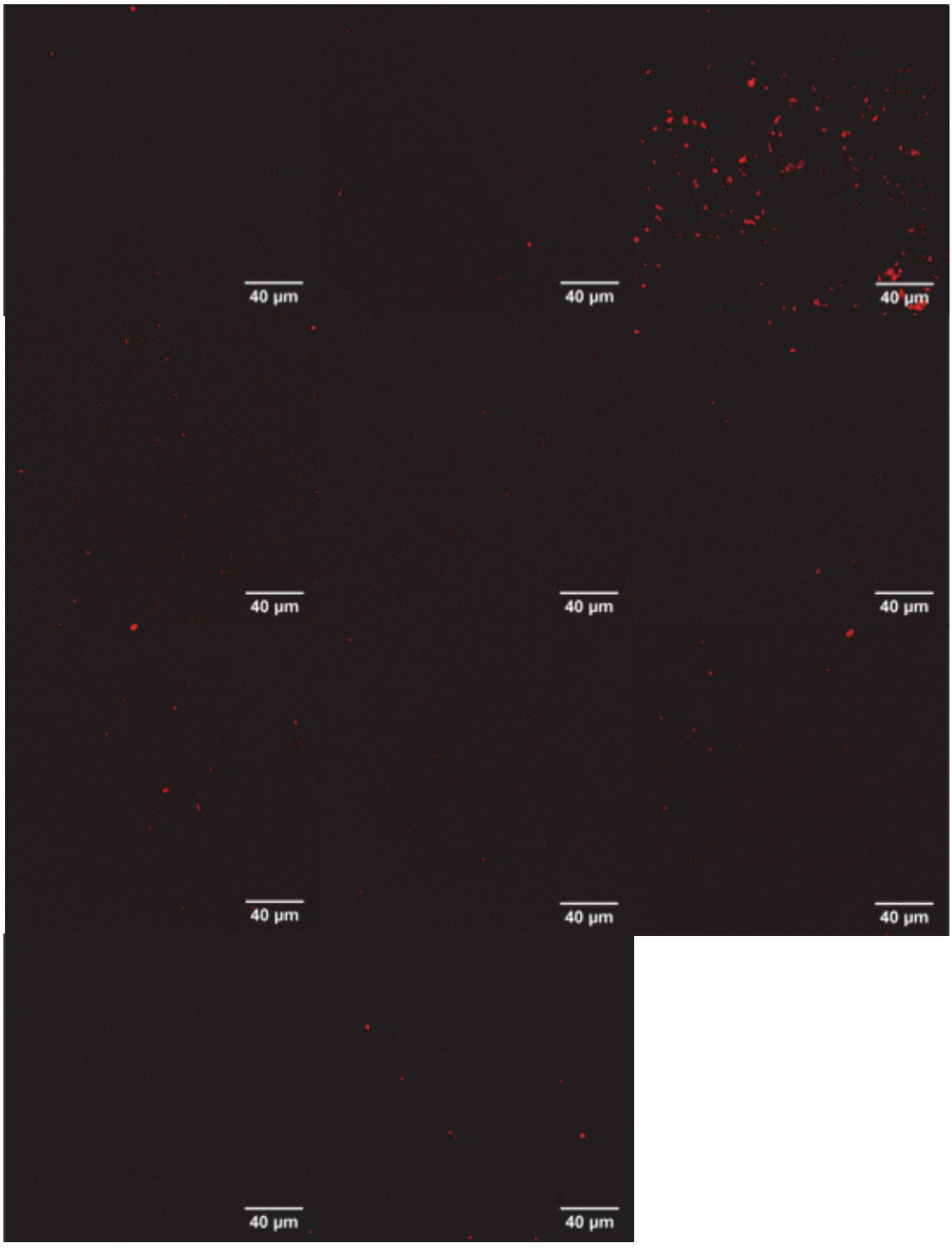

Figure 5.8. *CLSM (raw) images of 11 different spots of sample "$A_6B_{44}A_6$ no ligand shaking".*

Almost no fluorescence is detectable when no aldehyde group, as is the case for the references "$A_6B_{44}A_6$ ligand" (Figure 5.5 and 5.6), or ligand, as in the references "$A_6B_{44}A_6$ no ligand" (Figure 5.7 and 5.8), is present. Again, for these samples there does not seem to be a difference in fluorescence intensity between the samples that were shaken and those, which were not shaken. This leads to the conclusion that shaking has no influence on surface binding.

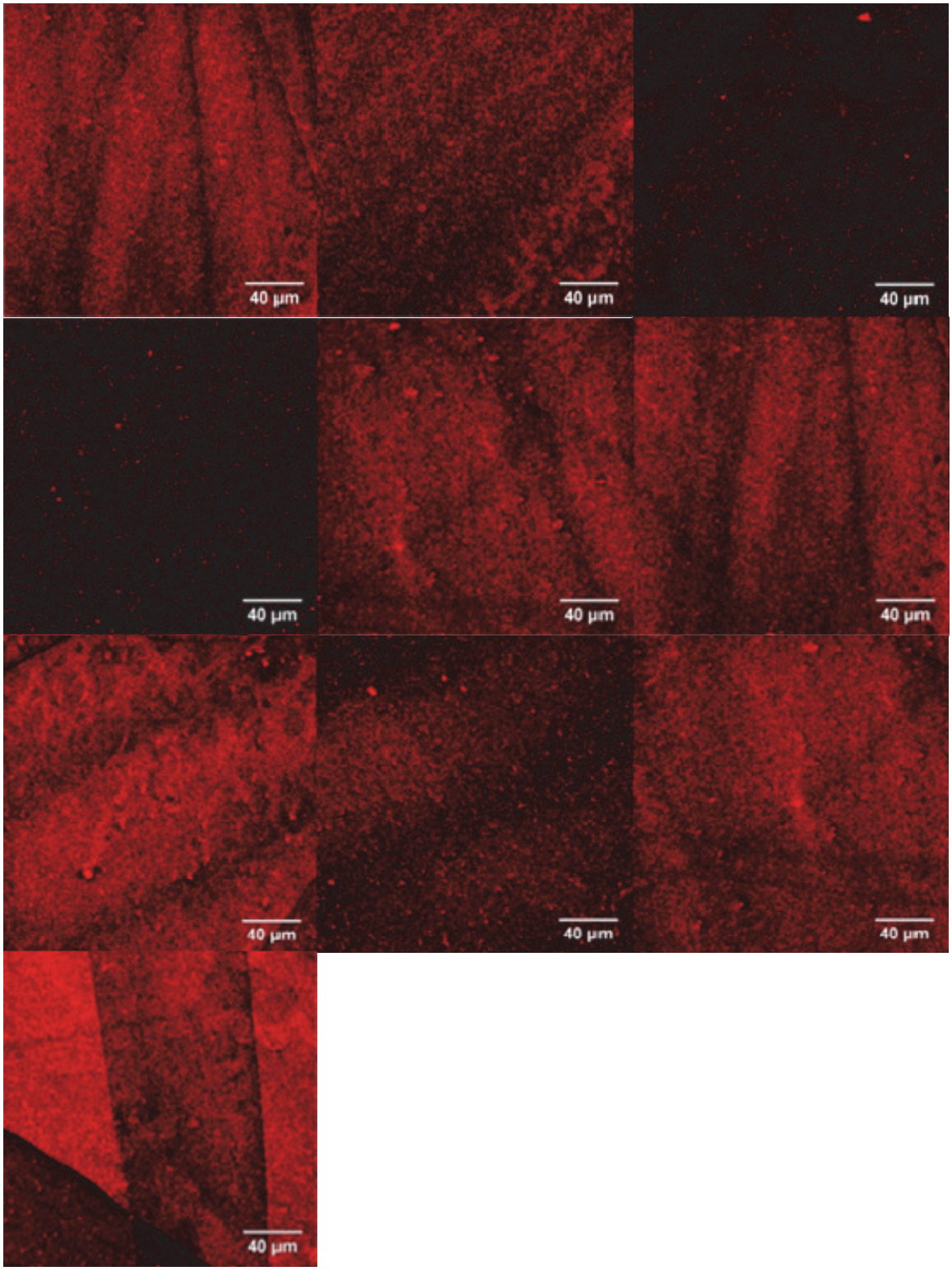

Figure 5.9. *CLSM (raw) images of 10 different spots of the sample "$A_6B_{44}A_6$-CHO ligand no shaking".*

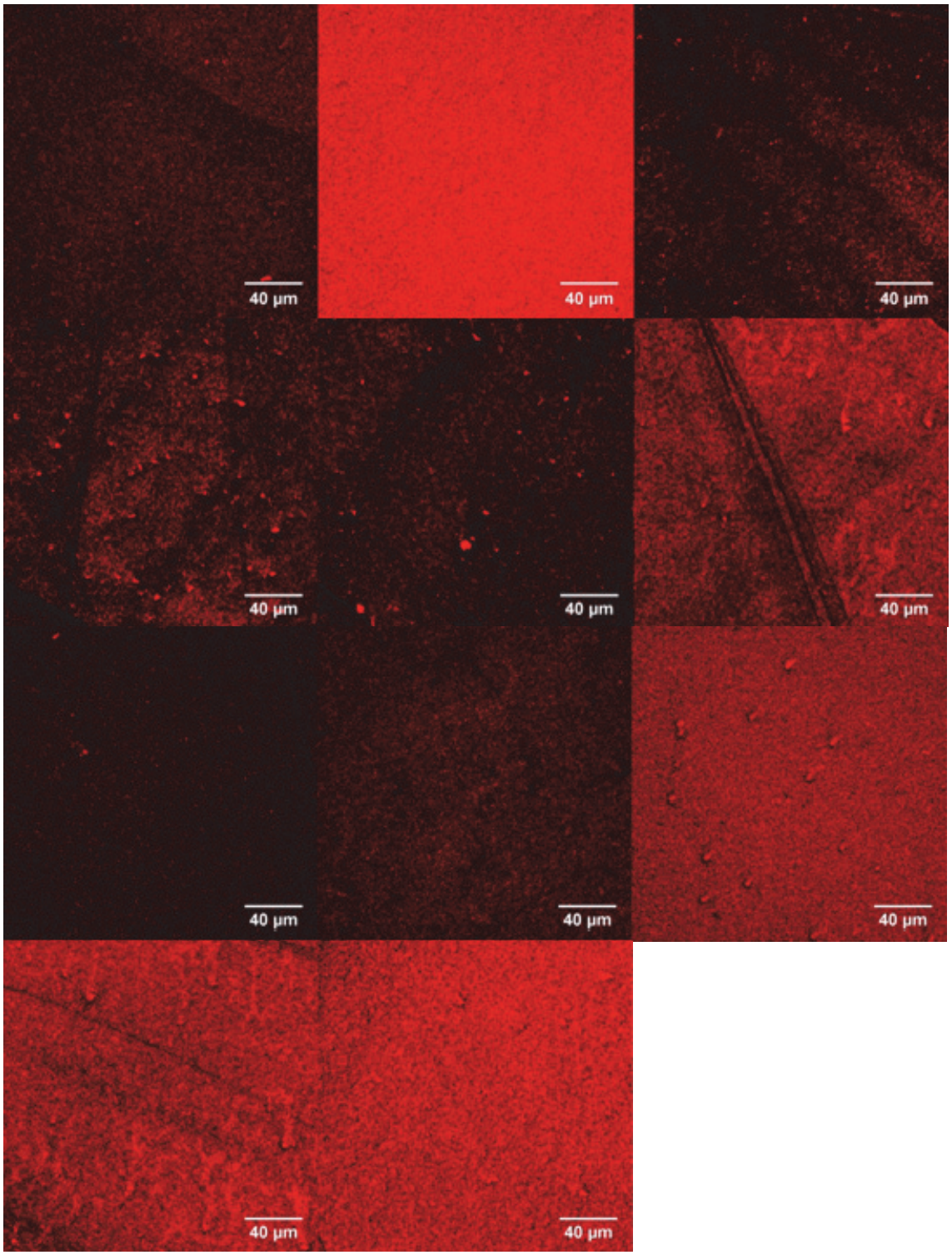

Figure 5.10. *CLSM (raw) images of 11 different spots of the sample "$A_6B_{44}A_6$-CHO ligand shaking".*

Both the samples, "$A_6B_{44}A_6$-CHO ligand no shaking" (Figure 5.9) and "$A_6B_{44}A_6$-CHO ligand shaking" (Figure 5.10) showed a bright and uniformly distributed fluorescence on the surface. This indicates that polymersomes are evenly distributed over the surface. Any inhomogeneity seems to come from the surface structure, that may have been caused by the handling or the spin-coating process.

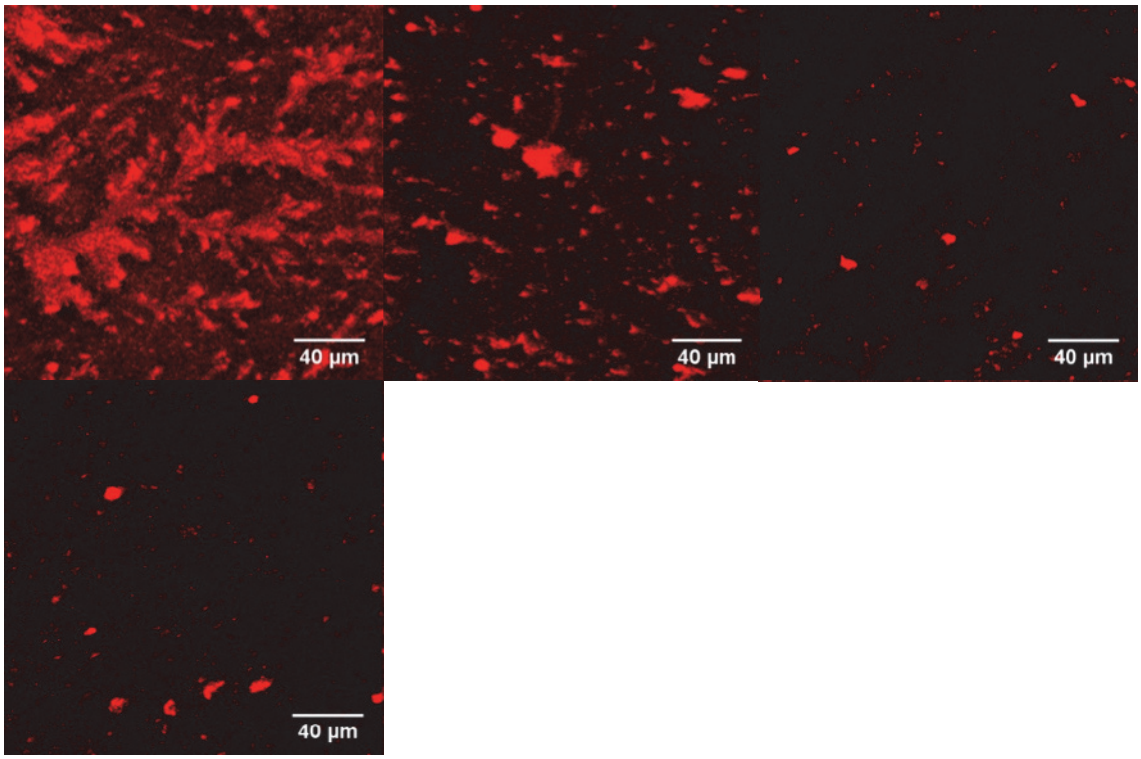

Figure 5.11. *CLSM (raw) images of 4 different spots of the sample "$A_6B_{44}A_6$-CHO no ligand no shaking".*

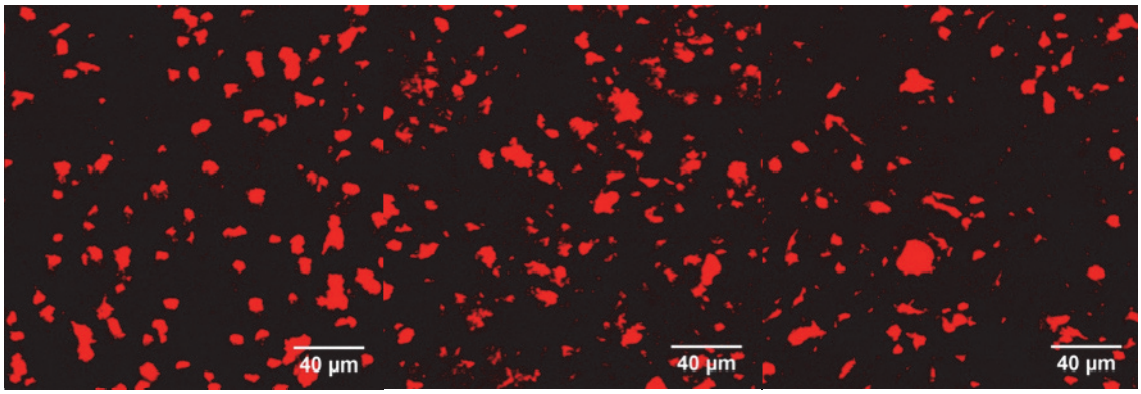

Figure 5.12. *CLSM (raw) images of 3 different spots of sample "$A_6B_{44}A_6$-CHO no ligand shaking".*

In the samples made from aldehyde-functionalized polymer, but without terpyridine ligand, "$A_6B_{44}A_6$-CHO no ligand no shaking" (Figure 5.11) and "$A_6B_{44}A_6$-CHO no ligand shaking" (Figure 5.12), bright fluorescent spots are visible on the non-fluorescent background. This discovery can be explained by the findings of Klonos et al., stating, that the polymer forms a layer of reduced mobility on the surface, [9, 10] causing the inhomogeneous appearance of the surface.

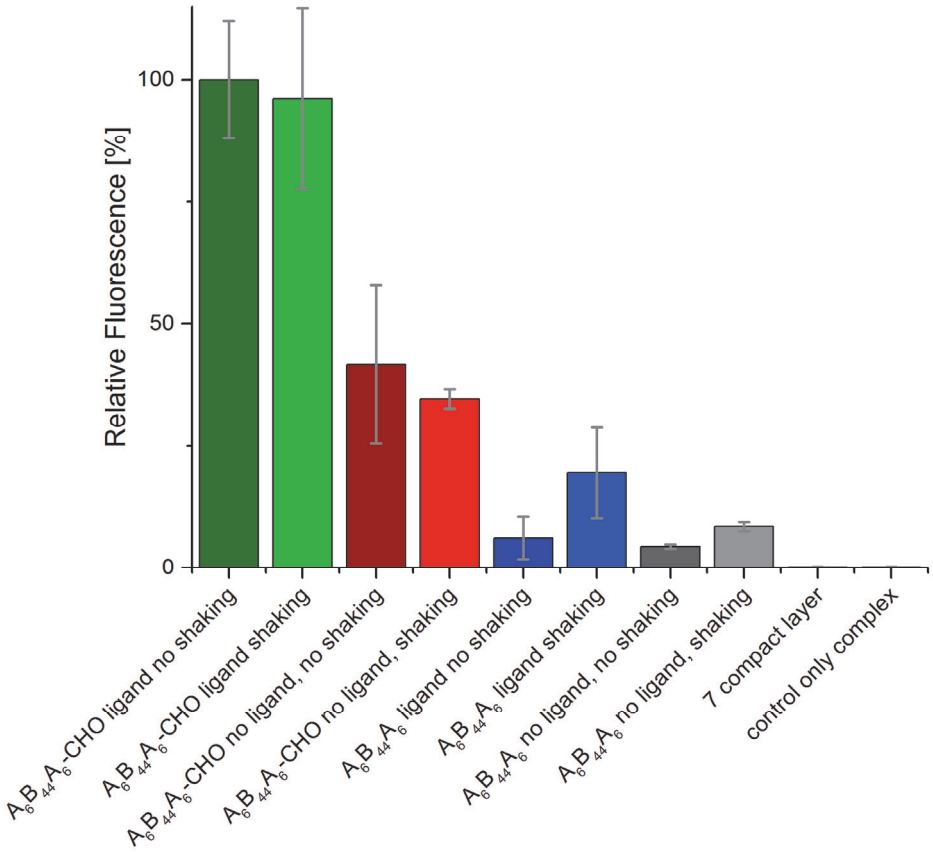

Figure 5.13. *Mean fluorescence intensities of the modified surfaces calculated from raw CLSM images and normalized to 100%.*

The mean fluorescence intensity and standard deviation were calculated from each raw CLSM image (ImageJ) to quantify the surface fluorescence and to visualize the results (Figure 5.13) The trend confirms the observations in the graphical evaluation. "$A_6B_{44}A_6$-CHO ligand no shaking" and "$A_6B_{44}A_6$-CHO ligand shaking" gave the highest fluorescent intensities. The fluorescence is strongly decreased by the absence of the aldehyde groups on the polymersomes (samples "$A_6B_{44}A_6$ ligand" and "$A_6B_{44}A_6$ no ligand"). "$A_6B_{44}A_6$-CHO ligand" and "$A_6B_{44}A_6$-CHO no ligand" give similar fluorescence intensities, that can be explained by the formation of agglomerates. To compare the numerical values and to determine the significance of the factors ligand and shaking, two way analysis of variance (ANOVA) was used (Table 5.1).

	Df	Sum of Squares	Mean Square	F Value	P Value	Signif. Code
CHO	1	122815.5	122815.5	80.85844	2.16E-13	***
Ligand	1	11517.11	11517.11	7.582558	0.007456	**

Shaking	1	126.1628	126.1628	0.083062	0.774018	
CHO:Ligand	1	11638.51	11638.51	7.662485	0.007163	**
CHO:Shaking	1	961.0777	961.0777	0.632748	0.428964	
Ligand:Shaking	1	260.1544	260.1544	0.171279	0.680208	
Residuals	72	109360.5	1518.896			

Table 5.1. *The results of two way ANOVA regarding significance of factors ligand and shaking; Signif. codes: 0 '***', 0.001 '**,' 0.01 '*', 0.05 '.', 0.1 ' ', 1*

The ANOVA test showed a significant difference between samples that did contain the ligand and samples that did not. Also, there is a significant difference between samples containing an aldehyde functionalization and samples that did not. However, the shaking does not make a significant difference. Therefore the factors CHO:Ligand and CHO:Shaking were tested. CHO:Ligand is significant, whereas CHO:Shaking is not. Consequently, effective binding depends exclusively on the co-presence of the ligand and the aldehyde group.

After verifying the surface immobilization of polymersomes via CLSM, single polymer vesicle imaging was performed using AFM to prove the preserved functionality of the polymersomes. AFM relies on even smoother surfaces. Therefore, commercially available titania covered chips (for QCM) were used. For AFM imaging, these sensor chip surfaces were modified with the same methodology used for the spin-coated surfaces for CLSM measurements. Because of the significance shown by the ANOVA test, no shaking was applied. A sample "$A_6B_{44}A_6$-CHO ligand" ([Fe(**2**)(**6**)]$^{2+}$), a reference "$A_6B_{44}A_6$-CHO no ligand" (by using polymersomes from modified polymer without any ligand) and a blank (bare and unmodified sensor surface) were made. Height traces were measured on the AFM images to gain insight into the shape and height of the prominent peaks.

The AFM pictures taken from sample "$A_6B_{44}A_6$-CHO ligand" (Figure 5.14) display several spherical structures. Their width and height can be determined from the measured height traces (Figure 5.15). The majority of peaks show rounded tops as would be expected for spherical structures. The structures are between 200 and 500 nm wide, between 20 and 70 nm high, with the majority being around 20 nm in height.

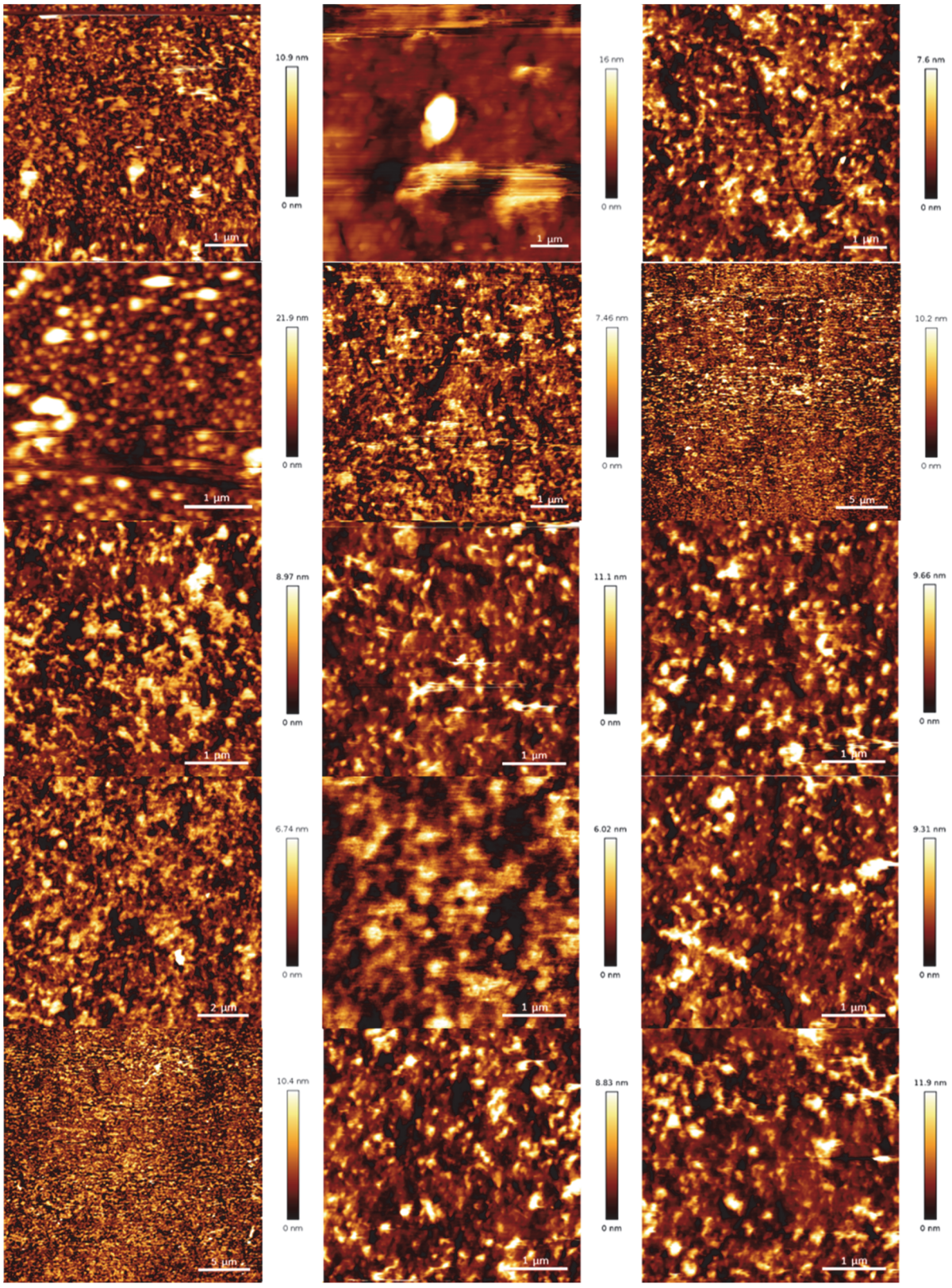

Figure 5.14. *AFM images of different areas on the sample "$A_6B_{44}A_6$-CHO ligand".*

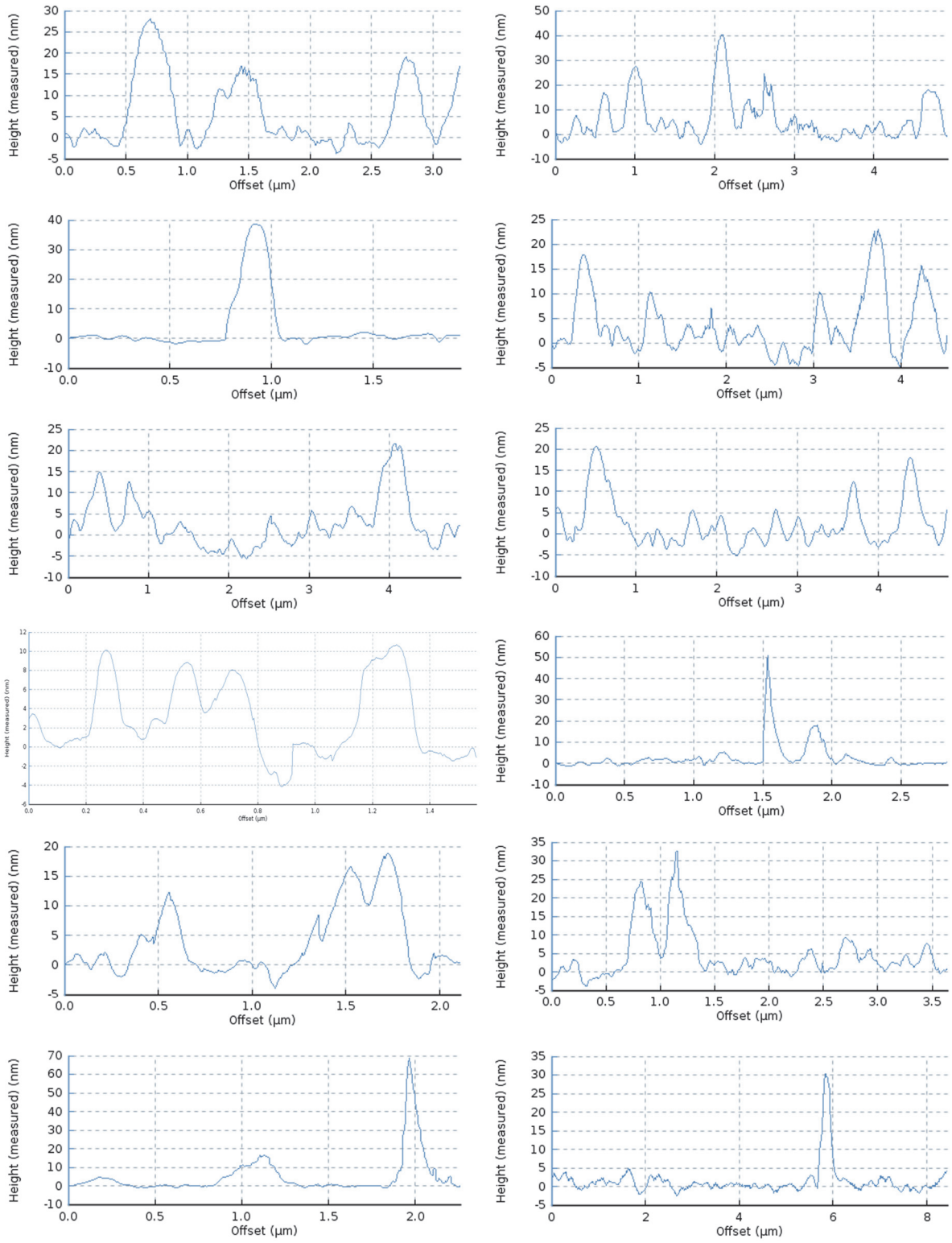

Figure 5.15. *Height traces taken from AFM measurements of sample "$A_6B_{44}A_6$ ligand".*

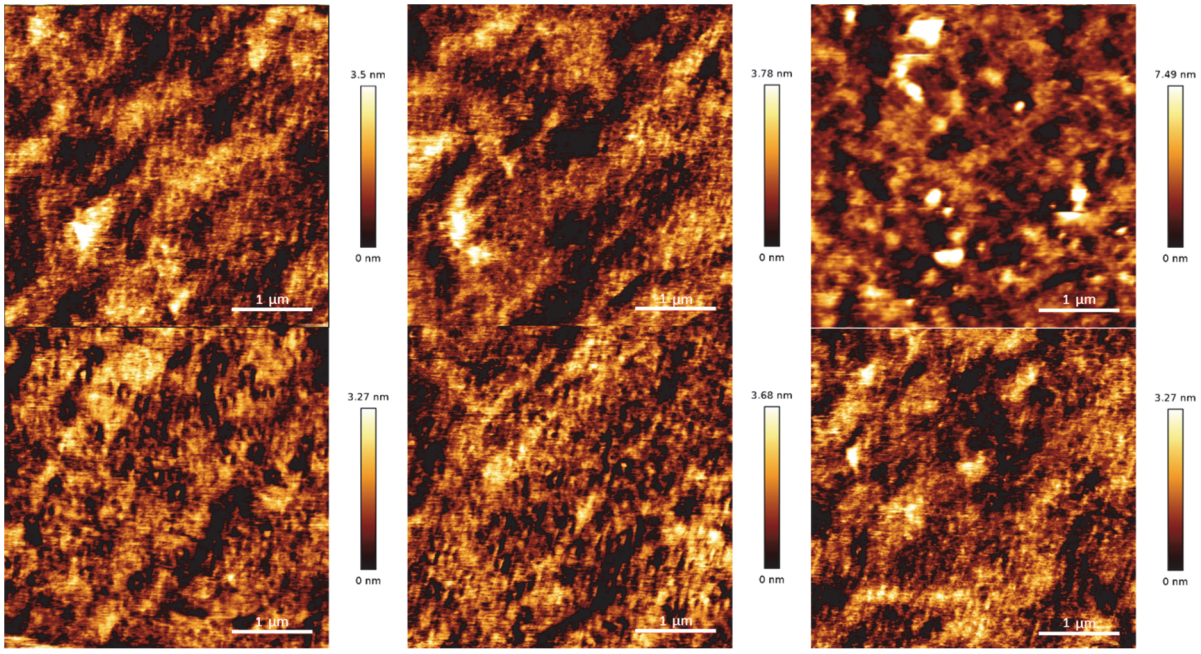

Figure 5.16. *AFM images of different areas on the sample "$A_6B_{44}A_6$ no ligand".*

The surface for the reference "$A_6B_{44}A_6$-CHO no ligand" is in general very smooth compared to the sample "$A_6B_{44}A_6$-CHO ligand". It shows only very few peaks (Figure 5.16). However, from the height traces it can be determined, that the peaks are mostly not rounded at the top and rarely over 5 nm high and never above 13 nm in height (Figure 5.17).

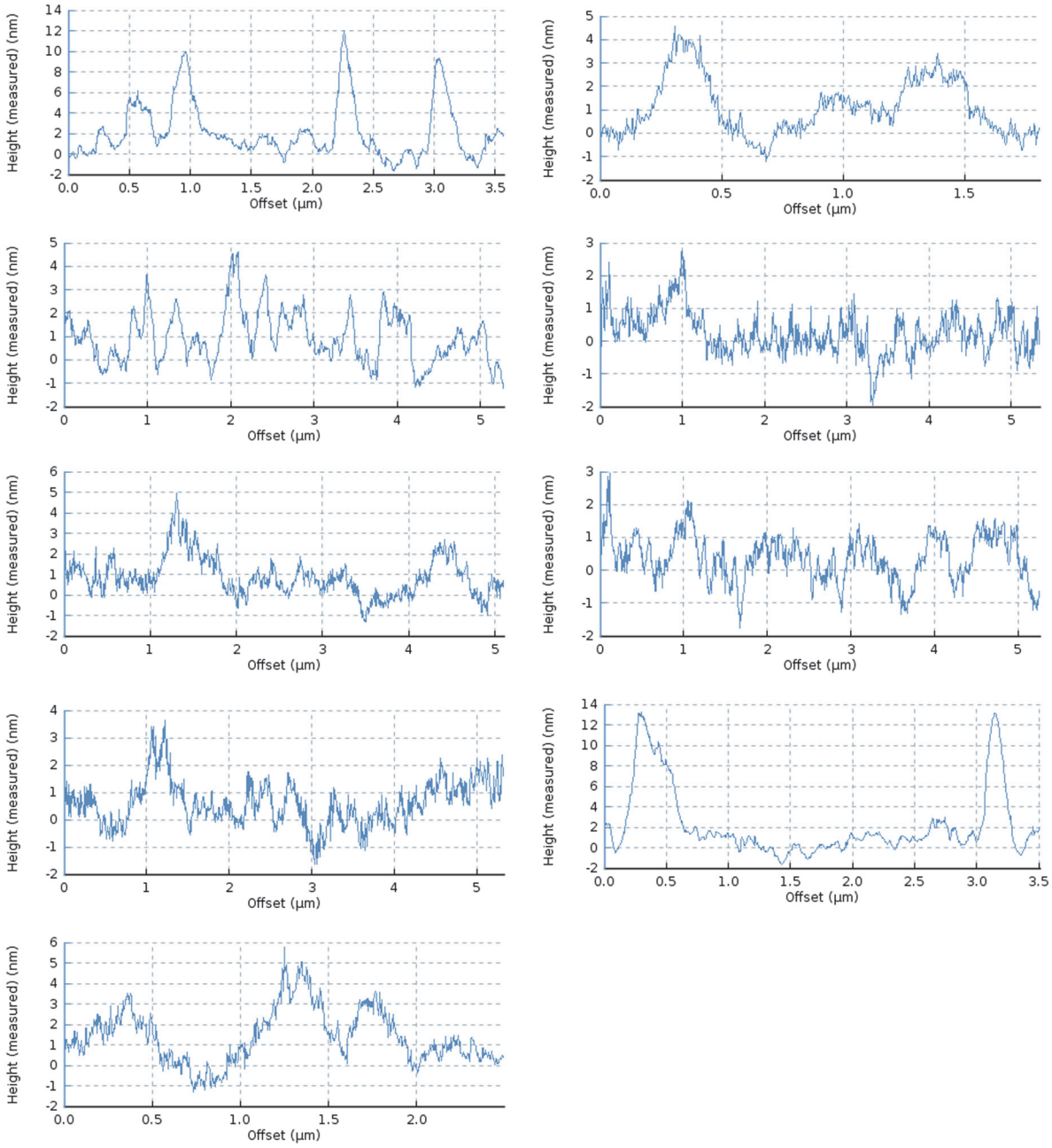

Figure 5.17. *Height traces taken from AFM measurements of control "$A_6B_{44}A_6$ no ligand".*

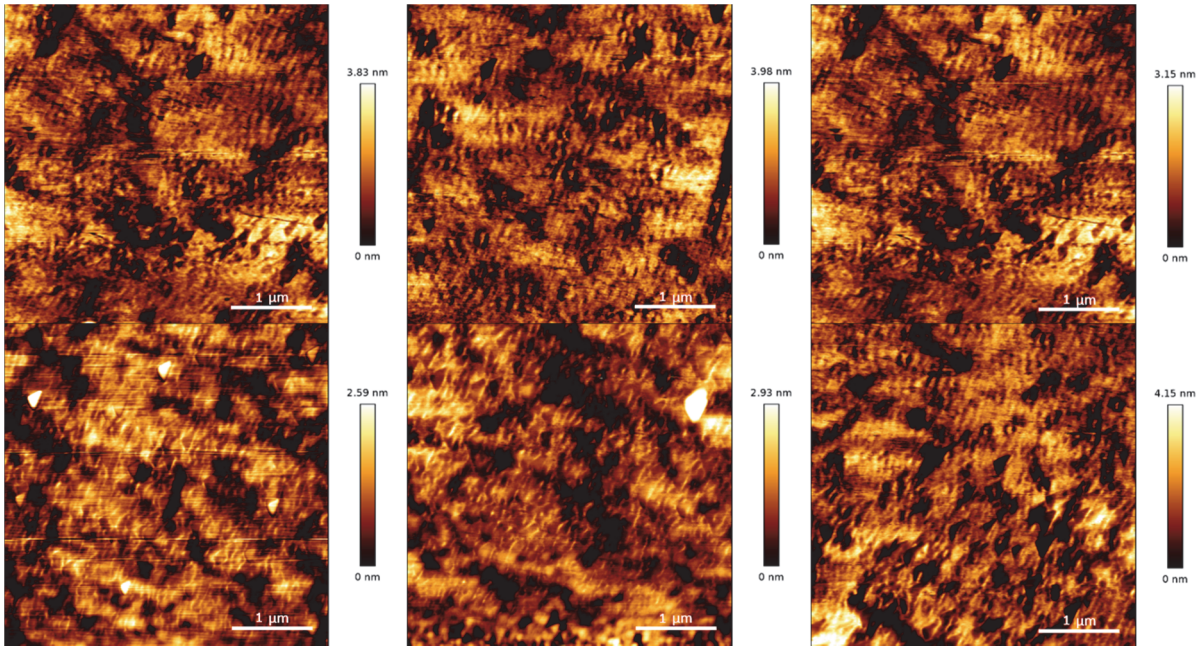

Figure 5.18. *AFM images of different areas on the sample "Blank".*

The blank, the bare sensor surface, is also very smooth compared to the sample "$A_6B_{44}A_6$-CHO ligand" surface (Figure 5.18). It shows very few peaks and none exceeds 6 nm (determined from height traces, Figure 5.19).

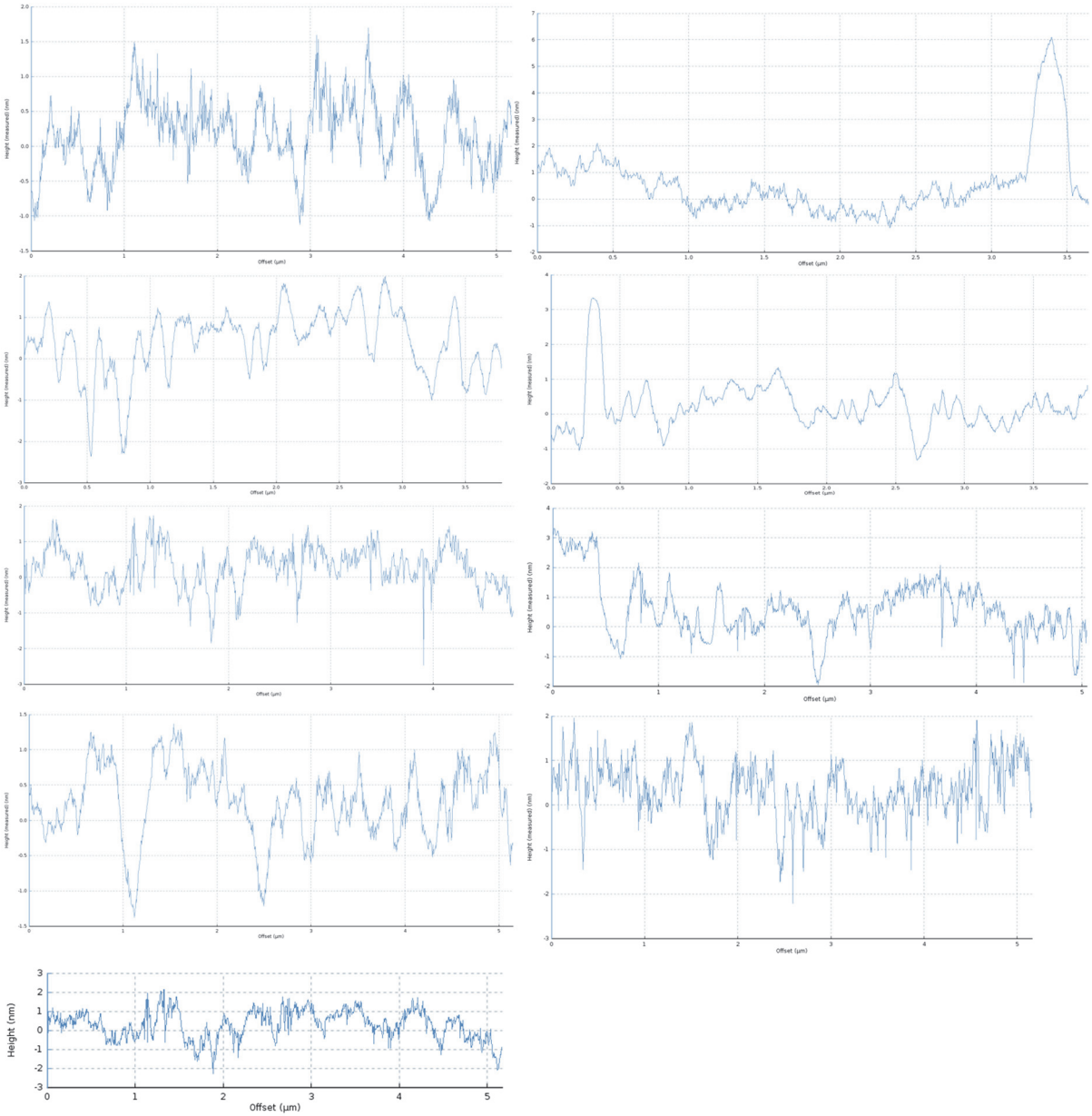

Figure 5.19. *Height traces taken from AFM measurements of blank*

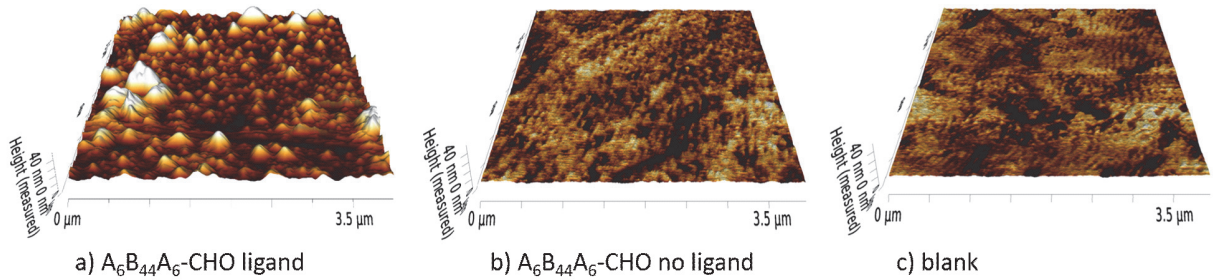

Figure 5.20. *3D representation of one selected representative measurement per modified surface (normalized to 40 nm)*

While the height profiles are clearly useful in providing height data, 3D images have the advantage of better visualization. 3D images of one selective measurement per surface can

be seen in Figure 5.20. The sample (Figure 5.20a) shows spherical objects of up to 40 nm height, whereas the reference and control surfaces are flat. All AFM measurements were conducted in tapping mode, which, depending on the applied force, can lead to compression of the flexible polymersome vesicles. The membrane thickness of $A_6B_{44}A_6$ is well-established to be 10.7 ± 0.7 nm. [11] The measured height of the spherical structures 20 nm and higher is in agreement with twice this membrane thickness and indicates successful polymersome immobilization.

Conclusion

In this chapter, polymersomes assembled from $A_6B_{44}A_6$-CHO and functionalized with a tpy unit were succesfully immobilized onto the previously optimized titania coated surfaces as well as commercially available QCM sensors with preserved architectures. Surface immobilization was confirmed by CLSM measurements in combination with a two way ANOVA test. The test verifies, that the strong homogeneous fluorescence observed for the sample "$A_6B_{44}A_6$-CHO ligand", i.e. the surface bound polymersomes, depends exclusively on the co-presence of the ligand and the aldehyde group. We also determined that shaking has no influence on surface binding.

Single surface bound polymersomes were imaged using AFM. By measuring height traces, the height of the spherical surface-bound structures was determined to be between 20 and 70 nm. 20 nm corresponds to twice the membrane thickness of $A_6B_{44}A_6$.

References

[1] J. T. Seil, T. J. Webster, *Int. J. Nanomed.*, 2012, **7**, 2767.

[2] L. Tamayo, M. Azocar, M. Kogan, A. Riveros, M. Paez, *Mater. Sci. Eng. C,* 2016, **69**, 1391.

[3] T. V. Duncan, *J. Colloid Interface Sci.*, 2011, **363**, 1.

[4] B. Iyisan, A. Janke, P. Reichenbach, L. M. Eng, D. Appelhans, B. Voit, *ACS Appl. Mater. Interfaces*, 2016, **8**, 15788.

[5] S. Domes, V. Filiz, J. Nitsche, A. Frömsdorf, S. Forster, *Langmuir*, 2010, **26**, 6927.

[6] N. P. Kamat, S. J. Henry, D. Lee, D. A. Hammer, *Small*, 2013, **9**, 2272.

[7] K. Muller, E. Bugnicourt, M. Latorre, M. Jorda, Y. Echegoyen Sanz, J. M. Lagaron, O. Miesbauer, A. Bianchin, S. Hankin, U. Bolz, G. Perez, M. Jesdinszki, M. Lindner, Z. Scheuerer, S. Castello, M. Schmid, *Nanomater.*, 2017, **7**, 74.

[8] A. Mills, *Chem. Soc. Rev.*, 2005, **34**, 1003.

[9] P. Klonos, A. Panagopoulou, L. Bokobza, A. Kyritsis, V. Peoglos, P. Pissis, *Polymer,* 2010, **51**, 5490;

[10] P. Klonos, A. Panagopoulou, A. Kyritsis, L. Bokobza, P. Pissis, *J. Non-Cryst. Solids,* 2011, **357**, 610.

[11] F. Itel, C. Mohamed, A. Najer, S. Lörcher, D. Wu, I. A. Dinu, W. Meier, *Macromolecules*, 2014, **47**, 7588.

Chapter 6

Materials and Methods

Chapter 2

Materials

All solvents were purchased from Sigma-Aldrich with the highest purity. Ultrapure water was obtained with a Merck Millipore Milli-Q Reference Water Purification System.

Sonoswiss cleaner L2 was purchased from Sonoswiss.

HCl and titanium ethoxide, for the titania precursor solution, were purchased from Sigma-Aldrich.

Substrate, Fluorine doped tin oxide (FTO) covered glass plates, type TCO22-7, 2.2 mm thickness, sheet resistance 7 Ω/sq, and transparent Test Cell Titania Electrodes were purchased from Solaronix.

Spin Coating

For spin coating the commercial FTO covered glass surfaces a SAWATEC SM-180-BT spin coater was used. For ultraviolet ozone (UVO) cleaning a UVO-Cleaner from Jelight Company, Inc. Model 42A SERIES was used. A Branson ultrasonic bath type 1510 was used for sonication. For sintering, a Schott Digitana heating plate was used.

AFM

Atomic force microscopy (AFM) was used for determining the roughness of the glass surfaces. A JPK NanoWizard® 3 AFM (JPK Instruments AG) was used. For roughness measurements, all measurements were carried out in the AC tapping mode in air at room temperature, using silicon cantilevers (PPP-NHCR, Nanosensors) with a nominal spring constant of 10-130 N m^{-1} and a resonance frequency of 300 kHz. The images were analyzed with the data analysis software JPK Data Processing (v. 6.0.63). Root mean squared roughness (R_{RMS}), [1] given by the standard deviation of the z-values for the sample area, was calculated for every image.

$$R_{RMS} = \sqrt{\sum_{n=1}^{N} \frac{(Zn-\bar{Z})^2}{N}}$$

Equation 6.1. *Calculation of Root mean squared roughness (R_{RMS}).*

Chapter 3

Materials

All solvents were purchased from Sigma-Aldrich with the highest purity. Ultrapure water was obtained with a Merck Millipore Milli-Q Reference Water Purification System.

Chemicals for ligand synthesis: 2-acetylpyridine, KOH, 4-bromobenzaldehyde, diethyl phosphite, triethyl amine, $Pd(PPh_3)_4$, HBr, TMSBr, NaOH, HCl, 4-aminobenzaldehyde, ammonium acetate, acetamide, acetic acid and KNO_3 were purchased from Sigma-Aldrich and were used without any further purification. 32% NH_3 was purchased from VWR Chemicals.

Transparent Test Cell Titania Electrodes, for coadsorbant optimization, were purchased from Solaronix.

$FeCl_2$ was purchased from Sigma-Aldrich.

Coadsorbants: Decylphosphonic acid, phenylphosphonic acid and *tert*-butylphosphonic acid were purchased from Sigma-Aldrich.

Buffers: HEPES, PBS and TES were purchased from Sigma-Aldrich.

Sodium dodecyl sulfate (SDS) was purchased from Bio-Rad Laboratories.

Synthesis of 2,2’:6’,2’’-terpyridine ligands

Synthesis of (4-([2,2':6',2''-terpyridin]-4'-yl)phenyl)bromide: The condensation of 4-bromobenzaldehyde with 2 equivalents of acetylpyridine is reported as a one-step procedure. [2] KOH (54.9mmol, 3.08g) pellets and NH_3 (58mL) aq. were added to a solution of 2-acetylpyridine (04mmol, 4.84g, 4.48mL) and 4-bromobenzaldehyde (11.5mmol, 2.12g) in EtOH (100ml) and stirred at RT for 24h (Figure 2.3). The precipitate was filtered, washed with EtOH (3x10ml) and recrystallized from $CHCl_3$-MeOH (20:80) to obtain (4-([2,2':6',2''-terpyridin]-4'-yl)phenyl)bromide (520 mg, 12%). [3]

Synthesis of 4-(2,2':6',2''-terpyridin-4'-yl)phenyl phosphonate (**1**): (4-([2,2':6',2''-terpyridin]-4'-yl)phenyl)bromide (3.17 mmol, 1230 mg) in toluene (7 mL) was added to a stirred solution of diethyl phosphite (4.4 mmol, 620mg, 0.574 mL), triethyl amine (4.34 mmol, 439 mg, 0.61 mL) and catalytic tetrakis(triphenyl phosphine)palladium (0.2 mmol, 231 mg) under nitrogen and stirred at 90 °C for 4h (Figure 2.3). After the addition of diethylether (50ml), triethylamine hydrobromide is removed by filtration. The solvent is removed from the solution containing

compound **1** (832mg, 63%) and impurities. [3] ^{1}H-NMR ($CDCl_3$, 400 MHz): 8.75 (s, 2H, H^{B3}), 8.73 (ddd, 2H, J_{HH} = 4.76, 1.81 and 0.90 Hz, H^{A6}), 8.68 (dt, 2H, J_{HH} = 8.00 and 1.11 Hz, H^{A3}), 7.98 (m, 4H, H^{A4+C3}), 7.89 (m, 2H, H^{C2}), 7.37 (ddd, 2H, J_{HH} =7.50, 4.78 and 1.23 Hz, H^{A5}), 4.17 (m, 4H, H^{a}), 1.36 (dt, 6H, J_{HH} = 7.07 Hz, J_{PH} = 0.56 Hz, H^{b}). ^{1}H-NMR (Figure 2.3) matched that reported in literature. [3]

Synthesis of (4-([2,2':6',2''-terpyridin]-4'-yl)phenyl)phosphonic acid (**2**): The deprotection of phosphonic esters is a well-known reaction and should be performed to allow for better anchoring to the semiconductor surface. [3, 4] Bromotrimethylsilane (42 mmol, 6430 mg) is added to a solution of **2** (10.5 mmol, 4659 mg) in anhydrous dichloromethane (40 mL) under nitrogen and stirred overnight at RT. The solvent was evaporated and the solid dissolved in methanol (160 mL), stirred at RT for 2 h, filtered, washed with ethanol (120 mL) and acetone (120 mL) and dried under vacuum. The resulting white solid was dissolved in water (80mL) by addition of 10% NaOH (aq) and precipitated by adding 10% HCl (aq) solution until pH 3. The precipitate was filtered, washed with water (120 mL), ethanol (120 mL) and acetone (120 mL) and dried under vacuum to afford **2** (3360 mg, 82%). ^{1}H-NMR (*d_6*-DMSO, 400 MHz): 8.82 (ddd, 2H, J_{HH} = 4.88, 1.82 and 0.91 Hz, H^{A6}), 8.80 (s, 2H, H^{B3}), 8.77 (dt, 2H, J_{HH} = 7.96 and 1.11 Hz, H^{A3}), 8.14 (td, 2H, J_{HH} = 7.79 and 1.78 Hz, H^{A4}), 8.08 (m, 2H, H^{C3}), 7.91 (dd, 2H, J_{HH} =12.57 and 8.27 Hz, H^{C2}), 7.62 (ddd, 2H, J_{HH} = 7.59, 4.88 and 1.21 Hz, H^{A5}), 3.97 (s, 2H, $H^{P(O)OH}$). ^{1}H-NMR matched that reported in literature. [3]

Synthesis of 4-([2,2':6',2''-terpyridin]-4'-yl)aniline (**3**): Ligand **3** was also prepared using Kröhnke methodology (Figure 3.6) and the ^{1}H-NMR spectra matched the literature data. ^{1}H-NMR ($CDCl_3$, 400 MHz): 8.73 (dd, 2H, J_{HH} = 4.77 and 0.88 Hz, H^{A6}), 8.69 (s, 2H, H^{B3}), 8.66 (d, 2H, J_{HH} = 7.97 Hz, H^{A3}), 7.87 (m, 2H, H^{A4}), 7.78 (d, 2H, J_{HH} = 8.54 Hz, H^{C2}), 7.34 (ddd, 2H, J_{HH} = 7.47, 4.80 and 1.23 Hz, H^{A5}), 6.80 (d, 2H, J_{HH} = 8.57 Hz, H^{C3}), 3.87 (s, 2H, H^{NH2}). ^{1}H-NMR matched that reported in literature. [5]

Synthesis of 4'-phenyl-2,2':6',2''-terpyridine (**4**): Ligand **4** was synthesized according to the literature. [6] ^{1}H-NMR ($CDCl_3$, 400 MHz): 8.72 (s, 2H, H^{B3}), 8.68 (m, 2H, H^{A6}), 8.63 (d, 2H, J_{HH} = 7.98 Hz, H^{A3}), 7.86 (m, 4H, H^{C2+A4}), 7.45 (m, 2H, H^{C3}), 7.39 (m, 1H, H^{C4}), 7.32 (m, 2H, H^{A5}). ^{1}H-NMR matched that reported in literature. [6]

NMR Spectroscopy

^{1}H-NMR spectra were recorded at 25 °C using a Bruker DPX-400 NMR spectrometer (Bruker, Switzerland). The chemical shifts of 1H were referenced with respect to δ(TMS) = 0 ppm.

UV-vis Spectroscopy

Solid-state absorption spectra were recorded on an Agilent Cary 5000 UV-vis spectrometer equipped with VARIAN Cary Win UV Scan Application software. All measurements were performed in single beam mode. Spectra were recorded between 350 and 800 nm wavelength. The measurements were calibrated with a transparent Test Cell Titania Electrode and a measurement with zero transmittance. The absorbance intensities were referenced to an non-functionalized, transparent Test Cell Titania Electrodes. It is not possible to quantify the absolute dye loading on the electrode.

Quartz Crystal Microbalance (QCM)

A QCM is an ultrasensitive weighting device. It is based on a single quartz crystal, with electrodes on both sides, that oscillates at its resonance frequency by an external circuit. Any change in mass causes a frequency shift. If the added mass is rigidly attached to the crystal, evenly distributed over the surface and much smaller than the mass of the crystal, the added mass is proportional to the frequency change. (ref 4) QCM measurements were performed with a QSense quartz crystal microbalance (Biolin Scientific AB), equipped with a High Precision Multichannel Dispenser pump (ISMATEC IPC).

Cyclic Voltammetry

Cyclic voltammograms were recorded using a CH Instruments Scanning Electrochemical Microscope. The setup was built as follows: an FTO glass, to which titia compact layers were deposited, was used as the working electrode; 0.1 M potassium nitrate was used as electrolyte. The spectra were recorded within the potential window of 1 to 1.5 V and scan rates varied between 0.03 and 0.1 V/s. In the measurements, the modified glass substrates with the surface bound $[Fe(tpy)_2]^{2+}$ were used as the working electrode. The counter electrode was a platinum wire and the reference electrode was a silver wire. The measurements were not referenced and served only as a qualitative comparison.

Chapter 4

Materials

All solvents were purchased from Sigma-Aldrich with the highest purity. Ultrapure water was obtained with a Merck Millipore Milli-Q Reference Water Purification System.

DMP for polymer oxidation was purchased from Sigma-Aldrich and was used without any further purification. Deuterated solvents were purchased from Cambridge Isotope Laboratories Inc.

Sulforhodamine B (SRB) was purchased from ThermoFischer.

Polymer oxidation

Synthesis of aldehyde terminated $PMOXA_6$–$PDMS_{44}$–$PMOXA_6$, $A_6B_{44}A_6$-CHO: The hydroxyl terminated $A_6B_{44}A_6$ was converted to the aldehyde terminated $A_6B_{44}A_6$-CHO by a mild oxidation using Dess-Martin periodinane (DMP), in accordance with a published protocol with minor modifications. [7-10] $A_6B_{44}A_6$ in DCM reacts with a small excess of DMP (2.2 eq) in DCM under inert conditions. The solvent is removed and the $A_6B_{44}A_6$-CHO purified by dialysis against EtOH.

Preparation of SRB-loaded PMOXA-PDMS-PMOXA polymersomes

SRB-loaded polymersomes were prepared at RT from the triblock copolymers, $A_6B_{44}A_6$ and $A_6B_{44}A_6$-CHO $PMOXA_6$-$PDMS_{44}$-$PMOXA_6$. Polymersomes were generated using the film rehydration technique in which the polymer was dissolved in a small amount of chloroform, dried, and 1 mM sulforhodamine B in HEPES at RT is then used as a rehydration solution in order to yield a final polymer concentration of 3 mg/mL. Rehydrated films were stirred overnight at RT, while being protected from light. All samples were extruded through an Avanti mini-extruder (Avanti Polar Lipids, USA) using a Merck 200 nm diameter pore-size polycarbonate membrane (21 times) at RT in order to obtain size homogeneity. Non-encapsulated dye was removed from the polymersomes by using a HiTrap Desalting ready-to-use 5 ml column, pre-packed with Sephadex G-25 Superfine, and equilibrated with HEPES.

NMR Spectroscopy

^{1}H-NMR spectra were recorded at 25 °C using a Bruker DPX-400 NMR spectrometer (Bruker, Switzerland). Purified copolymers were measured after 2 days of dialysis against ethanol, taking into account as reference the solvent peak at 7.26 ppm.

FT-IR Spectroscopy

An ALPHA spectrometer (Bruker) with a Platinum ATR QuickSnap™ A220/D-01 sampling modules and a single reflection diamond ATR accessory, was used to perform the ATR-FTIR measurements. All spectra were recorded at a resolution of 2 cm^{-1}, in the wavenumber range of 4000 - 450 cm^{-1} as an average of 128 scans.

UV-vis Spectroscopy

Solution UV-vis spectroscopy was used to determine the amount of encapsulated SRB fluorophore. UV-vis absorption spectra were recorded on an Agilent Cary 5000 UV-vis spectrometer equipped with VARIAN Cary Win UV Scan Application software. All measurements were performed in single beam mode. Spectra were recorded between 350 and 800 nm wavelength.

Transmission Electron Spectroscopy (TEM)

Transmission electron spectroscopy (TEM) was performed with a Phillips CM 100 and an accelerating voltage of 80 kV. 5 µL of sample were adsorbed on a plasma glow discharged 400-hole carbon-coated copper grid and negatively stained using 2% uranyl acetate.

Dynamic (DLS) and static (SLS) Light Scattering

An ALV/CGS-8F goniometer (Langen, Germany), with an ALV He-Ne laser (JDS Uniphase, wavelength λ = 632.8 nm) was used for light scattering measurements. Dynamic (DLS) and static (SLS), were performed at 20°C. Dilution rows with polymer concentrations, ranging from 1.6 mg/mL to 0.3 mg/mL were prepared from polymersome stock solutions. The samples were measured at 293 K ± 0.5 K, at scattering angles of 45-100° with angular steps of 5° in 10 mm quartz cells and mounted in a thermostated toluene bath. Toluene was used as a standard. An ALV/LSE-5004 digital correlator was used to determine the photon intensity autocorrelation

function g2(t). DLS data were analyzed by a non-linear decay-time analysis supported by a regularized inverse Laplace transformation of $g^2(t)$ (CONTIN analysis). Data were analyzed at 90°. The resulting values were averaged. Angle- and concentration-dependent SLS data were analyzed by Zimm plot software, with a Refractive Index Increment (RII) set to 0.16. Note, that the Zimm plot software does not give an error for R_g values. DLS data for large aggregates (R_h > 500 nm) was discarded from further analysis.

Fluorescence Correlation Spectroscopy (FCS)

Fluorescence correlation spectroscopy (FCS) measurements were carried out using a confocal laser scanning microscope (ZEISS LSM 880, inverted microscope ZEISS Axio Observer, Carl Zeiss, Germany) with a water immersion objective lens (C-Apochromate 40x/1.2W korr FCS M27). Measurements were taken at room temperature with a sample volume of 20 µL on a glass cover slide. A diode-pumped solid-state 561-10 laser (DPSS) at 561 nm was used as excitation source for the excitation of SRB along with the appropriate filter sets. The fluorescence signal was measured in real time and the autocorrelation function was calculated by a software correlator (Zen Black). Measurements were recorded over 10 s and repeated 30 times. Correlation curves that could not be fitted were excluded (<20%). The structural parameter and the triplet state relaxation time for SRB were determined in dilute aqueous SRB solution (25 nM). Auto correlation curves were fitted using a two-component model including a triplet state. The structural parameter and the triplet state relaxation time of free SRB were fixed for the polymersome fitting (Equation 6.2).

$$G(\tau)fit = 1 + \left(1 + \frac{T}{1-T}e^{-\frac{\tau}{\tau trip}}\right)\frac{1}{N}\left[\frac{f_1}{1+\frac{\tau}{\tau D1}}\frac{1}{\sqrt{1+R^2\frac{\tau}{\tau D1}}}\right] + \left(1 + \frac{T}{1-T}e^{-\frac{\tau}{\tau trip}}\right)\frac{1}{N}\left[\frac{f_2}{1+\frac{\tau}{\tau D2}}\frac{1}{\sqrt{1+R^2\frac{\tau}{\tau D2}}}\right]$$

Equation 6.2. *τ_D represents the diffusion time, T the fraction of fluorophores in the triplet state with triplet time τ_{trip}, N is the number of particles and R the structural parameter.*

Chapter 5
Materials

All solvents were purchased from Sigma-Aldrich with the highest purity. Ultrapure water was obtained with a Merck Millipore Milli-Q Reference Water Purification System.

Sulforhodamine B (SRB) was purchased from ThermoFischer.

For imaging by confocal laser scanning microscopy (CLSM), glass micro slides (Assistant, 76x26mm, with thicknesses of approx. 1mm) and thin glass plates (Thermo Scientific™ coverslips, 22 x 50 mm, with thicknesses of 0.13 – 0.16 mm) were used.

Atomic Force Microscopy (AFM)

Atomic force microscopy (AFM) was used for imaging of surface bound polymersomes. A JPK NanoWizard® 3 AFM (JPK Instruments AG) was used. All measurements were carried out in the AC taping mode in liquid at room temperature, using silicon cantilevers (Budget Sensors) with a nominal spring constant of 5 N m^{-1} and a resonance frequency of 150 kHz. The images were analyzed with the data analysis software JPK Data Processing (v. 6.0.63). For each sample 6-15 images of different spots were taken. Height traces were measured to determine the height of each prominent peak. AFM for imaging of surface bound polymersomes was conducted in liquid. Titania covered quartz crystal microbalance chips (QSense, LOT-QuantumDesign) were used as substrate. Plastic rings (height=6mm and Ø=2-2.5cm) were glued on large glass micro slides (Assistant, 76x26mm, with thicknesses of approx. 1mm) using a water resistant two component glue. The modified chips were taken out of dipping solution 3 and glued on the glass slides in the center of the ring (Figure 6.1). The ring was filled with buffer before the surfaces could dry and constantly refilled to keep the surface wet during the measurement.

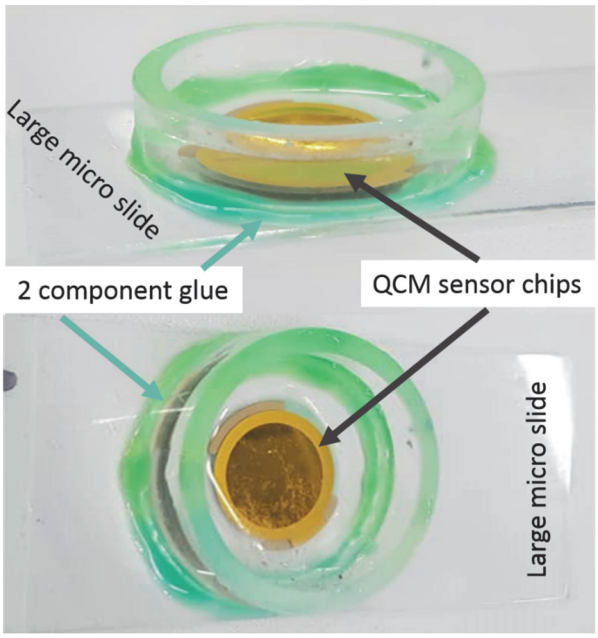

Figure 6.1. *Setup for AFM measurements in liquid.*

Confocal Laser Scanning Microscopy (CLSM)

CLSM measurements were performed at 20°C, using a confocal laser scanning microscope (ZEISS LSM 880, inverted microscope ZEISS Axio Observer, Carl Zeiss, Germany) with a water immersion objective lens (C-Apochromate 40x/1.2W korr FCS M27). A diode-pumped solid-state 561-10 (DPSS) laser was used (λ = 561 nm, 0.2 % laser intensity) as the excitation source. A main dichromatic beam splitter (MBS 458/561) was used in all the experiments. The detector range was set to 566-690 nm. The pinhole was adjusted to 1 airy units and the gain was set to 800. Each sample was scanned unidirectional using a scan time of 2.52 seconds per image and 1024 x 1025 pixel with a Bit Depth of 8 Bit. For the measurements, glass coverslips were equipped with two small pieces of the same coverslips, fixed approximately 1 cm apart by small droplets of HEPES, as spacers. Between the spacers a droplet of HEPES buffer was added on the coverslip and the sample was placed inverted on the spacers, which allowed measurements of the samples in HEPES buffer (Figure 6.2).

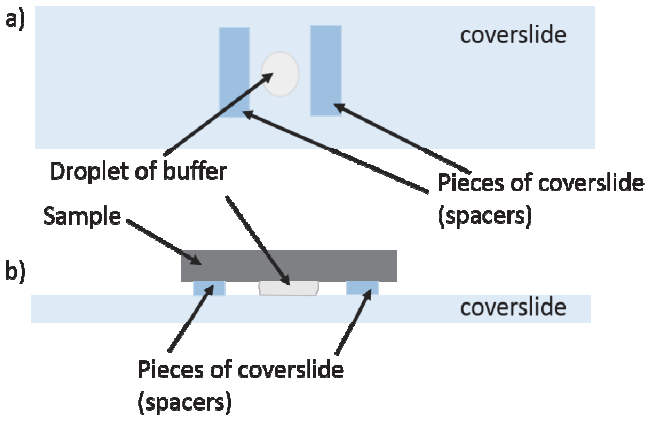

Figure 6.2. *Setup for CLSM measurement a) top view, b) side view.*

References

[1] R. R. L. De Oliveira, D. A. C. Albuquerque, T. G. S. Cruz, F. Yamaji, F. Leite, in *Atomic Force Microscopy - Imaging, Measuring and Manipulating Surfaces at the Atomic Scale*, Ed. V. Bellitto, Intech, London, England, 2012, Ch. 7.

[2] J. Wang, G. S. Hanan, *Synlett*, 2005, **8**, 1251.

[3] V. Spampinato, N. Tuccitto, S. Quici, V. Calabrese, G. Marletta, A. Torrisi, A. Licciardello, *Langmuir*, 2010, **26**, 8400-8406.

[4] F. J.Malzner, S. Y.Brauchli, E. Schönhofer, E. C. Constable, C. E. Housecroft, *Polyhedron*, 2014, **82**, 116.

[5] G. D. Storrier, S. B. Colbran, D. C. Craig, *J. Chem. Soc., Dalton Trans.*, 1997, 3011.

[6] E. C. Constable, J. Lewis, M. C. Liptrot, P. R. Raithby, *Inorg. Chim. Acta,* 1990, **I78**, 47.

[7] K. Langowska, J. Kowal, C. G. Palivan, W. Meier, *J. Mater. Chem. B,* 2014, **2**, 4684.

[8] J. K. Kowal, D. Wu, H. Stahlberg, C. G. Palivan, W. P. Meier, *Biomater.,* 2014, **35**, 7286.

[9] P. Baumann, M. Spulber, I. A. Dinu, C. G. Palivan, *J. Phys. Chem. B,* 2014, **118**, 9361.

[10] F. Itel, M. Chami, A. Najer, S. Lörcher, D. Wu, I. A. Dinu, W. Meier, *Macromolecules,* 2014, **47**, 7588.

Conclusion & Outlook

Functional polymer nanostructures were successfully immobilized on a conductive metal oxide surface by using two different self-assembly phenomena: the formation of polymersomes from block copolymers and metal-ligand interactions.

Surfaces were based on a solid glass support with titania, in the form of nanoparticles or as spin-coated layers. These surfaces were modified by decreasing surface roughness through the application of multiple layers of titania by spin-coating. The optimum smoothness was achieved after application of seven compact layers of spin coated TiO_2 (R_{RMS} = 2.0 ± 0.2 nm), reducing the surface to below 10% of its original roughness (for FTO: R_{RMS} = 24.6 to 27.6 nm). This compares to around 20% of the roughness of nanoparticulate titania (R_{RMS} = 9.4 ± 0.7 nm).

The surface was further modified by adsorption of metal-binding domains. The established SALSAC approach (´Surface-as-ligand, surface-as-complex´) for stepwise assembly of copper(I) complexes on the commercially available nanoparticulate titania surface was extended to employ the $[Fe(tpy)_2]^{2+}$ motif as a binding motif for polymersomes. Some solvents, such as EtOH, MeCN and 2-ethoxyethanol, were shown to stabilize a surface bound iron terpyridine complex, allowing for a straightforward stepwise-assembly of $[Fe(tpy)_2]^{2+}$-type complexes. On the other hand, DMSO was shown to, some extent, remove iron from the complex. However, for the assembly in solvents such as water and MeOH, coadsorbants had to be introduced to minimize the formation of homoleptic complexes with two surface-bound anchoring ligands **2**. With the use of an appropriate solvent or the addition of coadsorbants, such as *tert*-butylphosphonic acid or phenylphosphonic acid, the formation of the heteroleptic $[(\mathbf{2}_{surface})Fe(\mathbf{2})]^{2+}$ complex could be achieved via the SALSAC approach. To account for solvent effects, various aqueous buffers were tested for their influence on the system. PBS is able to desorb the $[Fe(tpy)_2]^{2+}$-complex from the surface and should be avoided, whereas water, saline, TES and HEPES are acceptable for this system. Surface binding of the $[Fe(tpy)_2]^{2+}$-type complex was also confirmed for the spin-coated surfaces.

Polymersomes were formed from an amphiphilic triblock copolymer, PMOXA-PDMS-PMOXA, whose terminal hydroxyl groups were oxidized to aldehydes (0.5% aldehyde content by ^{1}H NMR spectroscopy) using Dess-Martin periodinane (DMP). The nanoassemblies were shown to be hollow spheres with radii of up to 100 nm. The polymersomes were also shown to have encapsulation efficiencies of up to 7%, and low amounts of unspecific binding (0 to 3%). These polymersomes from aldehyde-terminated copolymer were subsequently functionalized using

an amino-functionalized tpy acting as an additional metal-binding domain through Schiff base condensation.

These functionalized compartments were able to bind to the tpy-functionalized surface by forming the $[Fe(tpy)_2]^{2+}$ motif. Successful attachment of polymersomes with encapsulated dye inside their cavities to the titania surface is confirmed by CLSM, Single surface bound polymersomes, whose height was determined to be between 20 and 70 nm, were imaged using AFM.

The resulting surfaces with immobilized polymersomes can serve as a toolbox for complex reactions taking place inside the cavities of the nanocompartments protected from the harsh environment in a confined volume. By using specific functionalized polymers, these nanocompartments can be used as hosts which release their encapsulated cargos locally on demand due to their rupture or by inducing a change of the membrane structure in respond to different external stimuli such as light, pH or temperature.

The possibility to reconstitute membrane proteins in the membranes of the polymersomes and the encapsulation of enzymes inside their cavities results in nanoreactors, where substrates and products are able to pass the membrane. The immobilization of these nanoreactors on surfaces allows enzymatic reactions to take place at specific places on demand. Even further if we think about different nanoreactors immobilized next to each other on the surface, each producing different kinds of products based on different kinds of enzymatic reactions, this would allow the realization of cascade reactions in a chip-like manner.

Acknowledgements

First of all, I want to express my gratitude to Prof. Dr. Catherine E. Housecroft and Prof. Dr. Edwin C. Constable for giving me the opportunity to do my PhD in their group. Thank you for being the best supervisors a PhD student could wish for. Thank you for being patient, supportive and encouraging and for always having an open office door that we were never afraid to enter.

I thank Prof. Dr. Christof Sparr for being my co-examiner. Thank you for investing your time, especially on such short notice.

I want to thank Prof. Dr. Cornelia G. Palivan and Prof. Dr. Wolfgang P. Meier for the wonderful collaboration project and the swiss national science foundation (SNF) for financial support through the national centre of competence in research –molecular systems engineering (NCCR MSE).

Big thanks go to all members of the Constable/Housecroft group, for the nice working atmosphere. Thank you for being amazing colleagues, for helping and supporting each other. Thank you for becoming friends. Thank you for the great time we had in the office, in the lab, at conferences at aperos and at weddings, too. Thank you for countless coffee breaks. For games, serious discussions and stupid jokes. It was a pleasure!

In particular I want to thank the following people.
Martina Garni, I do not know how to thank you. We started out at the Uni together. Thank you for many years of friendship, for great discussions, for your support and your pragmatism.
Martina Ribar Hestericová, thank you for many emergency coffees. I appreciate your levelheadedness and relied on it many a time.
Fabienne Thommen, thank you for your friendship, which made countless hours of studying much more cheerful.
Angelo Lanzilotto, thank you. Not only for being one of the best colleagues one can have, but for being a great friend as well. You are incredibly stubborn. So am I. It is a wonder we got along so well. Thank you for your friendship and your help whenever I needed it.
Mariia Karpacheva, I want to thank you for being a great colleague and friend, for awesome discussions, lovely coffee breaks and a video of a pet bear eating cake.

Sarah Keller, thank you for speaking your mind, for being fun to be around and for good talks.
Nathalie Marinakis, thank you for many a heartfelt discussion. For giving perspective and shaking me up, when I needed it.
Max Klein, thank you for always spreading a good mood, for introducing games in the coffee breaks and especially for insisting on coffee breaks and thank you as well for organizing great group trips.
Fabian Brunner, thank you for your great advice. It is greatly appreciated.
Frederik Hug, thank you for organizing great group trips, a lot of IT help and a lot of tips around the thesis.
Marianna Spulber, thank you for spontaneous drinks and for bringing everyone together.
Audrey Fischer, thank you for the most enjoyable lunches. Thank you for your honest advice and especially for all the help proofreading my CVs.
Bernhard Jung, thank you for the computer support. I would not have survived without you. Thank you for the good time in the practicum and also for printing all those posters.
Beatrice Erismann, thank you for being there for everybody, for all your administrative work, for all the aperos, for being patient with me and fort the little gifts from your travels as well.
Tomaz Einfalt, thank you for the patient explanations, nice talks and especially for proof reading my thesis.
I thank the workshop, namely Andres Koller, Markus Ast, Andreas Sohler, Meha Hisni and Pascal Andrek for keeping the building running and for their help in maintaining instruments, but even more for doing way more than is their job, for being creative and helpful and for always finding a solution.

Furthermore, I thank Maik Deppe for his love and support. Thank you for being there through all ups and downs, for believing in me and for never wavering.
I thank my parents, Ilse Rennich-Wiesler and Karl Wiesler, for their endless support. Thank you for making all this possible.
I want to thank my Brother, Robert Vincent Wiesler, my cousin, Nadine Bless, and my friend, Stephanie Kaiser, for being there for all this time, for listening and for cheering me on.

On a special note I want to mention my dog, Amos, who has been with me for 11 years now, through my whole chemistry education. He has grounded me and always cheered me up.

I will never forget these past 4 years!